Astronomy Letters, Vol. 26, No. 12, 2000, pp. 757–762. Translated from Pis'ma v Astronomicheskiĭ Zhurnal, Vol. 26, No. 12, 2000, pp. 883–888.
Original Russian Text Copyright © 2000 by Karataeva, Hagen-Thorn, Yakovleva.

A Study of the Object ZGC 2315+03: A Candidate Polar Ring Galaxy

G. M. Karataeva*, V. A. Hagen-Thorn, and V. A. Yakovleva
Astronomical Institute, St. Petersburg State University, Bibliotechnaya pl. 2, Petrodvorets, 198904 Russia

Received May 11, 2000

Abstract—We report the results of spectroscopic and photometric observations of ZGC 2315+03 with the 6-m Special Astrophysical Observatory telescope. This object is shown to belong neither to polar ring galaxies nor to close interacting pairs. The peculiar appearance of ZGC 2315+03 is explained by projection effects. *© 2000 MAIK "Nauka/Interperiodica".*

Key words: *galaxies, groups and clusters of galaxies, intergalactic gas*

INTRODUCTION

The galaxy designated as ZGC 2315+03 (Fig. 1) was first cataloged by Zwicky *et al.* (1965). The catalog gives a rough estimate of its integrated magnitude ($m_{pg} \approx 17^m$) and not too reliable data on its radial velocity obtained from weak absorption lines (V_{hel} = 18 770 km s^{-1}). Subsequently, Zwicky (1971) described the object as "a crossed galaxy, post-eruptive or result of the crossing of a compact galaxy… through an edge-on spiral." ZGC 2315+03 is apparently not a member of a particular group or cluster of galaxies.

In their *Catalog of Polar Ring Galaxies, Candidates, and Related Objects*, Whitmore *et al.* (1990) included ZGC 2315+03 in a group of possible candidates for polar ring galaxies (PRC C-71). They suggested that the elongated structures at position angles ~125° and 64° were the "disk" and "polar ring" of the galaxy, respectively. A dust lane stretching along the major axis was detected in the disk. The authors also provide photometric and color profiles along the main axes. It is said in the text that the ring is bluer, in conflict with the figures (clearly, there is confusion as to which feature is represented by a particular profile).

We have failed to find any other studies of this unusual object.

The lack of any kinematic information was the reason why ZGC 2315+03 was included in the program of research on polar ring galaxies and candidates under way at the Astronomical Institute of St. Petersburg University. Originally, we were going to restrict ourselves to spectroscopic observations, but these were later supplemented with photometry.

For the Hubble constant H_0 = 65 km s^{-1} Mpc^{-1}, the object's distance of 295 Mpc corresponds to the redshift 19 195 km s^{-1} (our value, see below), which gives a scale of 1.43 kpc in 1″.

OBSERVATIONS AND DATA REDUCTION

Our spectroscopic observations of the galaxy ZGC 2315+03 were performed in November 1996 at the prime focus of the 6-m Special Astrophysical Observatory (SAO) telescope with the UAGS long-slit spectrograph. A 530 × 580 CCD detector (pixel size 18 × 24 μm) was used. The spectrograph slit size was 2″ × 210″, the scale along the slit was 0.″4/pixel, and the dispersion was 1.55 Å/pixel. All frames were taken in the red spectral range (6200–7000 Å). For accurate wavelength calibration, we observed the comparison spectrum of an Ar–Ne–He lamp before and after each exposure. The seeing during our observations was about 3″. The slit position angles roughly corresponded to the directions of the main axes and passed through the object's brightest point. A log of spectroscopic observations is given in Table 1.

Table 2 gives a log of our photometric observations performed in Johnson's *B* and *V* and Cousins's R_c bands in September 1999 at the prime focus of the 6-m SAO telescope. Unfortunately, we had to use observations of standards on neighboring nights for calibration. Our data are therefore preliminary, but are suitable for drawing some important conclusions.

The observations were reduced at the Astronomical Institute of St. Petersburg University using the ESO-MIDAS, LONG ESO-MIDAS software package and spectrum reduction procedures developed by D.I. Makarov (SAO).

---

* E-mail address for contacts: narka@gong.astro.spbu.ru

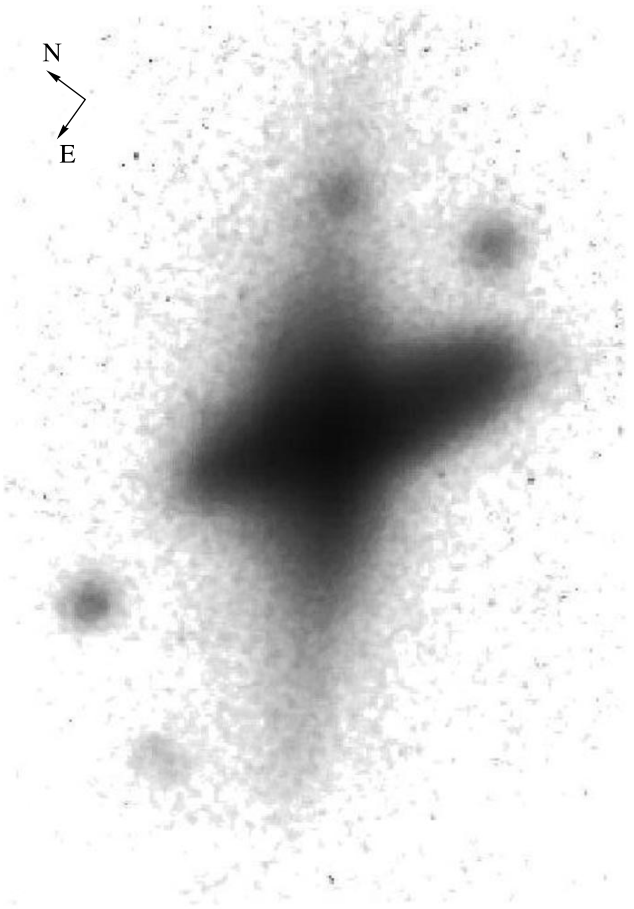

Fig. 1. A reproduction of the *B*-band image for ZGC 2315+03.

The accuracy of our radial-velocity determinations is 15 and 25 km s^{-1} for strong and weak emission lines, respectively.

RESULTS OF OBSERVATIONS

Spectroscopic Data

All our spectra show emission lines. The strongest line is Hα; [N II] λ6583 Å follows next. The Hα line in the spectrum of the presumed ring [for now, we use the structure names from Whitmore *et al.* (1990)] extends to distances ≈15″ (21 kpc) from the center. These spectra also exhibit weak [S II] λλ6717, 6731 Å lines. By way of illustration, Fig. 2 shows isophotes of the spectrum taken at position angle 54°. The lines are clearly seen to be curved, suggesting the rotation of gaseous masses around the minor axis of the ring. Emission features in the disk spectra are less intense and extend not so far, approximately to 5″ (7.2 kpc).

Radial-velocity curves are presented in Fig. 3, where the filled and open symbols refer to the disk and the ring, respectively. The radial-velocity curves constructed from the Hα and [N II] lines are seen to coincide. Note also that the curves have a regular shape (with the exception of the curve for position angle 125°, at which the spectrograph slit was along the dust lane); they show no perturbations commonly encountered in galaxies experiencing close interactions. At the same time, it should be noted that they are not symmetric about the brightness center (0″ radius) and that the dynamical center of the disk does not coincide with the dynamical center of the ring. It is displaced from the brightness center by 1″ to the NW and has V_{hel} = 18 990 km s^{-1} for the former and by 1″.2 to the SW and has V_{hel} = 19 030 km s^{-1} for the latter. Corrected for Galactic rotation (185 km s^{-1}), these velocities are 19 175 and 19 215 km s^{-1}, respectively.

Photometric Data

Figure 4 shows the pattern of isophotes for ZGC 2315+03 in the *B*, *V*, R_c bands. The undistorted isophote shape in the peripheral regions is noteworthy. Assuming the disk and the ring to be thin, the observed ellipticity of the isophotes implies inclinations *i* of 65° and 60° for the disk and the ring, respectively (*i* is the angle between the line of sight and the normal to the plane of the disk or the ring). The position angles of the major axes are 130° for the disk and 66° for the ring.

The *B–V* color distribution in ZGC 2315+03 is displayed in Fig. 5. Here, light and dark regions correspond to bluer and redder areas, respectively. The color

Table 1. A log of spectroscopic observations

Date	Spectrum	Exposure, min	Slit position angle, deg
Nov. 2, 1996	u05911	40	54
	u05914	30	54
	u05915	30	54
	u05917	30	114
	u05919	30	114
Nov. 4, 1996	u06003	30	64
	u06004	30	64
	u06007	30	125

Table 2. A log of photometric observations

Date	Band	Exposure, s	*z*, deg
Sept. 15, 1999	*V*	600	41.4
	B	600	40.7
	R_c	600	40.2
	B	600	39.5
	V	600	39.5
	B	600	39.6
	B	600	40.3

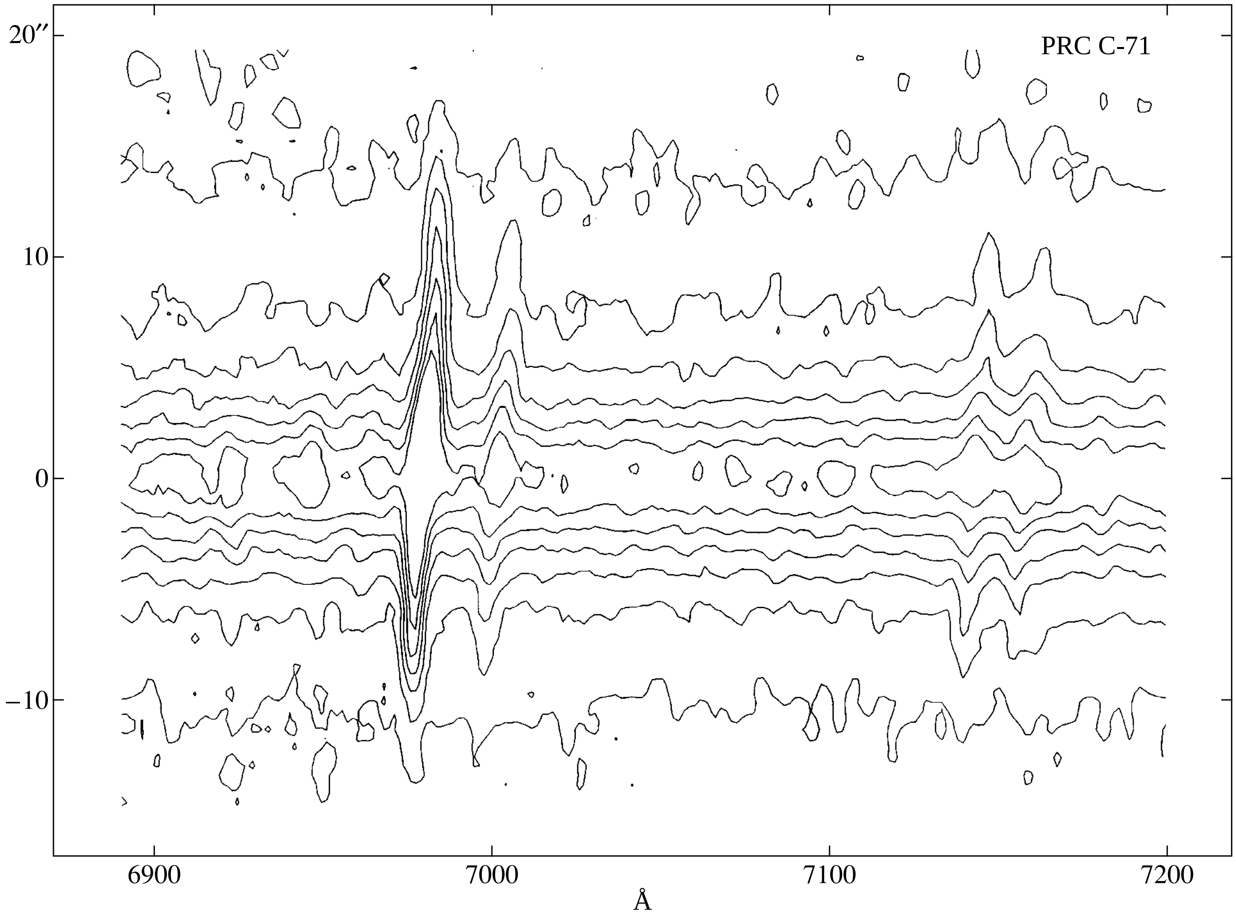

Fig. 2. Isophotes of the spectrum for ZGC 2315+03 at position angle 54°.

difference between the disk and the ring (independent of absolute calibration) is about $0\overset{m}{.}5$.

Since our photometric frames were taken at mediocre seeing (~3″), the narrow dust lane detected by Whitmore *et al.* (1990) does not show up in any way in Fig. 4. However, its presence is confirmed by the dark lane in Fig. 5, which roughly coincides with the direction of the disk major axis.

ANALYSIS OF OBSERVATIONAL DATA AND DISCUSSION

Rotation Curves

The disk rotation curve (dashed line in Fig. 6) was constructed from the 114° profile; we took photometric values for the position angle of the major axis and the inclination (respectively, 130° and 65°). The velocity increases with distance from the center and reaches 107 km s^{-1} at a distance of 5″.5 (7.9 kpc). We did not use the spectrum at position angle 125°, which is closer to that of the major axis, because it was severely distorted by the dust lane.

The ring rotation curve was constructed from two profiles at position angles 54° and 64°. The closest coincidence of these curves is achieved at position angle 66° ± 2° and inclination 70° ± 5°. We took these angles when constructing the rotation curve (solid line in Fig. 6). The velocity gradient is roughly constant, 30 km s^{-1} $arcsec^{-1}$, up to a distance of 2″(2.9 kpc). Further out, it slowly decreases and the rotation curve reaches a maximum (180 km s^{-1}) at 11″ (15.7 kpc) and probably flattens out. The curve is closely similar in shape to the rotation curve of a disk with an exponential density falloff.

Note that the disk and ring rotation curves differ, with the velocity gradient for the disk decreasing with distance more rapidly than it does for the ring. At 5″.5, the velocity in the ring is larger by approximately 27 km s^{-1}.

General Discussion

As was noted in the Introduction, there are two judgements on the nature of ZGC 2315+03 in the literature. Zwicky (1971) considered it to be either a posteruptive object or a pair of colliding galaxies, whereas Whitmore *et al.* (1990) considered it to be a polar ring galaxy. However, yet another interpretation is possible: the projection (possibly accidental) of one galaxy onto

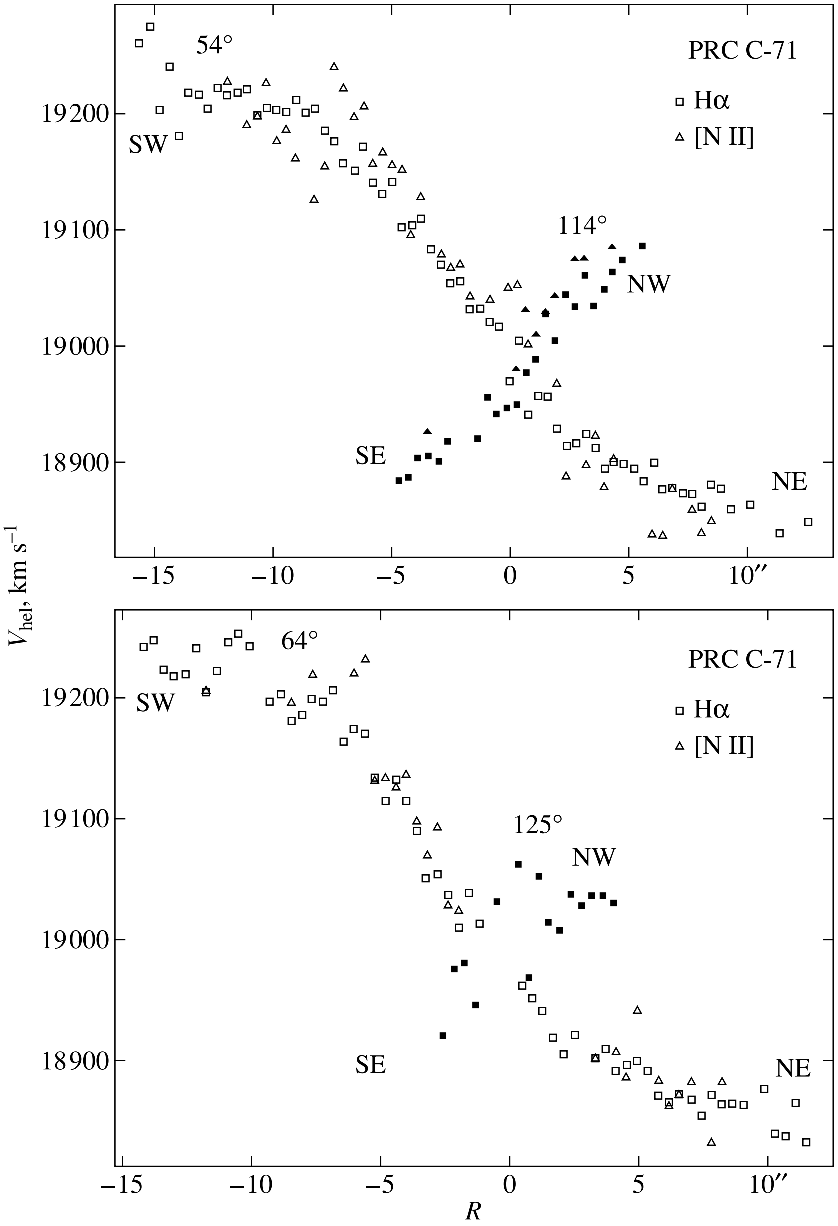

Fig. 3. Measured radial-velocity curves.

another. Let us consider arguments for and against each of these hypotheses.

The following facts argue against the hypothesis that ZGC 2315+03 is a polar ring galaxy:

(1) The location of the ring relative to the disk-galaxy center is asymmetric. Both the dynamical and photometric centers of the ring (actually the disk, because photometric data provide no evidence for a brightness dip in the middle) are displaced to the SW from the observed brightness peak.

(2) The ring deviates by 30° from the polar disk plane; this is too much for a polar ring: at such an inclination, the ring must rapidly break up because of differential precession.

(3) The dynamical centers of the disk and the ring do not coincide.

This all forces us to abandon the idea of ZGC 2315+03 as a polar disk galaxy.

Thus, the two structures elongated at position angles 130° and 66° can be assumed to be two galaxies, with both of them being most likely spiral: the first one (the disk in the old terminology) because it is rich in dust (below called a dusty galaxy) and the second one because of its color properties (below called a blue galaxy).

Of the two remaining alternatives (colliding galaxies and galaxy projection), we are inclined to the second. The reasons are as follows: undistorted isophotes in non-overlapping areas, the absence of peculiarities in the rotation curves (Fig. 6), and the difference between

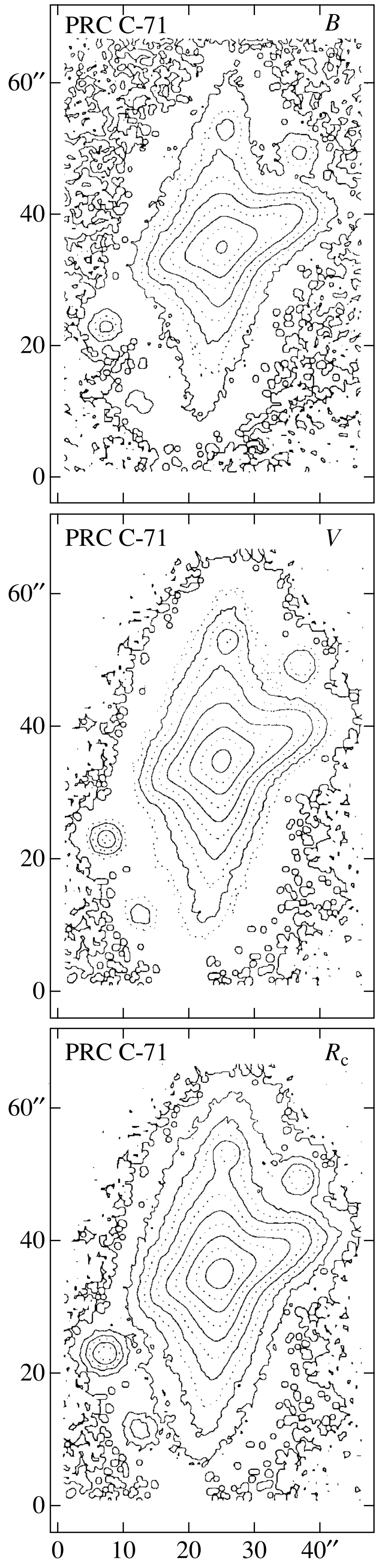

Fig. 4. The galaxy's isophotes in three color bands.

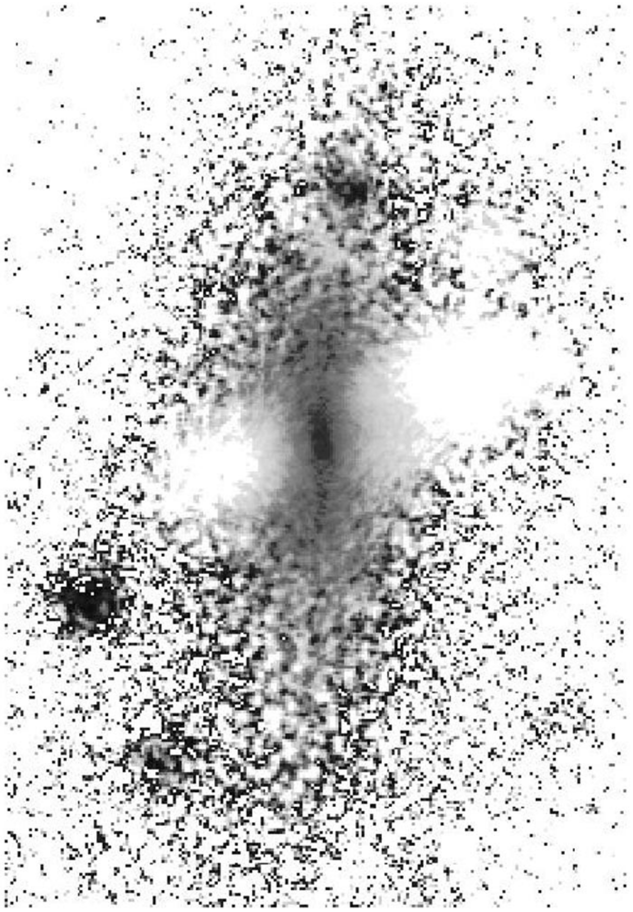

Fig. 5. The *B*–*V* color distribution over the object (darker regions correspond to a larger color index).

their gradients. In general, the isophotes and radial-velocity curves are distorted for closely interacting galaxies. In addition, ZGC 2315+03 is not an IRAS object. Closely interacting galaxies commonly show an infrared excess.

If the galaxies are projected onto each other, their masses can be estimated from the rotation curves in Fig. 6. The maximum velocity for the blue galaxy is about 180 km s^{-1} at $R = 11''$ (15.7 kpc), implying the mass $M = 10^{11}M_\odot$. Thus, its mass is comparable to the masses of giant galaxies. For the dusty galaxy, $V_{\max} =$ 107 km s^{-1} at $R = 5\overset{''}{.}5$ (7.9 kpc) and we obtain $M =$ $2.1 \times 10^{10}M_\odot$ for its mass within this range. Clearly, its total mass is also close to $10^{11}M_\odot$.

An examination of Fig. 5, which shows the color distribution in the galaxy, leads us to conclude that the blue galaxy is shielded by the dusty one, because the color index is at a maximum in the dust-lane region. For a different arrangement of the galaxies in the lane region, the contribution of the blue galaxy to the total flux would be large and a local minimum of the color index would be observed, which is not the case. In addi-

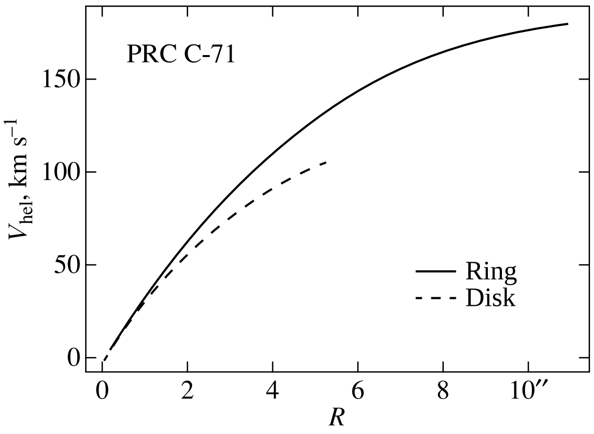

Fig. 6. Rotation curves for the two components of ZGC 2315+03.

tion, the radial velocity of the dynamical center for the blue galaxy is larger than that for the dusty one. This difference (40 km s^{-1}) is moderate and, in principle, can be explained by orbital motion in the pair. However, if both galaxies are on the line of sight, the projections of their orbital velocities onto the line of sight must be small. On the other hand, if this difference is assumed to be due to Hubble expansion, then a distance difference of 600 kpc corresponds to a difference of 40 km s^{-1} (for H_0 = 65 km s^{-1} Mpc^{-1}). At such a distance, the interaction (if any) cannot be strong and the regular shape of the isophotes and the radial-velocity curves comes as no surprise.

CONCLUSION

The results of our study lead us to conclude that the object ZGC 2315+03 is a pair of galaxies projected onto one another. They may also be interacting, but this interaction must be weak. Both galaxies are most likely giant spirals (judging by their estimated masses and by the presence of gas and dust in them), which must be confirmed by a detailed photometric study of the object.

ACKNOWLEDGMENTS

We are grateful to the Time Allocation Committee for allocating observing time at the 6-m SAO telescope. We also wish to thank A.N. Burenkov, responsible for observations with the UAGS spectrograph, and I.O. Drozdovskii, who performed the photometric observations. This study was supported in part by the Federal Program “Astronomy” (project no. 1.2.6.1) and the Russian Foundation for Basic Research (project no. 98-02-16609).

REFERENCES

1. B. C. Whitmore, R. A. Lucas, D. B. McElroy, *et al.*, Astron. J. **100**, 1489 (1990).
2. F. Zwicky, M. Karpowicz, and C. T. Kowal, in *Catalog of Galaxies and Clusters of Galaxies* (California Inst. of Technol. Publ., 1965), p. 5.
3. F. Zwicky, *Catalog of Selected Compact Galaxies and of Post-Eruptive Galaxies* (Zürich, 1971).

Translated by N. Samus’

Astronomy Letters, Vol. 26, No. 12, 2000, pp. 763–764. Translated from Pis'ma v Astronomicheskiĭ Zhurnal, Vol. 26, No. 12, 2000, pp. 889–891.
Original Russian Text Copyright © 2000 by Neshpor.

A $23\overset{d}{.}2$ Period in the Ultrahigh-Energy Gamma-Ray Flux from the Mk 501 Active Galactic Nucleus

Yu. I. Neshpor*

Crimean Astrophysical Observatory, National Academy of Sciences of Ukraine, p/o Nauchnyĭ, Crimea, 334413 Ukraine

Received February 23, 2000

Abstract—Observations at the Crimean Astrophysical Observatory are used to show that the ultrahigh-energy gamma-ray flux from the galaxy Mk 501 varies with a $23\overset{d}{.}2$ period. The period was determined by the HEGRA team from the 1997 observations. © *2000 MAIK "Nauka/Interperiodica".*

Key words: *active galactic nuclei, quasars, and radio galaxies*

The studies of active galactic nuclei (AGNs) at ultrahigh energies (10^{12} eV) by the methods of ground-based gamma-ray astronomy began after the CGRO Orbiting Observatory discovered gamma-ray emission with energy > 100 MeV from a number of AGNs. These objects arouse great interest from an astrophysical point of view, because they exhibit significant flux variations in all frequency bands (from radio to X-ray). In some cases, the large amplitudes of X-ray variations match those of optical ones (Maccagni *et al.* 1987). The variability time scale ranges from minutes to a year. AGNs are distinguished by a strong tendency for outburst (on a time scale of several days) and explosion (on a time scale of several months) activity.

The first objects to be discovered at ultrahigh energies at the Whipple Observatory (USA) were Mk 501 (Punch *et al.* 1992; Catanese *et al.* 1995) and Mk 421.

In the spring of 1997, Mk 501 was reported from the Whipple Observatory to be in an active state. According to preliminary data, the ultrahigh-energy gamma-ray flux from this object rose by more than a factor of 15 compared to its quiescent state. The HEGRA team found its flux in the spring of 1997 during several outbursts to have exceeded the Crab flux by a factor of 5–10 (Aharonian *et al.* 1997). Similar results were also obtained at other observatories (Djannati-Atai 1997; Krennrich *et al.* 1997; Hayashida *et al.* 1998). The observations of Mk 501 at the Crimean Astrophysical Observatory (CrAO) were carried out in 1997–1998. The two-year-long Crimean observations revealed ultrahigh-energy gamma-ray emission at a high confidence level (11σ in 1997 and 7.5σ in 1998), and the gamma-ray flux was shown to vary with time over a wide range. The mean gamma-ray flux at $E > 10^{12}$ eV was $(5.0 \pm 0.6) \times 10^{-11}$ phot. cm^{-2} s^{-1} in 1997 and $(3.7 \pm 0.6) \times 10^{-11}$ in 1998 (Andreeva *et al.* 2000). In 1997, the HEGRA team observed this object from February through October (more than 200 days) (Kranich *et al.* 2000). The amount of these data allowed a Fourier analysis to be performed, which revealed a $23\overset{d}{.}2$ ($f = 0.0431^{-1}$) periodicity in the ultrahigh-energy gamma-ray flux variations. Kranich *et al.* (2000) also analyzed the RXTE-ASM X-ray (2–10-keV) data obtained in the same time interval. The power spectrum constructed from the X-ray data exhibits a peak at the same frequency ($f = 0.0431^{-1}$). The simultaneous (X-ray and gamma-ray) data reduction showed that the probability of a chance origin of the spike in the power spectrum was 2.8×10^{-4}.

The galaxy Mk 501 (equatorial coordinates $\alpha = 16^h53^m47^s$ and $\delta = 39°45'50''$, 1997) was observed at CrAO from May 1 through June 10, 1997. The observations were carried out with the GT-48 gamma-ray telescope [see Vladimirskii *et al.* (1994) for a detailed description]. The object was observed in source–background mode. A session included a 25-min-long observation of the source when the object was at the center of the field of view of the GT-48 receiving camera and an observation of the background with the same duration displaced by 30^m in right ascension in order to observe it at the same zenith and azimuthal angles as the source. A total of 59 sessions were carried out; four of them were excluded from the subsequent data reduction, because the count rate of events was low or because it was highly nonuniform on the source or background due to poor weather conditions. In 47 and 8 of the sessions included in the data reduction, the background was observed after and before the source, respectively. The total duration of the source's observations was 22 h 40 min. Our data were subjected to initial reduction (Andreeva *et al.* 2000); as a result, 30 139 bursts (events) on the source and 29 345 bursts

---

* E-mail address for contacts: arnold@crao.crimea.ua

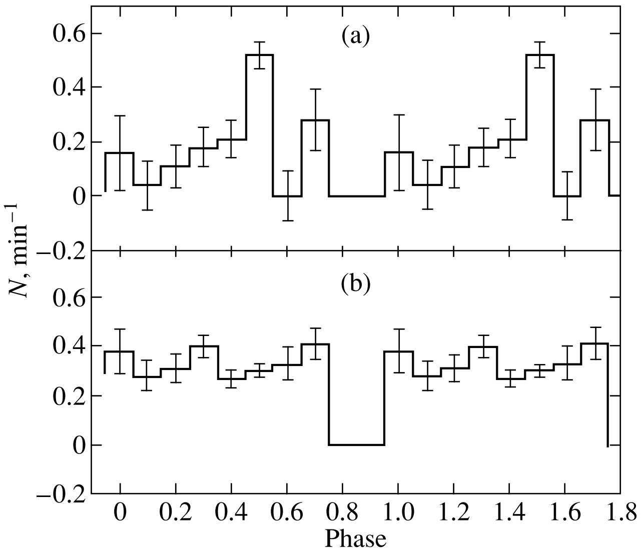

Phase histograms for (a) ultrahigh-energy gamma-ray events and (b) gamma-ray-like events on the background (t = MJD 50 545.0, $T = 23\overset{\mathrm{d}}{.}2$).

on the background were left in the 1997 observations for subsequent analysis. Gamma-ray-like events were selected by using both coordinate-dependent and coordinate-independent parameters.

As a result, the number of gamma-ray-like events was 819 on the source and 423 on the background; the number of gamma-ray photons was 396 ± 35.24 (Andreeva *et al.* 2000). For each observing night (to improve the statistics), we determined the number of detected ultrahigh-energy gamma-ray events N_γ (the amplitude of the effect) from the relation $N_\gamma = N_s - N_b$ and the statistical error in the amplitude of the effect from $\sigma = \sqrt{N_s + N_b}$, where N_s and N_b are the numbers of gamma-ray-like events on the source and background, respectively.

A phase histogram (light curve) for the amplitude of the effect with its statistical error is shown in the figure for the period $T = 23\overset{\mathrm{d}}{.}2$. The phase histogram was computed by an epoch-folding technique. The variation phase for each day was determined from $\varphi = (t - t_0)/T$, where t is the current time, t_0 = MJD 50 545.0, and $T = 23\overset{\mathrm{d}}{.}2$ (Kranich *et al.* 2000). The light curve was analyzed by using the χ^2 test.

The probability of a chance distribution of the phase histogram is 1.3×10^{-8}; i.e., it is low.

For comparison, we constructed a phase histogram for the events recorded during the background observations (see the figure). In this case, the number of events was distributed uniformly in the phase histogram ($\chi^2_{\nu = 7} = 9.0$).

The light curve constructed from ultrahigh-energy gamma-ray data (Kranich *et al.* 2000) (t_0 = MJD 50 545.0, $T = 23\overset{\mathrm{d}}{.}2$) has a maximum at phases $\Delta\varphi = 0.5$–0.55 (the period was broken down into 20 phase bins). According to the CrAO data, the maximum of the light curve (t = MJD 50 545.0, $T = 23\overset{\mathrm{d}}{.}2$) occurs at phases $\Delta\varphi = 0.45$–0.55 (the entire period was broken down into 10 phase bins). Such a close coincidence of the light curves implies that the ultrahigh-energy gamma-ray flux recorded at CrAO from Mk 501 varies with a $23\overset{\mathrm{d}}{.}2$ period. Our results confirm the presence of a $23\overset{\mathrm{d}}{.}2$ periodicity in the ultrahigh-energy gamma-ray flux from the active galaxy Mk 501.

ACKNOWLEDGMENTS

I wish to thank A.A. Stepanyan for his attention to the study. I am also grateful to Z.N. Skiruta and S.G. Kochetkova for their help in data reduction and in preparing the paper.

REFERENCES

1. F. Aharonian, A. G. Akhperjanian, J. A. Barrio, *et al.*, Astron. Astrophys. **327**, L5 (1997).
2. N. A. Andreeva, Yu. L. Zyskin, O. R. Kalekin, *et al.*, Pis'ma Astron. Zh. **26**, 243 (2000) [Astron. Lett. **26**, 199 (2000)].
3. M. Catanese, C. W. Akerlof, S. Biller, *et al.*, in *Proceedings of the Padova Workshop on TeV Gamma-Ray Astrophysics, 1995*, Ed. by M. Cresti, p. 348.
4. A. Djannati-Atai, in *Proceedings of the Kruger National Park Workshop on TeV Gamma-Ray Astrophysics, South Africa*, Ed. by O. C. de Jager (Potchefstroom Univ., 1997), p. 21.
5. N. Hayashida, H. Hirasawa, F. Ishikawa, *et al.*, Astrophys. J. Lett. **504**, L71 (1998).
6. D. Kranich, O. C. de Yager, M. Kastel, *et al.*, Astron. Astrophys. (2000) (in press).
7. F. Krennrich, J. Boyle, J. H. Buckley, *et al.*, in *Proceedings of the Kruger National Park Workshop on TeV Gamma-Ray Astrophysics, South Africa, 1997*, Ed. by O. C. de Jager, p. 32.
8. D. Maccagni, B. Garilli, R. Schild, and M. Terengdi, Astron. Astrophys. **178**, 21 (1987).
9. M. Punch, C. W. Akerlof, M. F. Cawley, *et al.*, Nature **358**, 477 (1992).
10. B. M. Vladimirskiĭ, Yu. L. Zyskin, A. A. Kornienko, *et al.*, Izv. Krym. Astrofiz. Obs. **91**, 74 (1995).

Translated by V. Astakhov

Astronomy Letters, Vol. 26, No. 12, 2000, pp. 765–771. Translated from Pis'ma v Astronomicheskiĭ Zhurnal, Vol. 26, No. 12, 2000, pp. 892–898.
Original Russian Text Copyright © 2000 by Lutovinov, Grebenev, Pavlinsky, Sunyaev.

X-ray Variability of the Pulsar Vela X-1 as Observed with ART-P/Granat

A. A. Lutovinov[1]*, S. A. Grebenev[1], M. N. Pavlinsky[1], and R. A. Sunyaev[1, 2]

[1] *Space Research Institute, Russian Academy of Sciences, Profsoyuznaya ul. 84/32, Moscow, 117810 Russia*
[2] *Max-Planck-Institut fuer Astrophysik, Karl Schwarzschild Strasse 1, 86740 Garching bei Muenchen, Germany*

Received June 9, 2000

Abstract—Observations of the X-ray pulsar Vela X-1 with the ART-P telescope onboard the Granat Observatory are presented. Variability on a time scale of several thousand seconds was detected; intensity variations are shown to be accompanied by changes in the source's spectrum. The hardness was also found to be highly variable on a scale of one pulsation period. The source's spectrum exhibits an absorption feature at energy ~27 keV, which is apparently attributable to cyclotron scattering/absorption in the neutron-star magnetic field. Weak persistent emission was detected during an X-ray eclipse, which probably resulted from the scattering of pulsar emission in the stellar wind from an optical star. *© 2000 MAIK "Nauka/Interperiodica".*

Key words: *neutron stars, pulsars, X-ray sources*

INTRODUCTION

Vela X-1 (4U0900–403) is a long-period ($P \simeq 283$ s; McClintock *et al.* 1976) X-ray pulsar that circles the B0.5 Ib supergiant HD 77581 of mass $M_1 \simeq 23M_\odot$ and radius $R_1 \simeq 30R_\odot$ in a slightly elongated orbit ($e \simeq 0.089$) (Van Kerkwijk *et al.* 1995). This is an eclipsing binary with a component separation $a \simeq 1.7R_1$, an orbital period $P_o \simeq 8.964$ days, and an eclipse duration of ~1.72 days (Forman *et al.* 1973; Sato *et al.* 1986; Deeter *et al.* 1987; Bildsten *et al.* 1997). The neutron star in this compact system is deeply embedded in the stellar wind outflowing from the optical companion at a rate $\dot{M} \sim 4 \times 10^{-6} M_\odot\ \mathrm{yr}^{-1}$ (Nagase *et al.* 1986). Accretion from the stellar wind is most likely responsible for the X-ray emission. On the other hand, the angular momentum transferred to the neutron star during such accretion is not enough to account for the observed variations in its rotation period on a time scale of several days. Therefore, Börner *et al.* (1987) suggested that there was also an accretion disk in the system.

The source's spectral shape is typical of X-ray pulsars: a power law with a high-energy exponential cutoff, with the cutoff energy varying in the range from ~20 to 40 keV (Nagase *et al.* 1986; Kretschmar *et al.* 1997; Kreykenbohm *et al.* 1999). The spectrum is distorted at low energies by strong photoabsorption. In addition, it exhibits a fluorescence emission line of neutral iron at ~6.4 keV. Two absorption features were detected in the hard part of the spectrum at energies ~24–27 and ~54 keV, which are assumed to be produced by the resonance scattering of pulsar emission by electrons in the neutron-star magnetic field (Kretschmar *et al.* 1997; Orlandini *et al.* 1998; Kreykenbohm *et al.* 1999). At a distance $d \simeq 1.9$ kpc to the system (Sadakane *et al.* 1985), the pulsar X-ray luminosity is $L_X \simeq (1\text{–}5) \times 10^{36}$ erg s^{-1}, consistent with the assumption of accretion from the stellar wind.

Here, we present the ART-P/Granat observations of the X-ray pulsar Vela X-1 in June 1992.

OBSERVATIONS

The ART-P X-ray telescope, one of the instruments onboard the Granat International Astrophysical Observatory, is sensitive to photons at energies 2.5–60 keV (with a maximum sensitivity at 3–30 keV). There are four independent ART-P modules onboard the Observatory, each consisting of a position-sensitive detector with a geometric area of 625 cm^2, a collimator, and a coded mask. The telescope is capable of imaging a region of the sky within a $3^\circ\!.4 \times 3^\circ\!.6$ field of view with a nominal angular resolution of $\sim 5'$. The observations were carried out in "photon-by-photon" mode, in which, for each detected photon, its coordinates on the detector, energy (1024 channels), and arrival time were written into the ART-P buffer memory. This mode allowed us to perform timing (the photon arrival time was accurate to within 3.9 ms) and spectral (the energy resolution was ~22% in the 5.9-keV line) analyses of the emission from each X-ray source within the ART-P field of view. Since data transfer to the main memory was made after the temporary buffer was filled and took, on the average, 25–30 s, the written information

---

* E-mail address for contacts: aal@hea.iki.rssi.ru

Table 1. The photon flux and luminosity of the X-ray pulsar Vela X-1 as observed with ART-P in June 1992[a]

Date (UT)	Exposure, s	Flux, mCrab	L_X,[b] 10^{36} erg s^{-1}
13.638–13.692 (I)	1340	133 ± 22	1.05 ± 0.17
13.692–13.751 (II)	3650	204 ± 25	1.61 ± 0.20
13.751–13.946 (III)	12280	138 ± 11	1.09 ± 0.09
15.467–15.719 (I)	16150	13.7 ± 4.8	0.11 ± 0.04
15.719–15.787 (II)	4180	18.8 ± 6.6	0.15 ± 0.05

[a] In the 6–26-keV energy band.

[b] For the assumed distance $d = 1.9$ kpc to the source.

has the form of individual "exposures" with breaks between them. A detailed description of the telescope and its technical specifications can be found in Sunyaev *et al.* (1990).

The region of the sky with Vela X-1 was observed with ART-P twice: on June 13 and 15, 1992 (Table 1). These were among the last sessions carried out with the telescope over the entire period of its observations (a total of ~400 sessions in 2.5 years). Unfortunately, there were some technical problems. Only one module with a normal efficiency at energies $h\nu \gtrsim 6$ keV was operational [see Grebenev *et al.* (2001) for more details]. The hard telemetry channel through which information about photons with energy above 26 keV was transferred failed in the middle of both sessions (this time is indicated in Fig. 1 by a dashed line for the June 13 session). Thus, we were able to study the pulsar hard ($h\nu \gtrsim 26$ keV) emission only at the initial stage of our observations.

The first and second observations were performed at orbital phases 0.714–0.748 and 0.918–0.953, respectively. Much of the second observation was carried out during an X-ray eclipse. In what follows, the orbital phase is measured from the epoch of periastron passage (JD 2 448 789.706), as inferred from the ephemerides computed by using long-term BATSE/CGRO observations of the source (Bildsten *et al.* 1997). The eclipse period falls within the phase range 0.756–0.946 (Sato *et al.* 1986). Depending on the X-ray 6–20-keV flux (Table 1), the June 13 observing session was arbitrarily broken down into three parts, as indicated by the dotted lines in Fig. 1. The second session was divided into two parts, in accordance with the time of the source's eclipse egress. We see from Table 1 that a nonzero flux of approximately 1/10 of the bright-state flux was observed from the source during the eclipse and eclipse egress. This result is illustrated by Fig. 2. It shows images of the sky region within the ART-P field of view during the first session and during the two parts of the second session. Although the source was detected in the latter two cases at moderately high confidence levels (4.3 and 4.6σ, respectively), the detected signal excess over the background closely coincides with the source's position on the image and cannot be accidental. This is also confirmed by our timing analysis of the pulsar emission (see below).

LIGHT CURVE AND PULSE PROFILE

Figure 1a shows the ART-P 6–20-keV light curve of the pulsar on June 13 during its bright state. The curve was corrected for the background count rate and for the variations in the efficiency of observations attributable

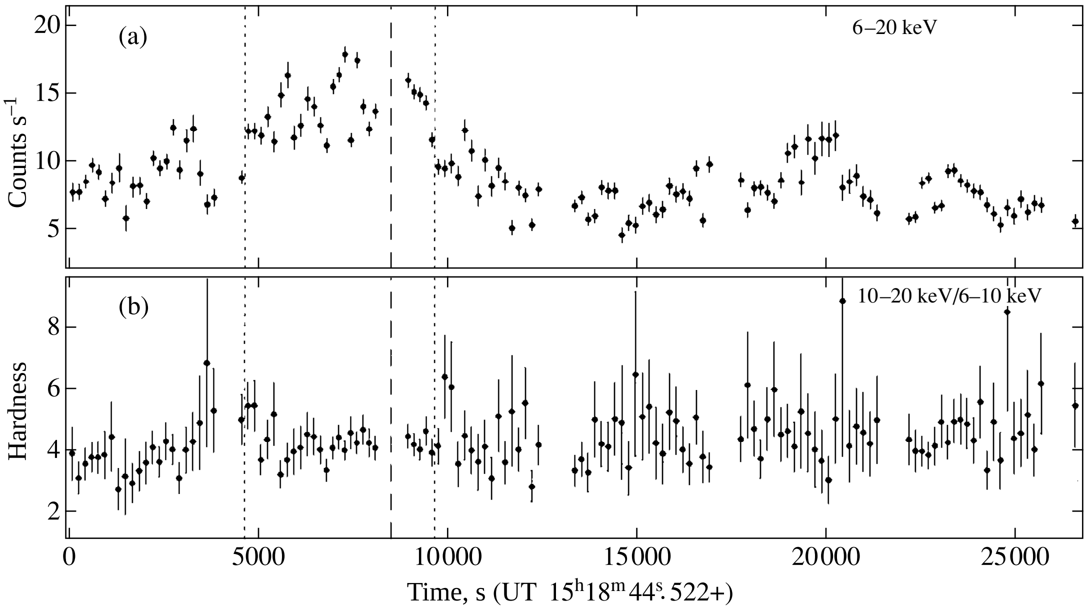

Fig. 1. (a) The ART-P 6–20-keV light curve of Vela X-1 on June 13, 1992, and (b) the corresponding variations in hardness: the ratio of count rates in the hard (10–20 keV) and soft (6–10 keV) energy bands. The errors correspond to 1σ.

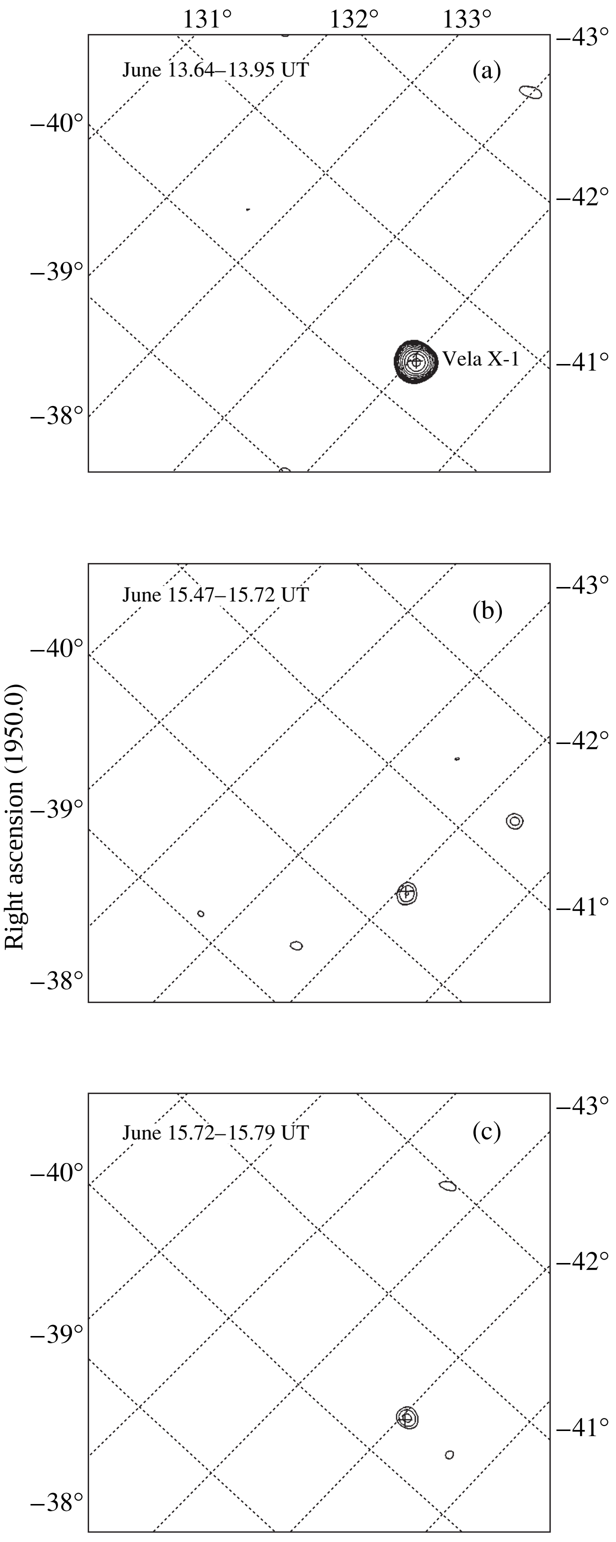

Fig. 2. ART-P 6–26-keV images of the sky region with Vela X-1 during (a) its bright state, (b) X-ray eclipse, and (c) eclipse egress. The 2.7, 3.4, 4.2, 5.3, and more σ confidence regions of the source are indicated by contours (with a logarithmic step).

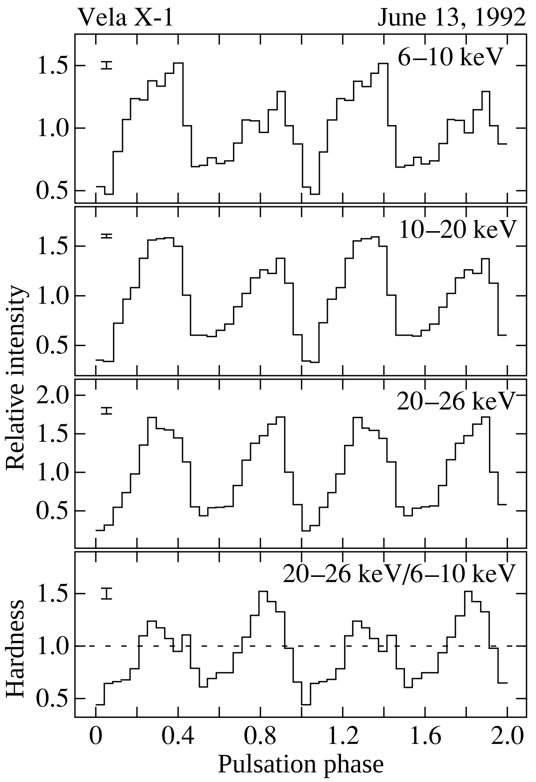

Fig. 3. Phase light curves of Vela X-1 in three energy bands. The ratio of instantaneous photon flux to period-averaged flux is plotted along the vertical axis. Hardness variations during one period are shown in the lower panel. The errors correspond to 1σ.

to a reduction in collimator transmission as the satellite (stabilized to within 30 arcmin) orientation changed. Figure 1b shows variations in the source's hardness during this session (the ratio of 10–20 and 6–10-keV photon fluxes). The integration time of each point is ~140–170 s and corresponds to the duration of a single "exposure." The figure demonstrates the variability of the pulsar on a time scale of several thousand seconds; its intensity first smoothly increased by a factor of ~1.5 and then smoothly decreased.

The small-scale (several hundred seconds) intensity variations accompanied by variations in the source's hardness are attributable to X-ray pulsations. The hardness variations are clearly seen in the lower panel of Fig. 3, which shows the evolution of the ratio of count rates in the 20–26 and 6–10-keV energy bands during one period. A comparison with the pulse profiles in the three upper panels of Fig. 3 for the 6–10-, 10–20-, and 20–26-keV energy bands indicates that the hardness increases at pulse maxima. The profiles were constructed by folding the corresponding light curves with measured period $P \simeq 283.287$ s. The arrival time of each photon was corrected for the orbital motion of the satellite and for the motion of the neutron star in the binary system. Orbital parameters were taken from Bildsten *et al.* (1997). The derived period slightly (within the 2σ

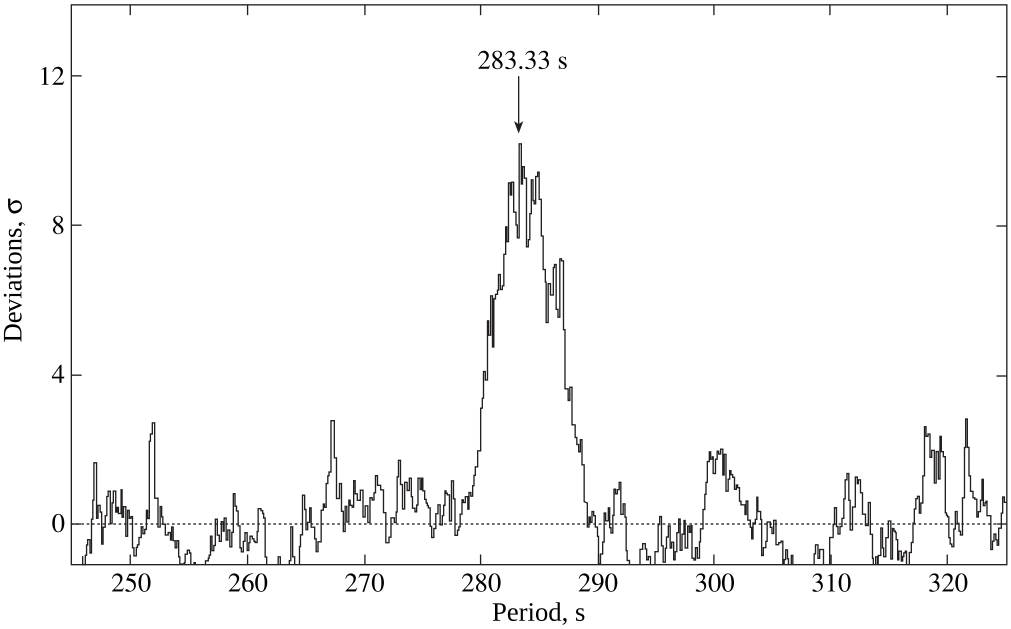

Fig. 4. The 6–26-keV periodogram for Vela X-1 constructed by the epoch-folding technique during the second part of the June 15 observing session (after eclipse egress). The amplitude of periodogram deviations from zero level is expressed in σ.

error limits) differs from $P \simeq 283.326 \pm 0.020$ s in our previous paper (Lutovinov *et al.* 1994), in which we used binary parameters from Deeter *et al.* (1987).

The pulse profiles in Fig. 3 have a double-peaked shape, characteristic of the pulsar Vela X-1. The peak width is approximately the same (~0.4 of the period) and does not depend on energy, which cannot be said about their amplitude ratio. The second peak is indistinct at $h\nu \lesssim 10$ keV; its amplitude increases at higher energies, reaching the amplitude of the first peak at $h\nu \gtrsim 20$ keV. The pulse profile changes against the background of a general increase in pulsation amplitude, as confirmed by the rise in the source's pulse fraction from $F \simeq (50.2 \pm 4.8)\%$ in the 6–10-keV band to $F \simeq (65.2 \pm 2.8)$ and $(84.5 \pm 8.8)\%$ in the 10–20- and 20–26-keV bands, respectively. Here, $F = (I_{\max} - I_{\min})/(I_{\max} + I_{\min})$, where $I_{\max}$ and $I_{\min}$ are the count rates at maximum and minimum of the pulse profile, respectively. In the broad 6–26-keV energy band, $F \simeq (69.1 \pm 2.7)\%$. Note that these are data averaged over the entire session, because, despite the source's intensity variations during the session, its pulse profile was essentially constant.

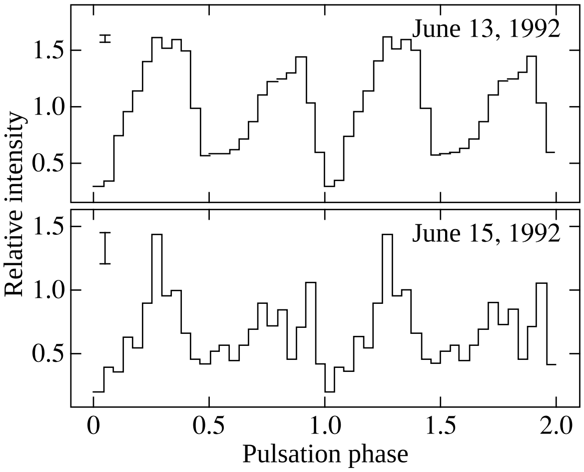

Fig. 5. Comparison of the ART-P 6–26-keV phase light curves for Vela X-1 on June 13 (during the entire session) and June 15, 1992 (after eclipse egress; during the second part of the session). The ratio of instantaneous flux to period-averaged flux is plotted along the vertical axis. The errors correspond to 1σ.

Pulsations were also detected during the second session, but only after eclipse egress of the source (part II of the session). The pulsation period was $P \simeq 283.33 \pm 1.65$ s. Figure 4 shows the periodogram constructed during this part of the session in the 6–26-keV energy band by the epoch-folding technique, and Fig. 5 shows the phase light curve in comparison with the June 13 light curve. Pulsations were detected at a 10.2σ confidence level. The pulse fraction was $(33.9 \pm 6.4)\%$; i.e., it was a factor of 2 lower than F measured in the source's bright state. During part I of the session (during the eclipse), we failed to detect such pulsations; the 3σ limit on the pulse fraction was 9.6%.

SPECTRA

The source's photon spectra for the different parts of the June 13 session are shown in Fig. 6. Because of the failure of the telemetry channel through which information about hard photons was transmitted, we used the data obtained only before the time marked by the dashed line in Fig. 1 to construct the spectrum for part II of the session. We reconstructed the spectra for parts I and II of the session up to $h\nu \sim 40$ keV and the spectrum for part III only at $h\nu \lesssim 26$ keV. The figure suggests that the source's spectrum is well described by a simple power law without evidence of a high-energy exponential cutoff, typical of most X-ray pulsars, over the entire ART-P energy range. The break energy may have been beyond the upper ART-P sensitivity limit. The spectral slope (photon index) changed during the session, generally decreasing with increasing flux from the source. To determine the parameters of the pulse-height spectra, we used the model

$$I(E) = I_{10}\left(\frac{E}{10\text{ keV}}\right)^{-\alpha}$$

$$\times \exp\left[-\tau_1\left(\frac{E}{E_1}\right)^2 \frac{W_1^2}{(E-E_1)^2+W_1^2}\right],$$

where E is the photon energy (in keV), I_{10} is the normalization of the power-law component to 10 keV (in phot. cm^{-2} s^{-1} keV^{-1}), and α is the photon index. Since the source exhibited cyclotron absorption features at energies ~27 and ~54 keV during several experiments (Kretschmar *et al.* 1997; Orlandini *et al.* 1998; Kreykenbohm *et al.* 1999), an absorption line with a Lorenz profile, centroid energy E_1, width W_1, and optical depth at the line center τ_1 was included in the model.

The interstellar absorption toward the source is low ($N_H \sim 6 \times 10^{21}$ cm^{-2}; Forman *et al.* 1973), but absorption in the stellar wind from the normal star may severely distort the spectrum at low energies. According to Sato *et al.* (1986) and Pan *et al.* (1994), the absorption column density varies with orbital phase, reaching a maximum, $N_H \sim 7 \times 10^{23}$ cm^{-2}, immediately before and after an X-ray eclipse. Since, in our case, we could not measure the photoabsorption because of the lack of data in the soft ($h\nu \lesssim 6$ keV) energy band, it was not included in the above model. Best-fit parameters for the source's pulse-height spectra during the June 13 session are listed in Table 2.

Evidence for the possible presence of a cyclotron resonance line in the source's spectrum was found only during the second part of the session. Allowance for this line improves the spectral fit, causing the χ^2_N value normalized to the number of degrees of freedom to decrease from 1.44 to 0.85. According to $\Delta\chi^2$ statistics, the probability of the corresponding chance decrease in χ^2_N is 1.24×10^{-2}, which is 2.5σ in standard deviations of the normal distribution. Thus, the confidence level for the presence of an absorption line in the pulse-height spectrum is moderately high. We mention this line only because it was detected precisely at those energies at which such an absorption feature was previously observed in this pulsar from other observatories (GINGA, Mir–Kvant, RXTE).

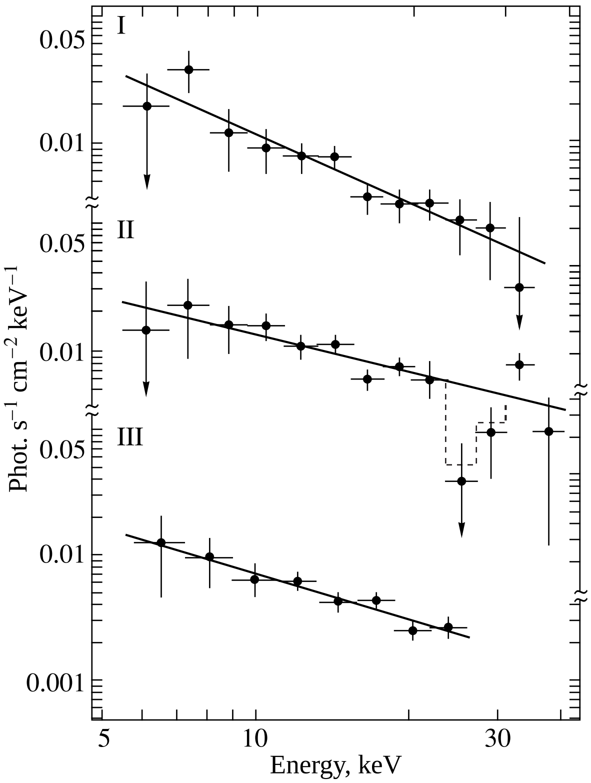

Fig. 6. Evolution of the photon spectrum for Vela X-1 as observed with ART-P on June 13, 1992. Power-law fits to the spectrum during each of the three parts of the session are indicated by solid lines. The contribution of the cyclotron absorption line is represented by a dashed line.

The source's hardness variations found on a scale of one pulsation period (see the lower panel in Fig. 3) point to a complex phase dependence of its spectral shape. Unfortunately, we were unable to perform phase-resolved spectroscopy in full, because the source was faint and because the observing time was insuffi-

Table 2. Best-fit parameters for the ART-P spectra of Vela X-1 on June 13, 1992

Part of session	I_{10}, 10^{-2} phot. cm^{-2} s^{-1} keV^{-1}	α	CL[a]
(I)	1.14 ± 0.17	1.81 ± 0.30	0
(II)	1.38 ± 0.19[b]	1.20 ± 0.26[b]	0
	1.27 ± 0.18	0.97 ± 0.28	1
(III)	0.72 ± 0.10	1.24 ± 0.22	0

[a] The presence of a cyclotron absorption line with the following parameters: $E_1 = 27.3 \pm 0.83$ keV, $\tau_1 = 3.5 \pm 2.6$, and $W_1 = 1.0$ keV (fixed).

[b] A fit in the 6–26-keV energy band for convenience of comparison with the spectrum for part III.

cient. We only compared the spectra corresponding to the two peaks in the pulse profile. The spectra were accumulated during the entire session for each phase interval equal to ~1/3 of the period. A power-law fit in the 6–26-keV energy band shows that the photon index is $\alpha \simeq 1.51 \pm 0.17$ and 1.04 ± 0.23 during the first and second peaks, respectively. Thus, the source's spectrum was harder at the second peak. Our analysis, separately for each part of the session, indicates that the spectral slope of the second peak was also subject to larger variations during the session.

CONCLUSION

The ART-P observations of the X-ray pulsar Vela X-1 in June 1992 revealed its variability on time scales from several hundred (pulse duration) to several thousand seconds. Smooth intensity variations were accompanied by changes in its spectrum: the source's spectral slope generally decreased with increasing X-ray flux and subsequently again increased as the flux declined. The hardness also varied on a scale of one pulsation period, reaching a maximum during the two peaks of the pulse profile; the pulsar flux at the second peak was considerably harder (by 30–40%) than its flux at the first peak. Such a flux dependence of the hardness caused the relative amplitude of both peaks to increase when passing from low to high energies.

Our measurements during an X-ray eclipse (its final part, which accounted for ~15% of the entire eclipse period) revealed a persistent flux at a 1/10 level of the pre-eclipse flux. This may be the emission scattered in a fairly dense stellar wind or in the extended atmosphere of the optical star. Given that the binary characteristic size, $l \sim a/c \simeq 120$ light seconds, is half the pulsation period, photons must undergo several scatterings for the pulse profile to be smeared enough. Therefore, the scattering optical depth of the wind is $\tau_T \sim 1$. A similar estimate also follows from the low-frequency absorption, $N_H \sim 7 \times 10^{23}$ cm^{-2}, observed in the spectrum of this source immediately after eclipse egress (Sato *et al.* 1986; Pan *et al.* 1994). For $\tau_T \sim 1$, the scattered-to-incident flux ratio allows us to estimate the solid angle $\Omega \sim 0.4\pi$ at which the scattering-envelope ring is seen from the compact source. Accordingly, the envelope height above the optical-star surface is

$$H \sim (R_1^2 + 0.4a^2)^{1/2} - R_1 \simeq 0.47R_1 \simeq 14R_\odot.$$

The source's pulsations were detected after eclipse egress, but their pulse fraction was ~34%, i.e., half that during the bright state. This implies that, in addition to the persistent component observed during the eclipse, the flux directly from the pulsar gave approximately the same contribution to the total flux during this time. Direct measurements show that, compared to the eclipse period, the flux rose by a factor of 1.4 ± 0.7.

We found evidence of an absorption feature at energy $E_1 \simeq 27.3$ keV in the source's pulse-height spectrum on June 13 during the second part of the session, when its X-ray flux rose by a factor of ~1.5. This feature can be associated with the resonance scattering of pulsar emission by electrons in the neutron-star magnetic field; in other words, it is the cyclotron absorption line. In this case, the neutron-star surface magnetic field is

$$B \simeq 8.6 \times 10^{10} \times \left(\frac{E_1}{1\ \text{keV}}\right)\left(1 - \frac{2GM_2}{R_2c^2}\right)^{-1/2} \text{G} \simeq 3.6 \times 10^{12}\ \text{G}.$$

Here, we took into account the gravitational redshift of the neutron star by assuming its radius and mass to be $R_2 \simeq 10$ km and $M_2 \simeq 1.9M_\odot$, respectively (van Kerkwijk *et al.* 1995).

ACKNOWLEDGMENTS

This study was supported by the Russian Foundation for Basic Research (projects nos. 98-02-17056, 99-02-18178, and 00-15-99297). We wish to thank K.G. Sukhanov, flight director, the staffs of the Lavochkin Research and Production Center, RNIIKP, and the Deep Space Communications Center in Evpatoria, the Evpatoria team of the Space Research Institute (Russian Academy of Sciences), and the team of I.D. Tserenin, and B.S. Novikov, S.V. Blagiĭ, A.N. Bogomolov, V.I. Evgenov, N.G. Khavenson, and A.V. D'yachkov from the Space Research Institute who operated the Granat Observatory, provided the scientific planning of the mission, and performed preliminary processing of the telemetry data. We also wish to thank the team of M.N. Pavlinsky (Space Research Institute) and the staff of the former Research and Development Center of the Space Research Institute in Bishkek who designed and manufactured the ART-P telescope.

REFERENCES

1. L. Bildsten, D. Chakrabarty, J. Chiu, *et al.*, Astrophys. J., Suppl. Ser. **113**, 367 (1997).
2. G. Börner, S. Hayakawa, F. Nagase, and U. Anzer, Astron. Astrophys. **182**, 63 (1987).
3. J. E. Deeter, P. E. Boynton, F. K. Lamb, and G. Zylstra, Astrophys. J. **314**, 634 (1987).
4. W. Forman, C. Jones, H. Tananbaum, *et al.*, Astrophys. J. Lett. **182**, L103 (1973).
5. S. A. Grebenev, A. A. Lutovinov, M. N. Pavlinsky, *et al.*, Pis'ma Astron. Zh. **27** (2001) (in press) [Astron. Lett. **27** (2001) (in press)].
6. P. Kretschmar, H. Pan, E. Kedziorra, *et al.*, Astron. Astrophys. **325**, 623 (1997).

7. I. Kreykenbohm, P. Kretschmar, J. Wilms, *et al.*, Astron. Astrophys. **341**, 141 (1998).
8. A. A. Lutovinov, S. A. Grebenev, R. A. Sunyaev, and M. N. Pavlinsky, Pis'ma Astron. Zh. **20**, 631 (1994) [Astron. Lett. **20**, 538 (1994)].
9. J. E. McClintock, S. Rappaport, P. C. Joss, *et al.*, Astrophys. J. Lett. **206**, L99 (1976).
10. F. Nagase, S. Hayakawa, N. Sato, *et al.*, Publ. Astron. Soc. Jpn. **38**, 547 (1986).
11. M. Orlandini, D. Dal Fiume, F. Frontera, *et al.*, Astron. Astrophys. **332**, 121 (1998).
12. H. Pan, P. Kretschmar, G. Skinner, *et al.*, Astrophys. J., Suppl. Ser. **92**, 448 (1994).
13. K. Sadakane, R. Hirata, J. Jugaku, *et al.*, Astrophys. J. **288**, 284 (1985).
14. N. Sato, S. Hayakawa, F. Nagase, *et al.*, Publ. Astron. Soc. Jpn. **38**, 731 (1986).
15. R. A. Sunyaev, S. I. Babichenko, D. A. Goganov, *et al.*, Adv. Space Res. **10**, 233 (1990).
16. M. van Kerkwijk, J. van Paradijs, E. Zuiderwijk, *et al.*, Astron. Astrophys. **303**, 483 (1995).

Translated by V. Astakhov

Astronomy Letters, Vol. 26, No. 12, 2000, pp. 772–778. Translated from Pis'ma v Astronomicheskiĭ Zhurnal, Vol. 26, No. 12, 2000, pp. 899–906.
Original Russian Text Copyright © 2000 by Sibgatullin, Sunyaev.

Energy Release on the Surface of a Rapidly Rotating Neutron Star during Disk Accretion: A Thermodynamic Approach

N. R. Sibgatullin[1, 2]* and R. A. Sunyaev[2, 3]

[1] *Moscow State University, Vorob'evy gory, Moscow, 119899 Russia*
[2] *Max-Planck-Institut fuer Astrophysik, Karl Schwarzschild Strasse 1, 86740 Garching bei Muenchen, Germany*
[3] *Space Research Institute, Russian Academy of Sciences, ul. Profsoyuznaya 84/32, Moscow, 117810 Russia*

Received February 28, 2000

Abstract—The total energy E of a star as a function of its angular momentum J and mass M in the Newtonian theory, $E = E(J, M)$ [in general relativity, the gravitational mass of a star as a function of its angular momentum J and rest mass m, $M = M(J, m)$], is used to determine the remaining parameters (angular velocity, chemical potential, etc.) in the case of rigid rotation. Expressions are derived for the energy release during accretion onto a cool (with constant entropy), rapidly rotating neutron star (NS) in the Newtonian theory and in general relativity. A separate analysis is performed for the cases where the NS equatorial radius is larger and smaller than the radius of the marginally stable orbit in the disk plane. An approximate formula is proposed for the NS equatorial radius for an arbitrary equation of state, which matches the exact equation of state at $J = 0$. *© 2000 MAIK "Nauka/Interperiodica".*

Key words: *neutron stars, luminosity, disk accretion, X-ray bursters*

INTRODUCTION

The change in mass and angular momentum of a cool neutron star (NS) during accretion leads to a transformation of its equilibrium state. Below, we consider NSs with weak magnetic fields that do not affect the accretion dynamics; i.e., our results refer to the accretion pattern in low-mass X-ray binaries and, in particular, in X-ray bursters. Of crucial importance is the question of what part of the energy released during accretion dissipates near and outside the stellar surface (in the accretion disk, in the boundary layer, in the spread layer, in the settling zone as matter is compressed under the weight of the newly supplied material, when uniform rotation is established by viscous forces throughout the entire extended stellar atmosphere, and in the zone with a surface density of the order of 10^9 g cm^{-2} subject to nuclear burning during X-ray flares) and what part dissipates inside the star in its interior. Observationally, these two zones of energy release differ radically. The energy released near the surface leaves the surface layers (is emitted) in a very short time, from fractions of a millisecond to several tens of seconds, although the complete energy dissipation can last for several hours. By contrast, the energy release in the stellar interior produces radiation with characteristic times exceeding hundreds of thousands and, possibly, millions of years; this is the time it takes for the interiors of neutron stars with weak magnetic fields to cool down (Levenfish *et al.* 1999). Such radiation can be detected only in highly variable transients when accretion on them virtually ceases.

Here, we disregard energy release in the stellar interior by assuming that the star is cool and that its entropy does not change during accretion and transformation of the NS internal structure. This strong assumption allowed us to obtain a number of general results, which we used previously (Sibgatullin and Sunyaev 2000). Note that this assumption does not hold in the so-called thermal neutron stars, where the spinup via accretion leads to a difference between the angular velocities of the crust and the central liquid superfluid core inside the star. As a result, energy is released inside the star through viscous friction [see Alpar (1999) for a discussion].

A thermodynamic relation between the change in NS total energy (gravitational mass in general relativity) and the change in its angular momentum and mass (rest mass in general relativity) is considered for cool, rigidly rotating NSs with a given equation of state (EOS). This relation and the energy conservation law are used to derive a formula for the energy release on the stellar surface (in the Newtonian approximation and in general relativity) during disk accretion onto a NS rotating with an arbitrary angular velocity. The case where the NS equatorial radius is smaller than the radius of the marginally stable orbit is also considered in terms of general relativity.

For the equilibrium figure of a rotating, incompressible fluid in its own gravitational field (Maclaurin spheroid), we derive explicit formulas for the depen-

---

* E-mail address for contacts: sibgat@mech.math.msu.su

dence of disk and surface energy release on spheroid eccentricity. The fraction of disk energy release in the total energy release is shown to be expressed by a simple linear dependence on the ratio of the Maclaurin-spheroid rotation frequency to the Keplerian equatorial particle velocity.

A universal approximate formula for the NS equatorial radius is derived for an arbitrary EOS.

Previously (Sibgatullin and Sunyaev 2000), we considered astrophysical implications of our results and methods for deriving simple approximation formulas. We also analyzed the universal geometric properties of space–time outside rotating bodies.

NEWTONIAN TREATMENT

In the Newtonian approximation, the total energy of a NS consists of the gravitational, kinetic, and internal energies:

$$\mathcal{E} = \int_V \left(-\frac{1}{2}\Phi(\bar{r}) + \frac{1}{2}\Omega^2(x^2+y^2) + u(\rho(\bar{r}))\right)\rho(\bar{r})dV, \tag{1}$$

where the gravitational potential Φ is

$$\Phi(\bar{r}) = G\int_V \frac{\rho(\bar{r}')}{|\bar{r}-\bar{r}'|}dV'. \tag{2}$$

We take a model of an ideal gas with constant (zero) entropy for the internal energy of superdense matter. The Gibbs identity then yields

$$du = -pd(1/\rho) + Tds = -pd(1/\rho). \tag{3}$$

We have the following obvious expressions for the NS mass and angular momentum:

$$M = \int_V \rho(\bar{r})dV, \quad J = \int_V \rho(\bar{r})(x^2+y^2)\Omega dV. \tag{4}$$

The following integral holds in a steady equilibrium state:

$$u(\rho) + \frac{p}{\rho} - \Omega^2(x^2+y^2)/2 - \Phi = \mu = \text{const}, \tag{5}$$

since μ has the same value at any point of the star[1], because the equilibrium is isentropic and because the rotation is rigid [the theorem of Crocco (1937); see also Oswatitsch (1976), Chernyi (1988)]. So, the dynamical equilibrium conditions can also be written as $\nabla\mu = 0$ [see the case of an incompressible fluid in Lamb (1947)].

Let us consider two close equilibrium states with global parameters $\mathcal{E}, M, J, \Omega$ and $\mathcal{E} + \delta\mathcal{E}, M + \delta M, J + \delta J, \Omega + \delta\Omega$.

Theorem 1. *The variations of* NS *mass δM, angular momentum δJ, and total energy δE for two close equilibrium states are related by the thermodynamic relation*

$$\delta\mathcal{E} = \Omega\delta J + \mu\delta M. \tag{6}$$

We denote the local displacement of point $\bar{r}$ on the stellar surface along the normal when passing from one equilibrium state to the other by $W(\bar{r})$. For an arbitrary integral $\int_V a(\bar{r})dV$, we then have

$$\delta A = \int_V \delta a(\bar{r})dV + \int_{\partial V} a(\bar{r})W(\bar{r})dS. \tag{7}$$

In view of Eq. (2) for the gravitational potential, the variation of gravitational energy $\delta\mathcal{E}_{\text{gr}}$ is

$$\delta\mathcal{E}_{\text{gr}} = -\frac{1}{2}\int_V \delta\rho\Phi dV - \frac{1}{2}\int_V \rho\delta\Phi dV - \frac{1}{2}\int_{\partial V} \rho W\Phi dS.$$

Reversing the order of integration in the second term on the right-hand side, we reduce this expression to

$$\delta\mathcal{E}_{\text{gr}} = -\int_V \delta\rho\Phi dV - \int_{\partial V} \rho W\Phi dS. \tag{8}$$

We calculate the variation of internal energy $\delta\mathcal{E}_{\text{in}}$ from formula (7) by using the Gibbs identity (3):

$$\begin{aligned}\delta\mathcal{E}_{\text{in}} &= \delta\int_V u(\rho)\rho dV \\ &= \int_V \left(u(\rho) + \frac{p(\rho)}{\rho}\right)\delta\rho dV + \int_{\partial V} \rho W\left(u(\rho) + \frac{p}{\rho}\right)dS.\end{aligned} \tag{9}$$

In order to simplify the subsequent calculations, we added the surface term $\int_{\partial V} WpdS$ to the right-hand part of (9); this term is zero, because the pressure vanishes at the stellar boundary. Clearly, the variation of kinetic energy can be expressed as

$$\begin{aligned}\delta\mathcal{E}_{\text{c}} &= \frac{1}{2}\int_V (\delta\rho\Omega + 2\delta\Omega\rho)(x^2+y^2)\Omega dV \\ &+ \frac{1}{2}\int_{\partial V} \Omega^2\rho(\bar{r})(x^2+y^2)WdS.\end{aligned}$$

As a result, the variation of total energy $\delta\mathcal{E} = \delta\mathcal{E}_{\text{gr}} + \delta\mathcal{E}_{\text{in}} + \delta\mathcal{E}_{\text{c}}$ is

$$\begin{aligned}\delta\mathcal{E} &= \int_V \Bigg\{\delta\rho\left(-\Phi + \frac{1}{2}\Omega^2(x^2+y^2) + u(\rho) + p/\rho\right) \\ &+ \delta\Omega\Omega(x^2+y^2)\Bigg\}dV + \int_{\partial V} \rho W\Bigg(-\Phi + u(\rho) \\ &+ p/\rho + \frac{1}{2}\Omega^2(x^2+y^2)\Bigg)dS.\end{aligned}$$

---

[1] The constant μ should not be confused with the Bernoulli integral i_0, which is constant along a streamline: $\mu = i_0 - [r, \omega]^2$!

The quantities δM and δJ are given, respectively, by

$$\delta M = \int_V \delta\rho(\bar{r})dV + \int_{\partial V} \rho(\bar{r})W(\bar{r})dS,$$

$$\delta J = \int_V (\Omega\delta\rho(\bar{r}) + \delta\Omega\rho(\bar{r}))(x^2+y^2)dV \qquad (10)$$

$$+ \int_{\partial V} \Omega\rho(\bar{r})(x^2+y^2)WdS.$$

Regrouping the terms, we represent the expression for $\delta\mathscr{E}$ as

$$\delta\mathscr{E} = \int_V \left\{\delta\rho\left(-\Phi - \frac{1}{2}\Omega^2(x^2+y^2) + u(\rho) + \frac{p}{\rho}\right)\right\}dV$$

$$+ \int_V \{\delta\rho\Omega + \delta\Omega\rho\}(x^2+y^2)\Omega dV \qquad (11)$$

$$+ \int_{\partial V} \Omega\rho(\bar{r})(x^2+y^2)WdS + \int_{\partial V} \rho W\left(-\Phi + u(\rho) + \frac{p}{\rho}\right.$$

$$\left. - \frac{1}{2}\Omega^2(x^2+y^2)\right)dS.$$

The coefficients in front of $\delta\rho$ in the first and last integrals of Eq. (11) match the constant μ given by (5). Let us now make use of Crocco's theorem and factor this constant outside the integral signs. The angular velocity Ω can also be factored outside the integral signs in the second and third integrals because the rotation is rigid. Having done these operations and using formula (7) for δM and δJ, we obtain

$$\delta\mathscr{E} = \Omega\delta J + \mu\delta M,$$

hence,

$$\Omega = \left.\frac{\partial\mathscr{E}}{\partial J}\right|_M, \quad \mu = \left.\frac{\partial\mathscr{E}}{\partial M}\right|_J. \qquad (12)$$

We see that the constant μ has the physical meaning of chemical potential here (Landau and Lifshitz 1976).

Theorem 1 is conceptually associated with the following remarkable variational principle of general relativity by Hartle and Sharp (1967) (see also Bardeen 1970): the true mass and angular-momentum distributions differ from their virtual (possible) distributions with a fixed rest mass and a fixed total angular momentum in that they give a conditional extremum to the gravitational mass (energy in the Newtonian approximation). In this case, the angular velocity Ω and the constant μ act as the Lagrangian factors.

Corollary 1. *When a star loses its angular momentum and energy by the radiation of electromagnetic or gravitational waves, the rates of change in its total energy and angular momentum are related by* $\dot{\mathscr{E}} = \Omega\dot{J}$.

This equality follows from (12), because the change in NS baryonic mass is zero during wave emission. Corollary 1 was proved by Ostriker and Gunn (1969) when considering the fluxes of angular momentum and energy of electromagnetic or gravitational radiation in the wave zone. It has important applications for radio pulsars: the quasi-equilibrium evolution of the NS structure when it loses its angular momentum does not lead to any heating of the stellar matter.

Denote the fluxes of angular momentum and energy on the NS by $\dot{M}l$ and $\dot{M}e$, respectively, where l and e have the meaning of the specific angular momentum and specific energy brought by the accreting matter.

Theorem 2. *When the angular momentum* $\dot{M}l$ *and energy* $\dot{M}e$ *are transferred to a neutron star by accreting particles in unit time, the following energy is released in the star with constant entropy in unit time:*

$$L_s = \dot{M}(e - \Omega l - \mu), \qquad (13)$$

where μ is the chemical potential of the cool star.

Indeed, according to Theorem 1, we have

$$\delta\mathscr{E} = \Omega dJ + \mu dM.$$

On the other hand, it follows from the energy conservation law that

$$d\mathscr{E} = dMe - L_s dt,$$

where L_s is the rate of energy release (stellar luminosity) during accretion.

From the law of conservation of angular momentum, we have

$$dJ = \dot{M}ldt. \qquad (14)$$

By equating the expressions for dE from Theorem 1 and from the energy conservation law and using (14) for dJ, we reach the conclusion of Theorem 2.

Note. For the constant μ, we may choose its value at the stellar equator: $\mu = -\frac{1}{2}\Omega^2R^2 - \Phi_e$, where Φ_e is the gravitational potential at the stellar equator, and R is the equatorial radius. Here, we make use of the fact that the enthalpy vanishes on the stellar surface. This choice of μ allows us to determine the equatorial radius, the most important NS parameter [see formulas (32) and (33)].

The local justification is as follows. Falling on the stellar equator, a particle of mass m increases the NS moment of inertia. An additional work is done, which is equal to the difference between the particle angular momenta in the Keplerian orbit, $mR^2\Omega_K$, and on the stellar surface, $mR^2\Omega$, multiplied by the NS angular velocity Ω. This work is equal, with an opposite sign, to the additional (rotational) energy that must be added to the difference between the particle kinetic energies in the Keplerian orbit, $mR^2\Omega_K^2/2$, and on the stellar surface, $mR^2\Omega^2/2$. Therefore, when a particle approaches the NS from a thin accretion disk and decelerates in a narrow boundary layer at the equator from the Keplerian angular velocity Ω_K to the NS rotation velocity, it releases the energy $1/2m(\Omega_K - \Omega)^2R^2$, giving its angular momentum and part of its energy to the star. The formula for the energy release in this form was justified by Kluzniak (1987). The various local derivations of this formula were discussed by Kley (1991), Popham and Narayan (1995), and Sibgatullin and Sunyaev (1998).

It should be noted that, having accreted at the equator, the matter cannot remain there for long. It must spread in some way over the surface while changing its angular momentum and energy. Therein lies the inconsistency of the local approach, which disregards the subsequent redistribution of accreting matter over the star. The close match between the energy release given by (13) and the energy released when particles decelerate from the velocity $R\Omega_K$ to the velocity ΩR on the stellar surface is fairly unexpected.

Here, we make an attempt to solve the problem by taking into account the restructuring of a cool star during accretion. This global approach leads to formula (13). Thus, (13) holds not only for a narrow boundary layer near the equator (Popham and Sunyaev 2000). Our derivation of Corollary 1 from Theorem 1 suggests that the same energy is released by a particle in the spread layer (Inogamov and Sunyaev 1999), although the situation in the spread layer differs radically from the problem with a thin equatorial boundary layer. In the surface layer, the matter heats up, the thermal energy radiates away in bright latitudinal rings, and other complex physical processes accompanying the spread of matter over an equipotential of a rapidly rotating star take place. However, this all affects the instantaneous equilibrium of a neutron star only through global changes in its baryonic mass and angular momentum. It is pertinent to recall that, according to Huygens's theorem (see, e.g., Tassoul 1978), the work done by gravitational and centrifugal forces on a particle to move it over the surface of a rigidly rotating liquid body in its own gravitational field is zero.

The close coincidence between the energy release according to Eq. (13a) and energy, released when particles decelerate from velocity $R\Omega_K$ to particle velocity on the stellar surface ΩR, is rather unexpected.

Corollary 1. *When a thin accretion disk is adjacent to the stellar equator and when the star transforms into an equilibrium state with a new mass and angular momentum in time dt, the energy* $\frac{1}{2}dM(\Omega_K - \Omega)^2R^2$ *is released on the stellar surface, where dM is the amount of baryonic mass accreted onto the* NS *in time dt and* Ω_K *and* Ω *are the Keplerian velocity at the* NS *equator and its angular velocity, respectively.*

Indeed, in this case, $e = v^2/2 - \Phi_e$, $v = R\Omega_K$, $l = R^2\Omega_K$, and expression (13) for L_s turns into a full square. In particular, it follows from Corollary 1 that the energy release for counterrotation at $|\Omega| = 0.5\Omega_K$ is a factor of 9 larger than the energy release for corotation!

Corollary 2. *Since the kinetic energy* $\dot{M}v^2/2$ *of the decelerated matter is released during spherical accretion onto a nonrotating cool star at rate* $\dot{M}$ *in its surface layer in unit time, there is no volume energy release in this case either.*

This assertion follows from Theorem 2, because, in this case, $l = \Omega = 0$, $\Phi = \Phi_e = GM/R$, and the total energy release given by (13) matches the surface energy release.

Disk energy release. Passing from one Keplerian orbit to another with a smaller radius, an accreting particle loses its energy through viscous friction, which radiates away. The total energy radiated away by one particle from an infinitely distant point before it approaches a Keplerian circular orbit on the stellar surface is equal to the particle energy in this orbit, with an opposite sign. Therefore, the following formula holds for the energy release of the entire disk:

$$L_d = -\dot{M}(R^2\Omega_K^2/2 - \Phi_e). \tag{15}$$

Setting the sum of centrifugal and gravitational forces equal to zero yields

$$R\Omega_K^2 = -\frac{d\Phi}{dr}\bigg|_{r=R}. \tag{16}$$

The formula for the disk energy release follows from (15) and (16):

$$L_d = \frac{1}{2R}\frac{d(r^2\Phi)}{dr}\bigg|_{r=R}. \tag{17}$$

If there is no rotation, then $L_d = L_s = \dot{M}GM/2R$ (Shakura and Sunyaev 1973).

In order to estimate the effect of NS rotation on the disk energy release, let us consider an example in which the stellar matter is modeled by an ideal, incompressible fluid. In this case, the axisymmetric equilibrium figure is a Maclaurin spheroid. The Dirichlet formula (see, e.g., Lamb 1947) can be used for the gravitational potential of a homogeneous ellipsoid, and the following expression can be derived for L_d from (17) (below, e denotes the spheroid eccentricity, $e \equiv \sqrt{1 - c^2/a^2}$):

$$L_d = \dot{M}\frac{3GM}{2a}\left(\frac{e^2-1}{e^3}\arcsin e + \frac{\sqrt{1-e^2}}{e^2}\right). \tag{18}$$

The Keplerian equatorial rotation frequency can be calculated from (16):

$$f_{\mathrm{K}} = \sqrt{G\rho/2\pi}B(e);$$

$$B(e) \equiv \sqrt{\frac{\sqrt{1-e^2}}{e^3}\arcsin e - \frac{1-e^2}{e^2}}. \quad (19)$$

The formula for the rotation frequency is (Lamb 1947)

$$f = \sqrt{G\rho g(e)/2\pi},$$

$$g(e) \equiv \frac{\sqrt{1-e^2}}{e^3}(3-2e^2)\arcsin e - 3\frac{1-e^2}{e^2}. \quad (20)$$

According to Corollary 1 of Theorem 2 and formulas (19) and (20), the energy release on the NS surface is

$$\begin{aligned} L_{\mathrm{s}} &= \frac{1}{2}\dot{M}(\Omega_{\mathrm{K}} - \Omega)^2 R^2 \\ &= \frac{3GM}{4R}\left(\sqrt{\frac{3-2e^2}{e^3}\arcsin e - 3\frac{\sqrt{1-e^2}}{e^2}}\right. \quad (21) \\ &\quad \left. - \sqrt{\frac{\arcsin e}{e^3} - \frac{\sqrt{1-e^2}}{e^2}}\right)^2. \end{aligned}$$

Using (18)–(21), we can obtain the following unexpectedly simple relation to estimate the fraction of radiation from the disk in the NS total radiation:

$$L_{\mathrm{d}}/(L_{\mathrm{s}} + L_{\mathrm{d}}) = 0.5(1 + f/f_{\mathrm{K}}). \quad (22)$$

Note that the eccentricity $e \longrightarrow 1$ as $\Omega \longrightarrow \Omega_{\mathrm{K}}$ for an incompressible fluid. Therefore, the spheroid asymptotically transforms into a plane disk. However, large angular velocities cannot be reached: Maclaurin spheroids become unstable to quadrupole perturbations at $e > 0.8127$ (at $\Omega > 0.4326\sqrt{2\pi G\rho}$) (Lamb 1947; Chandrasekhar 1973).

According to (18) and (21), the total luminosity $L_{\mathrm{s}} + L_{\mathrm{d}}$ in the stability range of Maclaurin spheroids satisfies the inequalities

$$0.0485 < \frac{L_{\mathrm{s}} + L_{\mathrm{d}}}{\dot{M}c^2}\left(\frac{M}{1.4M_{\odot}}\right)^{-2/3}\left(\frac{\rho}{10^{14}\ \mathrm{g/cm^3}}\right)^{-1/3} < 0.0549$$

in the case of corotation and the inequalities

$$0.0549 < \frac{L_{\mathrm{s}} + L_{\mathrm{d}}}{\dot{M}c^2}\left(\frac{M}{1.4M_{\odot}}\right)^{-2/3}\left(\frac{\rho}{10^{14}\ \mathrm{g/cm^3}}\right)^{-1/3} < 0.1953$$

in the case of counterrotation. The speed of light (constant) was introduced here for convenience of comparing the results in the Newtonian approximation and in general relativity (Sibgatullin and Sunyaev 2000).

For the critical $e = 0.8127$, the ratio of angular velocities $\Omega/\Omega_{\mathrm{K}}$ is 0.602. It thus follows from formula (22) (in the stability range of Maclaurin spheroids) for spheroid and disk corotation that $0.199 < L_{\mathrm{s}}/(L_{\mathrm{s}} + L_{\mathrm{d}}) < 0.5$; $L_{\mathrm{s}}/(L_{\mathrm{s}} + L_{\mathrm{d}}) = 0.5$ for a nonrotating star (Shakura and Sunyaev 1973). The inequality $0.5 < L_{\mathrm{s}}/(L_{\mathrm{s}} + L_{\mathrm{d}}) < 0.801$ holds for disk and spheroid counterrotation.

TREATMENT IN GENERAL RELATIVITY

The metric of stationary, axisymmetric spaces invariant to the change $t, \phi \longrightarrow -t, -\phi$ can be written in cylindrical r, z, ϕ coordinates as

$$ds^2 = a^2dt^2 - b^2(d\phi - \omega dt)^2 - e^{2\sigma}(dr^2 + dz^2), \quad (23)$$

where a, b, and σ are the sought-for functions of r and z. The gravitational-mass functional in the steady-state, axisymmetric case is (Hartle and Sharp 1967)

$$\begin{aligned} Mc^2 &= c^4\int\limits_{\infty}\frac{R}{16\pi G}\sqrt{-g}d\phi drdz \\ &\quad + c^{-1}\int\limits_{V}T_0^0\sqrt{-g}d\phi drdz, \end{aligned} \quad (24)$$

where V and ∂V are the region occupied by the star and its boundary, respectively. The integral of the scalar curvature is extended to the entire three-dimensional space:

$$T_0^0 = (p + \varepsilon)\frac{(a^2 + \omega\Omega b^2)}{a^2 - (\omega - \Omega)^2 b^2} - p,$$

$$\sqrt{-g} = abe^{2\sigma}.$$

The NS nuclear overcompressed matter is an ideal isentropic gas with a given internal energy density, $\varepsilon = \rho u(\rho)$, with $d\varepsilon = (p + \varepsilon)d\rho/\rho$.

According to formula (24), the mass functional for a steady-state, axisymmetric star is determined by the functions ρ, a, b, and σ of independent variables r and z and by the constant Ω. Let us consider two close equilibrium states A and $A + \delta A$. Subtracting the mass functional in state A from the mass functional in state $A + \delta A$ yields

$$\begin{aligned} \delta M &= 2\pi\int\left(\delta\rho\frac{\delta M}{\delta\rho} + \delta\sigma\frac{\delta M}{\delta\sigma} + \delta a\frac{\delta M}{\delta a} + \delta b\frac{\delta M}{\delta b}\right)drdz \\ &\quad + \delta\Omega\frac{\partial M}{\partial\Omega} + c^{-3}\int\limits_{\partial V}T_0^0 W\sqrt{-g}dl. \end{aligned}$$

The functions of the form $\delta M/\delta a$ are variational derivatives of the functional M with respect to the corresponding function $a(r, z)$.

Since the metric coefficients and their first derivatives are continuous at the boundary of the region ∂V, the surface terms from variations of the gravitational mass reduce to the integral over a distant surface at pseudo-Euclidean infinity, where they vanish. The variational derivatives of M with respect to the metric coefficients are zero by virtue of the Einstein equations.

Using the equalities $u^0u_0 + u^\phi u_\phi = 1$ and $u^\phi = \Omega u^0$, we can derive the following formula at fixed metric coefficients:

$$\delta u^0 = -u_\phi (u^0)^2 \delta\Omega. \tag{25}$$

If we vary the gravitational-mass functional (25) at given metric coefficients, we then obtain

$$\begin{aligned} \delta Mc^2 &= 2\pi c^{-1}\delta\int_V T_0^0\sqrt{-g}\,drdz \\ &= 2\pi c^{-1}\delta\int_V (\varepsilon - T_\phi^0\Omega)\sqrt{-g}\,drdz. \end{aligned} \tag{26}$$

We now use the expressions for rest mass m and angular momentum J (Hartle and Sharp 1967)

$$m = 2\pi\int_V \rho u^0\sqrt{-g}\,drdz,$$

$$J = -2c^{-1}\pi\int_V T_\phi^0\sqrt{-g}\,drdz$$

and the relativistic integral of dynamical equilibrium conditions

$$\frac{p+\varepsilon}{(\rho c u^0)} = \mu = \text{const.}$$

In view of (24), the following formula holds:

$$\begin{aligned} \delta\varepsilon &= \frac{p+\varepsilon}{\rho}\delta\rho = \frac{p+\varepsilon}{\rho u^0}(\delta(\rho u^0) - \rho\delta u^0) \\ &= \frac{p+\varepsilon}{\rho u^0}\delta(\rho u^0) + T_\phi^0\delta\Omega. \end{aligned}$$

The quantity δM can then be easily represented after reducing similar terms in (26) as

$$\delta Mc^2 = \Omega\delta J + \mu\delta m; \tag{27}$$

hence,

$$\Omega = \left.\frac{\partial Mc^2}{\partial J}\right|_m, \quad \mu = \left.\frac{\partial Mc^2}{\partial m}\right|_J. \tag{28}$$

Theorem 3. *For any two close isentropic equilibrium states of a* NS, *the variations in gravitational mass, angular momentum, and rest mass are related by (28).*

Energy release during disk accretion onto a NS in general relativity. Let us now use Theorem 3 to calculate the NS radiation and evolution from equilibrium states. The constant in the relativistic case is also convenient to estimate from its value at the stellar equator:

$$\mu = c/u^0 = c\sqrt{a^2 - (\omega - \Omega)^2 b^2}; \tag{29}$$

the metric coefficients (23) are taken at the stellar equator.

In general relativity, the NS equatorial radius can be larger and smaller than the radius of the marginally stable orbit, which is equal to three gravitational radii when the star does not rotate (Kluzniak and Wagoner 1985; Sunyaev and Shakura 1986). For slow rotation of NS, its external field cannot be described by the Kerr solution linearized in angular momentum. The physical processes in the field of a slowly rotating NS were considered by Kluzniak and Wagoner (1985), Sunyaev and Shakura (1986), Biehle and Blanford (1993), and Miller and Lamb (1996). In the former case, we denote the energy and angular momentum of a test particle of unit mass in a Keplerian orbit with the NS radius by e and l, respectively, take into account the law of conservation of angular momentum $dJ = ldm$, and equate the expressions for the change in gravitational mass from Theorem 3 and from the law of conservation of energy:

$$(\Omega l + \mu)dm = dme - L_s dt.$$

We use the equalities $e = c(u_K)_0$, $l = c(u_K)_\phi$, $\mu = c/u^0$, and $u^\phi = \Omega u^0$, and express L_s as

$$\begin{aligned} L_s &= \dot{M}(e - \Omega l - \mu) = \mu(\mathbf{u}\cdot\mathbf{u}_K - 1)\dot{M}, \\ \frac{dm}{dt} &= \dot{M}. \end{aligned} \tag{30}$$

Here, we introduced the designation for a scalar product of the 4-velocity vector of a particle rotating with the NS angular velocity and the 4-velocity vector of a particle rotating in a Keplerian orbit at the same point on the stellar equator. Expression (30) for L_s is always positive and becomes zero if the NS angular velocity reaches the Keplerian one at the stellar equator. In our previous paper (Sibgatullin and Sunyaev 2000), we gave approximation formulas for the dependences of M, e, l, and f_K on Kerr parameter and rest mass for particles in equatorial Keplerian orbits for a NS with EOS A and FPS. We used (28) to calculate the NS angular velocity and chemical potential. For stars with EOS A and FPS and with a gravitational mass of $1.4M_\odot$, we derived approximation formulas for the dependences of total luminosity $L_s + L_d$ and $L_s/(L_s + L_d)$ ratio on NS angular velocity by using (30).

The case where the NS radius is smaller than the radius of the marginally stable orbit is characteristic of general relativity alone. In this case, the gravitational field does an additional work on the spiraling-in particles in the gap; no stable Keplerian orbits exist within the marginally stable orbit. Thus, the rate of energy release is

$$L_s = \dot{M}(e_* - \Omega l_* - \mu) = \mu(\mathbf{u}\cdot\mathbf{u}_* - 1)\dot{M}, \tag{31}$$

where $\mathbf{u}_*$ denotes the 4-velocity vector of the particle that fell on the stellar surface from a circular marginally stable orbit with the energy e_* and angular momentum l_* corresponding to this orbit. In our previous paper (Sibgatullin and Sunyaev 2000), we gave universal (valid for an arbitrary equation of state) approximation formulas for the dependences of e_*, l_*, R_*, and f_K^* on Kerr parameter and on dimensionless quadrupole coefficient b for the particles falling on the surface from circular marginally stable orbits. We constructed plots of total luminosity against angular velocity for a NS with gravitational mass $M = 1.4M_\odot$ by using (27) and (30).

Note the fundamental difference between our formulas (30), (31) for the luminosity and formulas (16), (18) from Thampan and Datta (1998). These authors calculated the energy release produced by particles during accretion as a difference between the particle energy in the stable circular equatorial orbit nearest the body and the energy of the particles lying on the equator and corotating with the body.

Using Theorem 3 to calculate the NS angular velocity and equatorial radius. As the NS parameters, we choose its rest mass and Kerr parameter j (dimensionless angular momentum cJ/GM^2). The methods of constructing the function $M(j, m)$ were developed previously (Sibgatullin and Sunyaev 2000).

According to (28), the NS *angular velocity at given rest mass m and Kerr parameter j can be determined from the known function M(j, m) by using the formula*

$$\Omega GM/c^3 = \frac{M_{,j}|_m}{M + 2jM_{,j}|_m},$$

where $M_{,j}|_m = \left.\frac{\partial M}{\partial j}\right|_m$.

Another important formula that relates the constant μ to a derivative of the gravitational mass with respect to the rest mass at constant angular momentum follows from (28). Taking (29) for μ, we obtain

$$c\frac{MM_{,m}|_j}{M + 2jM_{,j}|_m} = \sqrt{a^2 - b^2(\Omega - \omega)^2}, \quad R = b, \qquad (32)$$

where R is the geometric equatorial radius of the star (the equator length divided by 2π); the metric coefficients a and b are taken at the NS equator.

In the static case, the NS radius can be determined from (32) by using the Schwarzschild metric ($\omega = \Omega = 0$, $a^2 = c^2\left(1 - \frac{2GM}{Rc^2}\right)$):

$$\frac{Rc^2}{GM} = \frac{2}{1 - M_{,m}^2}. \qquad (33)$$

Remarkably, formula (33) [if $M(j, m)$ is substituted into it and differentiated at constant j) closely agrees with the numerical data from Cook *et al.* (1994) and Stergioulus (1998) for the equatorial radius of a rotating NS, to within a few percent: $R \approx 2GM/(c^2 - c^2M_{,m}^2|_j)$.

ACKNOWLEDGMENTS

We wish to thank N. Stergioulus for the use of his numerical code, made available by him on the Internet.

REFERENCES

1. M. A. Alpar, astro-ph/9912228.
2. J. M. Bardeen, Astrophys. J. **162**, 71 (1970).
3. G. Biehle and R. D. Blandford, Astrophys. J. **411**, 302 (1993).
4. S. Chandrasekhar, *Ellipsoidal Figures of Equilibrium* (Yale Univ. Press, New Haven, 1969; Mir, Moscow, 1973).
5. G. G. Chernyĭ, *Gas Dynamics* (Nauka, Moscow, 1988).
6. G. B. Cook, S. L. Shapiro, and S. A. Teukolsky, Astrophys. J. **424**, 823 (1994).
7. L. Crocco, ZAMM **17**, 1 (1937).
8. J. B. Hartle and D. H. Sharp, Astrophys. J. **147**, 317 (1967).
9. N. A. Inogamov and R. A. Sunyaev, Pis'ma Astron. Zh. **25**, 323 (1999) [Astron. Lett. **25**, 269 (1999)]; astro-ph/9904333.
10. W. Kley, Astron. Astrophys. **247**, 95 (1991).
11. W. Kluzniak, *Ph.D. Thesis* (Stanford Univ., 1987).
12. W. Kluzniak and R. V. Wagoner, Astrophys. J. **297**, 548 (1985).
13. H. Lamb, *Hydrodynamics* (Cambridge Univ. Press, Cambridge, 1932; Gostekhizdat, Moscow, 1947).
14. L. D. Landau and E. M. Lifshitz, in *Statistical Physics* (Nauka, Moscow, 1976; Pergamon, Oxford, 1980), Part 1.
15. K. P. Levenfish, Yu. A. Shibanov, and D. G. Yakovlev, Pis'ma Astron. Zh. **25**, 491 (1999) [Astron. Lett. **25**, 417 (1999)].
16. M. C. Miller and F. K. Lamb, Astrophys. J. **470**, 1033 (1996).
17. J. P. Ostriker and J. E. Gunn, Astrophys. J. **157**, 1395 (1969).
18. K. Oswatitsch, *The Foundations of Gas Dynamics* (Springer-Verlag, New York, 1976).
19. R. Popham and R. Narayan, Astrophys. J. **442**, 337 (1995).
20. N. I. Shakura and R. A. Sunyaev, Astron. Astrophys. **24**, 337 (1973).
21. N. R. Sibgatullin and R. A. Sunyaev, Pis'ma Astron. Zh. **24**, 894 (1998) [Astron. Lett. **24**, 774 (1998)].
22. N. R. Sibgatullin and R. A. Sunyaev, Pis'ma Astron. Zh. **26** (2000) (in press) [Astron. Lett. **26** (2000) (in press)].
23. N. Stergioulus, livingreview.org/Articles/Volume 1/1998-8stergio.
24. R. A. Sunyaev and N. N. Shakura, Pis'ma Astron. Zh. **12**, 286 (1986).
25. A. Thampan and B. Datta, Mon. Not. R. Astron. Soc. **297**, 570 (1998).
26. J. L. Tassoul, *Theory of Rotating Stars* (Princeton Univ. Press, Princeton, 1978).

Translated by V. Astakhov

Astronomy Letters, Vol. 26, No. 12, 2000, pp. 779–787. Translated from Pis'ma v Astronomicheskiĭ Zhurnal, Vol. 26, No. 12, 2000, pp. 907–916.
Original Russian Text Copyright © 2000 by Pavlinsky, Grebenev, Mazov, Dekhanov, Ryvkin, Sunyaev, Surtaev, Mokrousov, Glushenko, Yampol'skiĭ, Novikov.

The Spin-X Wide-Field X-ray Monitor of the Spectrum–X–Gamma Astrophysical Observatory

M. N. Pavlinsky[1]*, S. A. Grebenev[1], P. A. Mazov[1], I. A. Dekhanov[1], D. B. Ryvkin[1], R. A. Sunyaev[1], V. I. Surtaev[2], N. V. Mokrousov[2], A. G. Glushenko[2], S. I. Yampol'skiĭ[2], and A. D. Novikov[2]

[1] *Space Research Institute, Russian Academy of Sciences, Profsoyuznaya ul. 84/32, Moscow, 117810 Russia*
[2] *Aalam Special Design Office, Bishkek, Republic of Kyrgyzstan*

Received June 1, 2000

Abstract—The Spin-X wide-field X-ray monitor of the Spectrum–X–Gamma astrophysical observatory, which is based on the principle of a coded-aperture telescope, is designed to detect and localize cosmic gamma-ray-burst (GRB) sources; to survey large areas of the sky in search of new transients; and to carry out long-term observations of bright Galactic sources, including X-ray bursters. The monitor consists of two noncoaxial identical modules, Spin-X1 and Spin-X2, which together cover 6.8% of the sky. The high-apogee, four-day orbit of the Spectrum-XG satellite allows the instrument to be in observing mode more than 50% of the time. Having simulated the rate of GRB detection by Spin-X, we show that extrapolating BATSE 50–300-keV average data on the number of GRBs, their duration, and their mean energy spectrum to the X-ray energy band leads to disagreement with the observed detection rate of GRBs in the X-ray band. The number of GRBs that can be detected and localized with an accuracy $r \leq 3'$ (3σ) (the error-circle radius) by Spin-X is estimated to be ten bursts per year. We present data on the Spin-X sensitivity achievable during long-term observations of persistent and transient sources and on its sensitivity to X-ray bursts from Galactic sources in the 2–30-keV energy band. *© 2000 MAIK "Nauka/Interperiodica".*

Key words: *X-ray monitor, gamma-ray bursts, bursters, Galactic center, coded aperture*

INTRODUCTION

Since the discovery of gamma-ray bursts (GRBs), progress in understanding their origin has always turned on their accurate localization. The initially achieved accuracy of one degree obtained from flux ratios on differently directed detectors [the so-called cosine method implemented in the Konus (Mazets *et al.* 1979) and BATSE (Meegan *et al.* 1992) experiments], as well as the triangulation method based on determination of the arrival direction of a wave front from the delay of its detection on spatially separated spacecraft, has not allowed GRB sources to be identified with any astrophysical objects.

The simultaneous detection and accurate (to within several arcminutes) localization of GRBs by a single instrument hold the greatest promise. Such an accuracy makes possible attempts to identify GRB sources with objects showing up in other energy bands and, primarily, in the optical. GRB detection statistics show that, on the average, one GRB is detected per day by spacecraft near the Earth and that the sky distribution of their sources is uniform. This imposes obvious requirements on the instrument: to have the widest possible field of view (up to 4π) and a localization accuracy of no less than one arcminute at a sufficiently high sensitivity.

Attempts to devise such an instrument have been made repeatedly. In the mid-1980s, it was proposed to divide GRB detection and accurate localization between different instruments on the same spacecraft. This idea was embodied in the Konus–Podsolnukh package of instruments onboard the Granat orbiting observatory (Aptekar' *et al.* 1992). The Konus instrument must have determined the GRB source direction with a 1°–2° accuracy within 1–2 s after GRB detection and must have given target designation for the second Podsolnukh instrument, which included a platform with X-ray counters and an optical monitor. The platform could turn in any direction of the hemisphere with a 20′ accuracy in 1–2 s. Unfortunately, virtually immediately after the Granat spacecraft was placed into orbit in December 1989, problems with telemetry transmission from the Konus and Podsolnukh instruments arose and this original idea produced no serious results, nor did it lead to any discoveries.

A code-aperture technique in the X-ray band came into wide use in the 1980s. A coded aperture allows images with a resolution of the order of one arcminute to be formed within fairly wide fields of view. The XRT (Skinner *et al.* 1987), TTM (Brinkman *et al.* 1985; Zand *et al.* 1989), and ART-P (Sunyaev *et al.* 1990a) X-ray telescopes serve as examples of such instruments. The successful detection and localization of X-ray bursts with a one-arcminute accuracy by the above

---

* E-mail address for contacts: mykle@hea.iki.rssi.ru

instruments (Skinner *et al.* 1987; Sunyaev *et al.* 1990b; Pavlinsky *et al.* 1994) stimulated the use of such telescopes with the widest possible fields of view for detecting and localizing GRBs.

The first results could appear on the TTM telescope of the Kvant/Mir module, because the instrument had a relatively wide field of view (~200 square degrees) covering ~0.5% of the sky. Since 1987, ~3000 20-min-long observing sessions, which is equivalent to ~40 days, have been carried out with TTM over more than ten years of its in-orbit operation. This time, however, proved to be insufficient. The probability of GRB detection was low. The same result was also obtained with the SIGMA gamma-ray telescope (Roques *et al.* 1990) onboard the Granat observatory. There was no GRB within a field of view of ~100 square degrees in a total observing time of ~700 days (Sunyaev *et al.* 1993). This was somewhat unexpected, because it was assumed that the SIGMA telescope would detect one or even two GRBs within its field of view during this period.

It all fell into place with the launch of the BeppoSAX satellite (Perola 1990) in 1996. The WFC wide-field X-ray monitors onboard the BeppoSAX satellite (Jager *et al.* 1993) detected and localized GRB 960720 on July 20, 1996, with a 10′ accuracy (Piro *et al.* 1996). Confirmation that this was actually a GRB rather than an X-ray burst was received from the simultaneous triggering of the GRBM monitor (Frontera *et al.* 1997) onboard the BeppoSAX satellite. A revolutionary result was obtained after GRB 970228 was detected and localized with a 3′ accuracy on February 2, 1997 (Costa *et al.* 1997a). Eight hours later, having modified the satellite observing program, the BeppoSAX narrow-beam telescopes detected an X-ray afterglow of the GRB source (Costa *et al.* 1997b, 1997c). Over a period of three and a half years, from July 1996 until December 1999, the WFC/BeppoSAX instruments detected 25 GRBs. A distinctive feature of the operation of the BeppoSAX low-orbit satellite lay in a routine (every one and a half hours) data transmission to the Earth. This made it possible to rapidly process data and to generate the coordinates of GRB sources for pointing ground-based and orbiting telescopes. Unique data on GRBs, such as GRB 970508 ($z = 0.835$), GRB 971214 ($z = 3.14$), and GRB 980425 ($z = 0.0085$), were obtained with the WFC/BeppoSAX instruments; they showed a cosmological origin at least for some of the GRBs and their possible relationship to supernova explosions. WFC/BeppoSAX data allowed X-ray, optical, and radio afterglows of GRBs to be discovered, which gave strong impetus to the development of theoretical models.

These achievements have stimulated the development and construction of the Spin-X X-ray monitor for the Spektr–Rentgen–Gamma astrophysical orbiting observatory, which is designed to detect and localize GRB sources; to survey large areas of the sky in search of new transients; and to carry out long-term observations of bright Galactic sources, including X-ray bursters.

Below, we describe the Spin-X monitor and present Monte Carlo simulations of the Spin-X functionalities in solving the scientific problems listed in the preceding section.

2. DESCRIPTION OF THE SPIN-X MONITOR

The instrumentation of the Spectrum-XG astrophysical observatory includes two completely identical (but turned relative to one another through an azimuthal angle of 120°) wide-field Spin-X X-ray monitors. The instrument is being developed and constructed at the Space Research Institute (Russian Academy of Sciences) and at the Aalam Special Design Office in Bishkek, the Republic of Kyrgyzstan (the former branch of the Special Design Office of the Space Research Institute). Figure 1 shows a photograph of an engineering mock-up of one such monitor.

The Spin-X monitors are wide-field coded-aperture telescopes simultaneously covering 6.8% of the sky. Their basic parameters are given in Table 1. Only two Spin-X monitors were included in the Spectrum-XG instrumentation because of the mass and energy-consumption limitations.

Detector

A multiwire proportional chamber similar in design to the chamber of the KFRD focal detector (Pavlinsky *et al.* 1998) of the Sodart/Spectrum-XG telescope is used as the Spin-X position-sensitive detector. Figure 2 shows the inside of the Spin-X detector; the wire fields on the leucosapphire frames are clearly seen. The inner size of the wire field is 180 × 180 mm. The chamber has two layers: the first is position-sensitive and spectrometric and the second is only spectrometric. The second layer serves to reject charged particles and operates on anticoincidence with the first layer.

A circuit with an LC-type induction–capacitive delay line on discrete elements is used to determine the photon position in the chamber. The chamber case is made from titanium. A supporting grid is mounted on a beryllium entrance window on the outside to offset the internal gas pressure on this window. The chamber is filled with a gas mixture, 85%Xe + 10%Ar + 5%CO_2, under a 1.3-bar pressure. Four collimated radioactive sources on the periphery of the working detector field, three Fe^{55} and one Cd^{109}, are used for continuous in-flight calibration of the detector energy and position channels.

An energy resolution of 19% at 6 keV and 13% at 22 keV was obtained on the Spin-X detector during preliminary ground-based tests for integrated illumination by external Fe^{55} and Cd^{109} sources. The spatial resolution along the anode wires was found to be 0.6 mm (FWHM) at 6 keV. The resolution across the anode wires pulled at 3-mm steps cannot unequivocally be said to be 0.6 mm, because there is a well-known effect of coordinate modulation by the anode wires. The resolution ranges from 0.4 to 1.5 mm, depending on the distance to the nearest anode.

Optical System

The Spin-X monitor uses a system with incomplete coding, in which the mask size matches the size of the detector entrance window. The minimum size of the mask pixel is constrained by the detector spatial resolution; it must be no less than 1 × 1 mm. The size of the detector entrance window (144.5 × 142.2 mm) predetermined the choice of a pseudorandom sequence of a 127 × 129-pixel mask with a 1.12 × 1.12-mm pixel size. The separation between the mask and the detector entrance window is 413 mm, which provides a nominal angular resolution of $9\overset{\prime}{.}3$ within a $38\overset{\circ}{.}5 \times 38\overset{\circ}{.}0$ (FWZR) field of view. The position accuracy of events on the detector is several times higher than the mask pixel size, allowing sources to be localized with an accuracy higher than the nominal angular resolution.

The Spin-X coded mask is composed of a set of copper plates with a total thickness of 1.0 mm. At the 1.12 × 1.12-mm pixel size, the size of the open field is 1.0 × 1.0 mm. The fraction of open pixels in the mask is 50%. A copper-coated aluminum tube supports the mask and simultaneously serves as a collimator limiting the monitor field of view.

Electronics

The Spin-X electronics accumulates scientific and service information in a 1-Mb buffer memory, supports the communications protocol with the onboard 1553 MIL-STD bus of the Spektr–RG instrumentation, and provides data transmission to the common onboard memory.

The Spin-X monitor has two operating modes: “Burst” and “Flux.” The first is designed to detect GRBs, and the second is designed to survey large areas of the sky in search of new transients and to carry out long-term observations of bright Galactic sources. The instrument processes fluxes up to 10^4 events per second. In the Burst mode, all photons detected by the instrument in a 64-s time interval before the event detection and all photons arrived within 1024 s after the detection are written into the onboard memory. The information stored for a single photon is 5 bytes. In the Flux mode, all detected photons are written into the onboard memory.

3. SIMULATIONS OF SPIN-X OBSERVATIONS

Model

To evaluate the functionalities of the Spin-X wide-field monitor in detecting and localizing GRBs and monitoring persistent Galactic sources, we developed a mathematical model for the instrument that included all basic parameters (see Table 1). Observations were simulated by the Monte Carlo method by taking into account the instrument geometry and the detector effective area and spatial resolution.

Table 1

Operating energy band	2–30 keV
Total field of view (FWZR)	$38\overset{\circ}{.}5 \times 38\overset{\circ}{.}0$
Nominal angular resolution	$9\overset{\prime}{.}3$
Statistical localization accuracy at signal level ≥5σ on restored image	$r \le 3'$ (3σ)
Effective area (corrected for mask shading)	80 cm^2 of 6 keV
Energy resolution (FWHM)	19% of 6 keV
	13% of 22 keV
Time resolution	1/1024 s
Dead time	25 μs
Charged-particle rejection level	≥96%
Detector type	Multiwire proportional chamber
Detector area (=mask size)	144.5 × 142.2 mm
Gas mixture	85%Xe + 10%Ar + 5%CO_2
Gas pressure	1.3 bar
Spatial resolution (FWHM) at 6 keV:	
along anode wires,	0.6 mm
across anode wires	0.4–1.5 mm
Thickness of beryllium entrance window	250 μm
Thickness of detector position-sensitive layer	48 mm
Mask pixel size	1.12 × 1.12 mm
Separation between mask and detector entrance window	413 mm
Mass	40 kg
Energy consumption	30 W

During observations, Spin-X will record three radiation components:

(1) isotropic diffuse X-ray radiation;

(2) fluxes of charged particles left after useful events have been selected by the instrument;

(3) radiation from pointlike compact X-ray sources.

In most cases, diffuse X-ray radiation will make a major contribution to the instrument count rate. Estimates show that a diffuse background described by a power-law spectrum, $8.5 \times E^{-1.4}$ phot. s^{-1} cm^{-2} keV^{-1} ster^{-1} (Zombeck 1982), will give ~37 counts s^{-1} per detector in the 2–30-keV energy band. The charged particles passed through the Spin-X charged-particle rejection system will give ~9 counts s^{-1} (less by a factor of 4); the selection efficiency will be ≥96%. Depending on the monitor pointing, the total count rate from persistent X-ray sources can change by three orders of magnitude. When pointing Spin-X at the Crab Nebula, its contribution to the count rate will be ~182 counts s^{-1}. The

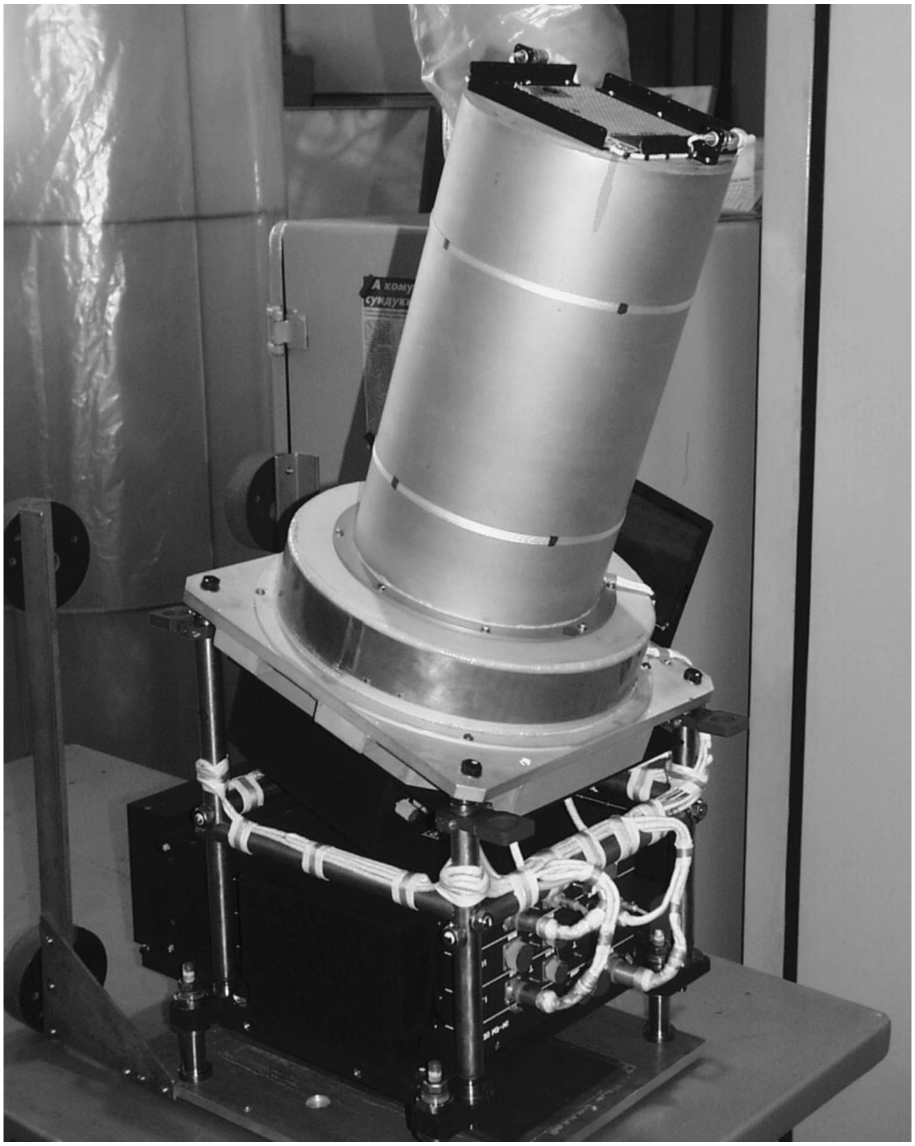

Fig. 1. A photograph of an engineering mock-up of one Spin-X module.

densely populated region of the Galactic center will give ~473 counts s^{-1}. When pointing the monitor at a sparsely populated region of the sky, for example, at the point with $\alpha = 0°$ and $\delta = 0°$, the sources' contribution will be negligible compared to the diffuse background; it will drop to 0.4 counts s^{-1}. Clearly, Spin-X will reach a maximum sensitivity when pointed at sparsely populated regions of the sky.

In our simulations, we used the UHURU Fourth Catalog of X-ray Sources (Forman *et al.* 1978). For simplification, all sources were assumed to have the energy spectrum of optically thin plasma bremsstrahlung with $kT = 5$ keV. We used the Crab flux (947 UHURU units in the 2–10-keV energy band) to recalculate the spectrum normalization from UHURU units. For simplicity, the interstellar absorption column density for all sources was taken to be $N_H = 10^{21}$ cm^{-2}.

We simulated the Spin-X instrument by using the ratio of the mask pixel size to the size of one detector bin $d_M/d_{det} = 4$. In principle, the detector position channels provide a ratio of 8, but using such a large ratio makes sense only for bright transients, where the signal statistical significance is considerably higher. The simple cross-correlation method was used for image restoration. The restored images of sources were fitted by a bivariate Gaussian function, and the error-circle radius was determined.

GRB Detection

The greatest GRB statistics was accumulated by BATSE. The Spin-X operation was simulated for the model that used BATSE data (Petrosian and Lee 1996;

Vikhlinin 1998) on the distribution of $N(>F)$ GRBs with fluences exceeding some threshold level F (in erg cm^{-2}) in the 50–300-keV energy band. For the BATSE data, we used a simple analytic fit

$$N(>F) = \frac{1700}{1 + (F/1.1 \times 10^{-7}\ \mathrm{erg\ cm^{-2}})^{1/2} + (F/1.4 \times 10^{-6}\ \mathrm{erg\ cm^{-2}})^{3/2}}, \quad \text{bursts yr}^{-1}$$

at fluences $F \geq 10^{-7}$ erg cm^{-2}.

As the average GRB photon spectrum integrated over the time profile, we used a spectrum of the form

$$N_E(E) = A\left(\begin{array}{c} \left(\frac{E}{100\ \mathrm{keV}}\right)^{\alpha}\exp\left(-\frac{E}{E_0}\right), \quad (\alpha-\beta)E_0 \geq E \\ \left(\frac{(\alpha-\beta)E_0}{100\ \mathrm{keV}}\right)^{\alpha-\beta}\exp(\beta-\alpha)\left(\frac{E}{100\ \mathrm{keV}}\right)^{\beta}, \quad (\alpha-\beta)E_0 \leq E \end{array}\right), \quad \text{phot s}^{-1}\ \text{cm}^{-2}\ \text{keV}^{-1}$$

with the parameters $\alpha = -1$, $\beta = -2$, and $E_0 = 150$ keV from Band *et al.* (1993). The spectrum is described by optically thin plasma bremsstrahlung with temperature $kT = 150$ keV at soft energies and by a power law with a slope of –2 at high energies.

The mean GRB duration $T_{90} \approx 30$ s with 90% of the fluence was taken from the review by Fishman and Meegan (1995). The sky distribution of GRBs was assumed to be isotropic.

As was already said above, the Spin-X sensitivity depends strongly on how many bright sources fall within the field of view. The observing program and, accordingly, the fields in the sky that will be observed by Spin-X cannot be guessed in advance. Therefore, our simulations of GRB detection with Spin-X were averaged over 100 randomly chosen pointing coordinates α and δ of the instrument principal axis. For such a number of points, the Spin-X field of view covers the sky several times.

With the Spectrum-XG four-day orbit, observations will be performed for three days; the fourth day (to be more precise, ~18 h) is lost, because the satellite passes through the Earth's radiation belts. We plan to carry out continuous observations for approximately 20–21 h; the remaining 3–4 h will be spent on communication sessions with the Earth. Consequently, the largest possible duty cycle of the Spectrum-XG observatory in orbit is 67–68%. Observing experience shows that the above level is very difficult to reach; therefore, when simulating the Spin-X operation, we used a more realistic value of 50%. All our simulations are given for the simultaneous operation of two modules.

Our simulations of GRB detection yielded the following results:

(1) The radius of the Spin-X GRB error circle is $r \leq 3'$ (3σ) at a signal confidence level $\geq 5\sigma$ on the restored image and the ratio $d_{\mathrm{M}}/d_{\mathrm{det}} = 4$;

(2) Figure 3 shows the sky-averaged Spin-X sensitivity to GRBs. The GRB 50–300-keV fluence F (erg cm^{-2}) is along the X axis, and the fraction (in %) of the nominal Spin-X solid angle ($100\% = 2 \times 0.428 = 0.856$ ster) is along the Y axis. The solid line reflects the solid angle within which the instrument is sensitive to GRBs with

Table 2

GRB	F^{a}	r^{b}	T_{γ}^{c}	T_{x}^{d}	IAUC[e]
960720		10	8[f]	17[f]	6467
970111	4	10	43[f]	60[f]	6533
970228	0.23	3	80[f]	55[f]	6572
970402	0.46	12	150[f]	150[f]	6610
970508	1	5	15[f]	29[f]	6649
971214	1	3.9	35[f]	35[f]	6787
971227	1.8	10	10		6796
980109	0.8	10	25		6805
980326	4	8	5		6851
980329	6	3	58[f]	68[f]	6853
980425	3	8	31[f]	40[f]	6884
980515	1.5	4	15		6910
980519	2.5	3	30	190	6910
980613	0.6	4	50	50	6938
981226	0.26	6	20	260	7074
990123	3.4	2	100	100	7095
990217	0.5	3	15		7110
990510	4.3	3	80	80	7160
990627	0.1	3	50	60	7211
990704	6.2	4	40	40	7217
990705	4	3	45	45	7218
990712		2	30	30	7221
990806		3			7235
991014	2.5	6	3	10	7281
991105	1.1	3.6	13	40	7301

[a] Maximum flux in the WFC energy band, in Crabs.
[b] Error box radius (3σ), in arcmin.
[c] Burst duration, in seconds, as determined by GRBM (40–700 keV).
[d] Burst duration, in seconds, as determined by WFC (2–28 keV).
[e] Reference to IAU Circular.
[f] Reference to Frontera *et al.* (2000); blank columns mean lack of data.

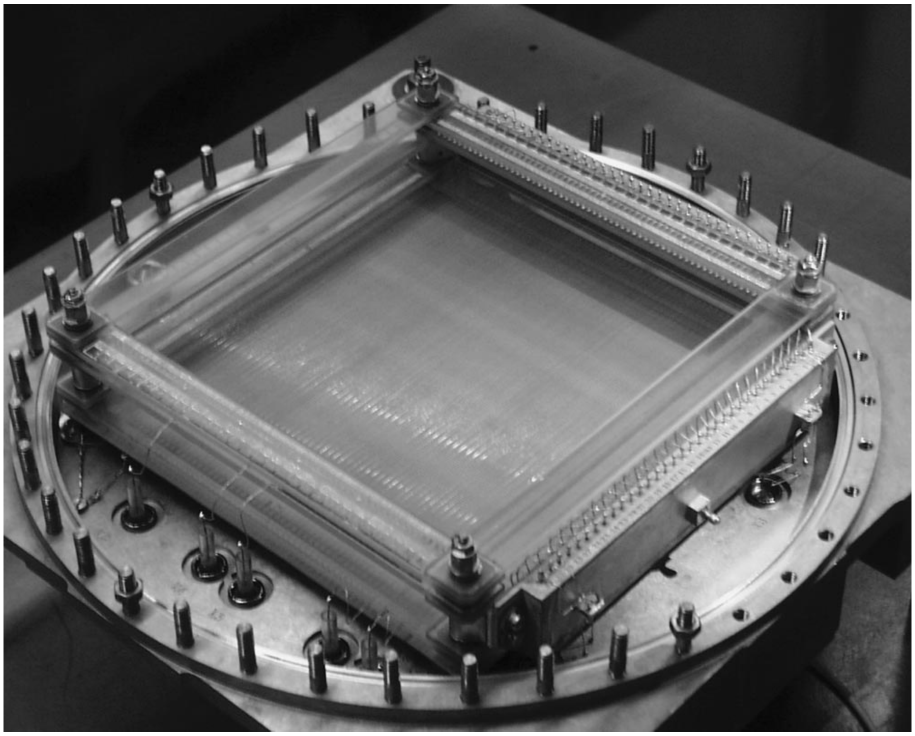

Fig. 2. A photograph of the inside of the Spin-X detector. The wire fields on leucosapphire frames are seen. The inner size of the wire field is 180 × 180 mm.

fluence F at 5σ confidence (by count rate), and the dashed line reflects the solid angle for GRB localization with an accuracy $r \le 3'$ (3σ). We see from Fig. 3 that the instrument has a "sensitive" solid angle that is half the nominal one for GRBs with fluences $F \ge 2.1 \times 10^{-6}$ (5σ by count rate) and 4.9×10^{-6} erg cm^{-2} (by localization), the maximum sensitivity on the principal axis is 1.9×10^{-7} erg cm^{-2};

(3) In the model using BATSE data, 24.4 GRBs with fluences $F \ge 1.9 \times 10^{-7}$ erg cm^{-2} (50–300 keV) fall within the Spin-X nominal solid angle in a year, on the average. Of these, the monitor will detect only 8.9 bursts at a count-rate level $\ge 5\sigma$ and only 4.9 of them are localized with an accuracy $r \le 3'$ (3σ).

The following two points must be noted:

(1) The Spin-X relatively soft energy band starting from 2 keV can be used to determine the interstellar absorption column density.

(2) A nonzero thickness of the detector position-sensitive layer affects the PSF shape at large angles (astigmatism), which results in a reduction of their localization accuracy and, accordingly, in a slightly lower than expected percentage of bursts that can be localized with $r \le 3'$ (3σ) compared to the number of bursts detected by count rate at a level $\ge 5\sigma$.

What can our results imply? The number of GRBs that can be localized by Spin-X and its comparison with WFC/BeppoSAX data are of primary interest. The number of bursts localized by Spin-X in our simulations recalculated to the WFC/BeppoSAX observing time is $4.9 \times 3.3 = 16.17$ bursts (we took 3.3 years, because BeppoSAX carried out no observations from May through August 1997 due to problems with its gyroscopes). The WFC/BeppoSAX effective area at 6 keV is a factor of 1.77 larger than the Spin-X one, which is tantamount to reducing the mean burst duration T_{90} from 30 to 16.9 s when simulating Spin-X. In our simulations with $T_{90} = 16.9$ s, the number of GRBs localized by Spin-X increased only slightly, by a mere 10%, i.e., to 17.8. If we analyze the publicly available WFC/BeppoSAX archival data, then the WFC/BeppoSAX duty cycle recalculated to two monitors, given the time losses associated with the Earth's shading and with data transmission, is ~35%. This is a factor of 1.43 smaller than the duty cycle used to simulate Spin-X. In other words, if the average burst duration and the mean energy spectrum in the 2–30-keV energy band had been the same as those in the 50–300-keV band, then WFC/BeppoSAX would have detected a factor of 2 fewer bursts from July 1996 until December 1999, i.e., a mere ~12.5.

The discrepancy in the results can only be explained by the fact that the BATSE average gamma-ray data on GRB duration and energy spectrum differ from the average X-ray data. Simultaneous BeppoSAX and GINGA X-ray and gamma-ray observations of GRBs serve as a clear example of this.

Average GRB duration. Table 2 gives data on the 25 GRBs detected and localized by the WFC and GRBM instruments of the BeppoSAX satellite from July 1996 to December 1999. If we compare the mean burst durations in the hard and soft energy bands, then we find that $T_\gamma \approx 39.6$ s (for 24 bursts) and $T_X \approx 71.5$ s (for 19 bursts), respectively.

Average energy spectrum. The average data on the 22 GRBs detected by the GINGA instruments show that the ratio of 2–10-keV energy to 50–300-keV energy is $R_{X/\gamma} \approx 0.24$ (Strohmayer *et al.* 1998). The average data on the eight GRBs detected by the BeppoSAX instruments (Frontera *et al.* 2000) show that the ratio of 2–10-keV energy to 40–700-keV energy is $R_{X/\gamma} \approx 0.12$. The ratio $R_{X/\gamma}$ inferred from the average energy spectrum of Band *et al.* (1993) is lower in the former and latter cases, $R_{X/\gamma} \approx 0.085$ and 0.053, respectively.

The observed differences in the average data can account for the discrepancy by a factor of 2 between the number of GRBs detected in the X-ray energy band and their number obtained by our simulations using BATSE data. We thus assume that the estimate in which the results obtained by our simulations with average BATSE data would be multiplied by 2 is correct, i.e., the expected number of GRBs that can be detected and localized with Spin-X is ten bursts per year.

Long-Term Observations of Persistent Sources

Apart from detecting and localizing GRBs, the Spin-X monitor can be used to survey large areas of the sky in search of new transients and to carry out long-term observations of bright Galactic sources. To illustrate the Spin-X potentialities, we simulated observations of the densely populated Galactic-center region. When the monitor is pointed at the Galactic center with $\alpha = 265.62°$ and $\delta = -28.980°$ (epoch 1950), 36 sources from the 4th UHURU Catalog with a total flux of ~7450 UHURU fall within the Spin-X field of view. As was already said above, these sources give a major contribution to the instrument count rate, 473 counts s^{-1}, which accounts for ≥90% of the total count rate. Observations were simulated for an exposure of 10^4 s. Virtually all bright sources were detected on the restored image. For example, two sources, MXB 1735–28 and GX 1+4, with fluxes of 565 and 60 UHURU near the Spin-X principal axis are seen at ~137σ and ~15σ confidence levels, respectively. This implies that the Spin-X sensitivity on the principal axis reaches ~4 UHURU (1σ) in 10^4 s. For comparison, when pointed at the point with $\alpha = 0°$ and $\delta = 0°$, the Spin-X sensitivity increases to ~1 UHURU (1σ).

Figure 4 shows the sky-averaged Spin-X sensitivity (5σ) for an exposure of 10^4 s assuming a power-law energy spectrum for a source with a slope similar to the Crab spectrum, $\propto E^{-2.06}$. The total 2–30-keV energy flux S (erg s^{-1} cm^{-2}) from the source is along the X axis, and the fraction (in %) of the Spin-X nominal solid angle is along the Y axis. The solid line reflects the solid angle within which the instrument sees the source on the restored image at 5σ confidence. The instrument has a "sensitive" solid angle that is half the nominal one for compact sources with energy fluxes $S \geq 3.9 \times 10^{-9}$ erg s^{-1} cm^{-2}, or 108 mCrab.

Detecting X-ray Bursts

We estimated the Spin-X sensitivity to X-ray bursts (from bursters) by assuming a blackbody spectrum of bursts with temperature $kT = 2$ keV and mean duration $\Delta T = 10$ s. For simplicity, the interstellar absorption column density for all compact sources falling within the Spin-X field of view, including the X-ray burster, was taken to be $N_H = 10^{22}$ cm^{-2}.

Figure 4 shows the Spin-X sensitivity to X-ray bursts when the instrument is pointed at the Galactic center with $\alpha = 265.62°$ and $\delta = -28.980°$ (epoch 1950). The dash–dotted line reflects the solid angle within which the instrument is sensitive to bursts with flux S at 5σ confidence (by count rate); the dashed line reflects the solid angle for burst localization with an accuracy $r \leq 3'$ (3σ).

The maximum Spin-X sensitivity to X-ray bursts in the 2–30-keV energy band was estimated from the restored image at 5σ confidence to be 4.4×10^{-9} erg s^{-1} cm^{-2}, which corresponds to a luminosity $L_X \approx 3.8 \times 10^{37}$ erg s^{-1} for the assumed distance of 8.5 kpc to the source. For example, the luminosity averaged over the 19 X-ray bursts detected with ART-P in the fall of 1990 (Pavlinsky *et al.* 1994; Grebenev *et al.* 2001) was found to be $L_X \approx 6.14 \times 10^{37}$ erg s^{-1} in the 4–17-keV energy band, or $L_X \approx 10^{38}$ erg s^{-1} in the 2–30-keV energy band. At this lumi-

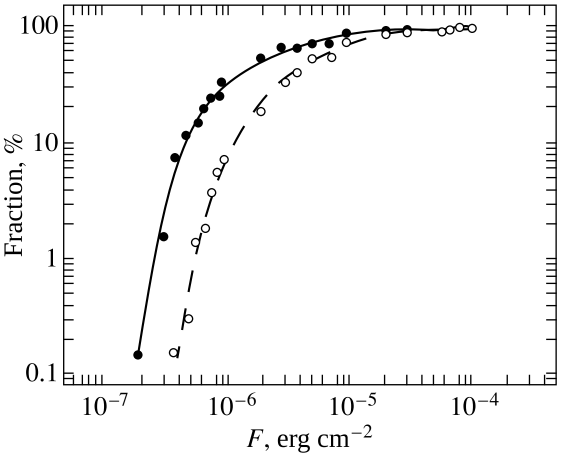

Fig. 3. The Spin-X sensitivity to GRBs. The 50–300-keV burst fluence F (erg cm^{-2}) is along the X axis, and the fraction (in %) of the Spin-X nominal solid angle (100% = 2 × 0.428 = 0.856 ster), which is sensitive to bursts with fluence F at a 5σ level by count rate (solid line) and by localization with an accuracy $r \leq 3'$ (3σ) (dashed line), is along the Y axis.

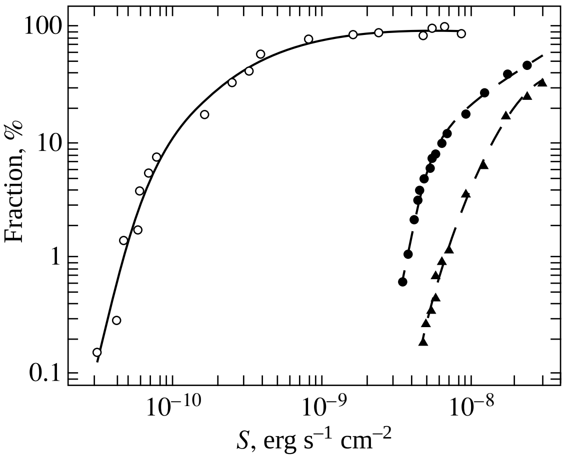

Fig. 4. The sky-averaged Spin-X sensitivity during long-term (10^4 s) observations of persistent sources and during observations of short X-ray bursts ($\Delta T = 10$ s) from the Galactic-center region. The total 2–30-keV energy flux S (erg s^{-1} cm^{-2}) of bursts is along the X axis, and the fraction of the Spin-X nominal solid angle is along the Y axis. The solid line reflects the sensitive solid angle within which the instrument sees a source on the restored image at 5σ confidence, the dash–dotted line (filled circles) reflects the solid angle within which the instrument is sensitive to bursts with flux S at 5σ confidence by count rate, and the dashed line (triangles) reflects the solid angle for burst localization with an accuracy $r \le 3'$ (3σ).

nosity, Spin-X has a sensitive solid angle equal to ~6.4% of the nominal one, which is equivalent to a $9\overset{\circ}{.}6 \times 9\overset{\circ}{.}6$ field.

CONCLUSION

We have described the Spin-X wide-field X-ray monitor of the Spektr–RG astrophysical observatory and provided its basic technical specifications. We simulated the functionalities of the instrument in solving the following problems:

(1) Detecting and localizing GRB sources;

(2) Surveying large areas of the sky in search of new transients and performing long-term observations of bright Galactic sources;

(3) Detecting and localizing X-ray bursts from sources in the Galactic-center region.

Our simulations of the GRB detection rate have shown that extrapolating BATSE 50–300-keV average data on the number of GRBs, their duration, and mean energy spectrum to the X-ray band leads to disagreement with the observed GRB detection rate in the X-ray band. Given the available observational data, the expected number of GRBs detected and localized by Spin-X will reach ~10 bursts per year.

We presented data on the Spin-X average sensitivity for long-term (10^4 s) observations of compact sources and for observations of X-ray bursts from Galactic sources. The instrument has a sensitive solid angle that is half the nominal one for compact sources with energy fluxes $S \ge 3.9 \times 10^{-9}$ erg s^{-1} cm^{-2} (~108 mCrab) and a solid angle equal to 6.4% of the nominal one ($\sim 9\overset{\circ}{.}6 \times 9\overset{\circ}{.}6$) for observations of X-ray bursts with a mean luminosity $L_X \approx 10^{38}$ erg s^{-1} in the 2–30-keV energy band.

ACKNOWLEDGMENTS

We wish to thank the staff of the Aalam Special Design Office in Bishkek (Republic of Kyrgyzstan), who took an active part in designing, constructing, and testing the Spin-X monitor. This study was supported in part by the Russian Foundation for Basic Research (project no. 98-02-17056).

REFERENCES

1. R. L. Aptekar, S. V. Golenetskiĭ, V. N. Ilyinskiĭ, *et al.*, AIP Conf. Proc. **265**, 317 (1991).
2. D. Band, J. Matteson, L. Ford, *et al.*, Astrophys. J. **413**, 281 (1993).
3. A. C. Brinkman, *et al.*, in *Non Thermal and Very High Temperature Phenomena in X-ray Astronomy*, Ed. by G. C. Perola and M. Salvati (Instituto Astronomico, Univerita “La Sapienza”, Roma, 1985), p. 261.
4. E. Costa, M. Feroci, F. Frontera, *et al.*, IAU Circ., No. 6572 (1997a).
5. E. Costa, M. Feroci, L. Piro, *et al.*, IAU Circ., No. 6576 (1997b).
6. E. Costa, F. Frontera, J. Heise, *et al.*, Nature **387**, 783 (1997c).
7. G. J. Fishman and A. C. Meegan, Annu. Rev. Astron. Astrophys. **33**, 415 (1995).
8. W. Forman, C. Jones, L. Cominsky, *et al.*, Astrophys. J., Suppl. Ser. **38**, 357 (1978).
9. F. Frontera, E. Costa, D. Dal Fiume, *et al.*, Astron. Astrophys., Suppl. Ser. **122**, 357 (1997).
10. S. A. Grebenev, A. A. Lutovinov, M. N. Pavlinsky, *et al.*, Pis’ma Astron. Zh. (2001) (in press) [Astron. Lett. (2001) (in press)].
11. R. Jager, J. Heise, J. J. M. In’t Zand, and A. C. Brinkman, Adv. Space Res. **13**, 315 (1993).
12. E. P. Mazets, S. V. Golenetskiĭ, V. N. Il’inskiĭ, *et al.*, Pis’ma Astron. Zh. **5**, 166 (1979) [Sov. Astron. Lett. **5**, 166 (1979)].
13. C. A. Meegan, G. J. Fishman, R. B. Wilson, *et al.*, Nature **355**, 143 (1992).
14. M. N. Pavlinsky, I. Dekhanov, D. Ryvkin, *et al.*, Phys. Scr. **77**, 33 (1998).
15. M. N. Pavlinsky, S. A. Grebenev, and R. A. Sunyaev, Astrophys. J. **425**, 110 (1994).
16. G. C. Perola, Adv. Space Res. **10**, 287 (1990).
17. V. Petrosian and T. T. Lee, Astrophys. J. Lett. **467**, L29 (1996).
18. L. Piro, E. Costa, M. Feroci, *et al.*, IAU Circ., No. 6467 (1996).
19. J. P. Roques, P. Mandrou, J. Paul, and F. Lebrun, Adv. Space Res. **10**, 223 (1990).

20. G. K. Skinner, A. P. Willmore, C. J. Eyles, *et al.*, Nature **330**, 544 (1987).
21. T. Strohmayer, E. Fenimore, T. Murakami, and A. Yoshida, Astrophys. J. **500**, 873 (1998).
22. R. A. Sunyaev, S. I. Babichenko, D. A. Goganov, *et al.*, Adv. Space Res. **10**, 233 (1990a).
23. R. A. Sunyaev, M. R. Gilfanov, E. M. Churazov, *et al.*, Pis'ma Astron. Zh. **16**, 136 (1990b) [Sov. Astron. Lett. **16**, 59 (1990b)].
24. R. Sunyaev, E. Churazov, M. Gilfanov, *et al.*, Astrophys. J. **402**, 579 (1993).
25. A. Vikhlinin, Astrophys. J. Lett. **505**, L123 (1998).
26. J. J. M. In't Zand *et al.*, in *Timing Neutron Stars*, Ed. by H. Ogelman and E. P. J. van den Heuvel (Kluwer, Dordrecht, 1989), p. 317.
27. M. Zombeck, *Handbook of Space Astronomy and Astrophysics* (Cambridge Univ. Press, Cambridge, 1982).

Translated by V. Astakhov

Astronomy Letters, Vol. 26, No. 12, 2000, pp. 788–796. Translated from Pis'ma v Astronomicheskiĭ Zhurnal, Vol. 26, No. 12, 2000, pp. 917–926.
Original Russian Text Copyright © 2000 by Imshennik, Manukovskiĭ.

A Two-Dimensional Hydrostatically Equilibrium Atmosphere of a Neutron Star with Given Differential Rotation

V. S. Imshennik* and K. V. Manukovskiĭ

Institute of Theoretical and Experimental Physics, ul. Bol'shaya Cheremushkinskaya 25, Moscow, 117259 Russia

Received May 16, 2000

Abstract—An analytic solution has been found in the Roche approximation for the axially symmetric structure of a hydrostatically equilibrium atmosphere of a neutron star produced by collapse. A hydrodynamic (quasi-one-dimensional) model for the collapse of a rotating iron core in a massive star gives rise to a heterogeneous rotating protoneutron star with an extended atmosphere composed of matter from the outer part of the iron core with differential rotation (Imshennik and Nadyozhin, 1992). The equation of state of a completely degenerate iron gas with an arbitrary degree of relativity is taken for the atmospheric matter. We construct a family of toroidal model atmospheres with total masses $M \approx 0.1\text{–}0.2M_\odot$ and total angular momenta $J \approx (1\text{–}5.5) \times 10^{49}$ erg s, which are acceptable for the outer part of the collapsed iron core, in accordance with the hydrodynamic model, as a function of constant parameters ω_0 and r_0 of the specified differential rotation law $\Omega = \omega_0 \exp[-(r\sin\theta)^2/r_0^2]$ in spherical coordinates. The assumed rotation law is also qualitatively consistent with the hydrodynamic model for the collapse of an iron core. © *2000 MAIK “Nauka/Interperiodica”.*

Key words: *pulsars, neutron stars and black holes; plasma astrophysics, hydrodynamics, and shock waves*

1. The gravitational collapse of an iron stellar core in the case of its sufficiently rapid initial rotation can produce a binary of neutron stars (NSs) (Imshennik 1992) and surrounding residual gaseous medium that does not become part of the rotating protoneutron star, which is generally unstable to fragmentation (Aksenov *et al.* 1995) and to conversion into a NS binary. The presence of a gaseous medium can result, first, from the heterogeneity of collapse, as revealed by hydrodynamic modeling (Imshennik and Nadyozhin 1992), for the outer part of the collapsing iron core, and, second, from subsequent protoneutron-star fragmentation, as was found in three-dimensional hydrodynamic models (Houser *et al.* 1994; Aksenov 1999); however, the latter models have failed to yield a NS binary and only give the ejection of a gaseous envelope. In any case, the gaseous medium is most likely an iron gas with a completely degenerate electron component, which is in hydrostatic equilibrium in the external gravitational field produced almost entirely by the more massive NS of the putative binary if its mass exceeds appreciably the total mass of the iron gas and the less massive NS. It should be noted that both NSs (particularly the more massive one)—the fragmentation products of the protoneutron star—lie in the immediate vicinity of the center of a vast iron-core cavity. Therefore, a satisfactory approximation for the problem of hydrostatic equilibrium of an iron gas is the Roche approximation with a central source for the gravitational field of the more massive NS with $M_p \approx (1.4\text{–}1.8)M_\odot$, which must be equal to the initial iron-core mass $M_{Fe} \approx 2.0M_\odot$ minus the iron-gas mass $M_e \approx (0.1\text{–}0.2)M_\odot$ and the mass of the low-mass NS $M_{ns} \approx (0.1\text{–}0.4)M_\odot$. In the quasi-one-dimensional approximation with the centrifugal force averaged over angle Θ (in spherical coordinates), this problem was approximately solved by Imshennik and Zabrodina (1999). These authors showed the possibility of hydrostatic equilibrium for a gas mass of $\sim 0.1M_\odot$ if the centrifugal forces (on the average) accounted for 90% of the gravitational forces of attraction with a central mass $M_p = 1.9M_\odot$. The remainder of the repulsive forces are produced by electron gas pressure, with $\rho \propto r^{-3/2}$ and the external radius $r_{ex} \simeq 2.4 \times 10^8$ cm, which is almost half the initial radius $R_{Fe} \simeq 4.4 \times 10^8$ cm of a $2M_\odot$ iron core. In order to estimate the radial sizes of the atmosphere, r_{ex} should be compared with the radius r_{in} of the more massive NS, rather than with the binary orbital radius, if the inequality $M_p \gg M_{ns}$ is satisfied for all times of the binary evolution. Indeed, from the very outset of the binary existence, i.e., since fragmentation, the protoneutron-star separation into two unequal parts seems more likely. One of the arguments for this separation is the detection of an early neutrino signal from SN 1987A, which, unfortunately, was recorded by only one detector (LSD) 4.7 h before the main neutrino signal recorded by three detectors (IMB, KII, BST). If we, nevertheless, associate this early signal with fragmen-

---

* E-mail address for contacts: imshennik@vxitep.itep.ru

tation and the main signal with the collapse of the more massive NS, then, according to our analytic model for the evolution of a NS binary with a total mass of $2M_\odot$ (Imshennik and Popov 1998), the initial mass ratio is $M_{ns}/M_p = 0.195$[1]. During the evolution of the binary orbit, the above ratio, after the low-mass NS fills the Roche lobe, decreases at the end of the evolution to $M_{ns}/M_p = 0.0526$, when $M_{ns} \simeq 0.1M_\odot$ and $M_p \simeq 1.9M_\odot$. Calculations of fragmentation in the above three-dimensional hydrodynamic model with the ejection of a low-mass envelope provide another argument for the separation into two unequal parts. Here, we take the radius of the more massive NS to be $r_{in} \simeq 6 \times 10^6$ cm, bearing in mind that the radius of the Lagrangian layer of a $1.8M_\odot$ protoneutron star was found in the hydrodynamic model of Imshennik and Nadyozhin (1992) to be 3×10^6 cm (see also Imshennik 1995). The increase in the NS radius can be easily understood by taking into account the large contribution of centrifugal forces when the angular momentum is partially conserved during fragmentation. The adopted two-fold increase of this estimate was dictated by convenience of our subsequent computation of the atmospheric structure and is essentially of no importance for our results (see below). Thus, we disregard the mass of the low-mass NS, along with the mass of the atmosphere itself, as sufficiently small and very distant from the coordinate origin with a characteristic orbital radius $r_{orb} \sim 10^8$ cm (Imshennik and Popov 1998).

2. The basic equations for the hydrostatic equilibrium of a two-dimensional configuration with a central pointlike or spherically symmetric gravitating body of given mass M_p and with a given rotation law $\Omega = \Omega(\tilde{\omega})$, where $\tilde{\omega}$ is the cylindrical radius, can be derived from the most general, unsteady-state three-dimensional hydrodynamic system with self-consistent "gravitation," for example, from Aksenov and Imshennik (1994). A given rotation law (with no dependence on the z coordinate) for barotropic equations of state $P = P(\rho)$ is known to be necessary for the conditions of hydrostatic equilibrium to be satisfied (Tassoul 1978).

However, the equations of interest to us in the axisymmetric case can be easily derived. Each Lagrangian particle of matter is subjected to the radially directed gravitational force of the point source, $F_g = -GM_p/r^2$, and to the centrifugal force, $F_r = \vartheta_\varphi^2/\tilde{\omega}$, directed perpendicular to the rotation axis (taken as the z axis), from which the angle θ of the spherical coordinate system is measured. In that case, an external force (per unit mass), which we write in the right-hand part of the relation

$$\frac{1}{\rho}\frac{\partial P}{\partial r} = F_r\cos\left(\frac{\pi}{2}-\theta\right) - \frac{GM_p}{r^2} = \frac{\vartheta_\varphi^2}{r} - \frac{GM_p}{r^2}, \qquad (1)$$

acts in the radial direction and an external force, which is also written on the right,

$$\frac{1}{\rho r}\frac{\partial P}{\partial \theta} = F_r\cos\theta = \frac{\vartheta_\varphi^2}{r\sin\theta}\cos\theta = \frac{\vartheta_\varphi^2}{r}\cot\theta \qquad (2)$$

acts in the meridional direction tangential to a circumference of radius r centered at the coordinate origin.

The counterbalancing external forces of the r- and θ-components of the pressure gradient are written in the left-hand parts of Eqs. (1) and (2). Thus, the system of equations of hydrostatic equilibrium for matter with a barotropic equation of state $P = P(\rho)$ takes explicit form in spherical coordinates if we substitute the relations for the azimuthal rotation velocity $\vartheta_\varphi = (r\sin\theta)\Omega$, where $\Omega = \Omega(r\sin\theta)$ is so far an arbitrary function of the only argument $r\sin\theta$ in Eqs. (1) and (2):

$$\frac{1}{\rho}\frac{\partial P}{\partial r} = r\Omega^2\sin^2\theta - \frac{GM_p}{r^2}, \qquad (3)$$

$$\frac{1}{\rho}\frac{\partial P}{\partial \theta} = r^2\Omega^2\sin\theta\cos\theta. \qquad (4)$$

Clearly, the matter density $\rho = \rho(r, \theta)$ can be determined from this system by additionally specifying the equation of state and boundary conditions. This is done below, but first we formulate some corollaries obtained during a more detailed derivation of the equations from the general system of unsteady-state, three-dimensional hydrodynamic equations in Aksenov and Imshennik (1994). This derivation is contained in Manukovskiĭ (1999). The main corollary is as follows: in the Roche approximation, the system of equations (3) and (4) is unique for a hydrostatically equilibrium ($\partial/\partial t = 0$), axially symmetric ($\partial/\partial\varphi = 0$) atmosphere composed of matter with a barotropic equation of state $P = P(\rho)$. In this case, it is, of course, implied that the specific internal energy E is given by the thermodynamic relation $P = \rho^2 dE/d\rho$. Other corollaries are formulated as follows: (i) we first exclude a singular rotation law, $\Omega \propto \tilde{\omega}^{-2}$, at nonzero velocity components, $\vartheta_r \neq 0$ and $\vartheta_\theta \neq 0$, and (ii) then rule out the possibility of nonzero velocities; i.e., we assume that $\vartheta_r = \vartheta_\theta \equiv 0$. The latter corollary follows from such an unacceptable property of these velocity components in the steady-state, axisymmetric case: their resultant at any point in space is directed along the rotation axis, because the identity $\vartheta_r\sin\theta + \vartheta_\theta\cos\theta = 0$ holds. This all implies that the well known meridional matter circulations, which, in contrast to the above ones, have closed trajectories and require no external sources of matter (Mestel 1970), are not possible.

Below, we use the equation of state of a completely degenerate electron gas with an arbitrary degree of rel-

---

[1] The estimate is given for a circular orbit (with a zero eccentricity). For elliptic orbits, this ratio slightly increases, but this increase is generally modest as long as $e_0 \leq 0.8$ (Imshennik and Popov 1994).

ativity, i.e., we imply a nonzero entropy of matter composed of ^{56}Fe, so the electron density is

$$n_e = \frac{26}{56}\frac{\rho}{m_u}. \tag{5}$$

In this case, we have for the pressure P and the specific internal energy E (see Landau and Lifshitz 1951)

$$P = C\left[\xi_F\left(\frac{2}{3}\xi_F^2 - 1\right)\sqrt{\xi_F^2 + 1} + \operatorname{Arsh}\xi_F\right], \tag{6}$$

$$E = \frac{C}{\rho}[\xi_F(2\xi_F^2 + 1)\sqrt{\xi_F^2 + 1} - \operatorname{Arsh}\xi_F], \tag{7}$$

where the dimensionless Fermi momentum (in units of $m_e c$) is

$$\xi_F = B\rho^{1/3} \tag{8}$$

and the constants B and C have the following known values:

$$B = \frac{2\pi\hbar}{m_e c}\left(\frac{39}{224\pi m_u}\right)^{1/3} = 7.792\times10^{-3}\ \mathrm{cm/g}^{1/3},$$

$$C = \pi m_e c^2\left(\frac{m_e c}{2\pi\hbar}\right)^3 = 1.801\times10^{23}\ \mathrm{g(s^2\ cm)^{-1}}.$$

It is easy to verify that the functions (6) and (7), as should be the case, satisfy the thermodynamic relation

$$P = \rho^2\frac{dE}{d\rho},$$

because the specific entropy of matter with the equations of state (6) and (7) is zero. However, our subsequent calculations are seriously simplified if a simple representation of the derivatives of pressure in Eqs. (3) and (4) with (8) is used,

$$\frac{\partial P}{\partial \eta} = M\rho\frac{\partial\phi}{\partial\eta}, \quad \phi = \sqrt{1 + \xi_F^2} = \sqrt{1 + B^2\rho^{2/3}}, \tag{9}$$

and if the constant M is expressed in terms of B and C,

$$M = \frac{8}{3}CB^3 = 2.272\times10^{17}\ \mathrm{cm^2\ s^{-2}}.$$

We take the following simple analytic formula as the differential rotation law:

$$\Omega = \omega_0\exp\left(-\frac{r^2\sin^2\theta}{r_0^2}\right), \tag{10}$$

which is in satisfactory agreement with the collapse calculations by Imshennik and Nadyozhin (1992) if we substitute appropriate values for the arbitrary constant parameters ω_0 and r_0 in it. Note that we may use any other plausible rotation law, for example, a law for which the rotation frequency decreases with increasing cylindrical radius as $1/\tilde{\omega}^k$. However, because of the stringent constraint on the mass, virtually the same toroidal solutions with slightly different profiles are obtained in all cases.

Using formula (9), let us write Eqs. (3) and (4) in final form, which we will solve to determine the structure of a hydrostatically equilibrium iron atmosphere in the form of $\rho = \rho(r, \theta)$ for the rotation law (10):

$$M\frac{\partial\phi}{\partial r} = r\omega_0^2\exp\left(-\frac{2r^2\sin^2\theta}{r_0^2}\right)\sin^2\theta - \frac{GM_p}{r^2}, \tag{11}$$

$$M\frac{\partial\phi}{\partial\theta} = r^2\omega_0^2\exp\left(-\frac{2r^2\sin^2\theta}{r_0^2}\right)\sin\theta\cos\theta, \tag{12}$$

where ϕ is defined in (9).

3. The system of equations (11) and (12) can be easily solved. Let us first integrate (11):

$$M\phi = -\frac{\omega_0^2 r_0^2}{4}\exp\left(-\frac{2r^2\sin^2\theta}{r_0^2}\right) + \frac{GM_p}{r} + F(\theta), \tag{13}$$

where $F(\theta)$ is an arbitrary function of θ. In order to determine $F(\theta)$, we differentiate (13) with respect to θ and substitute the result in (12):

$$F'(\theta) = 0, \quad F(\theta) = F_0 = \mathrm{const}. \tag{14}$$

Thus, the sought-for solution is

$$M\phi = -\frac{\omega_0^2 r_0^2}{4}\exp\left(-\frac{2r^2\sin^2\theta}{r_0^2}\right) + \frac{GM_p}{r} + F_0; \tag{15}$$

hence, we can easily find $\rho = \rho(r, \theta)$ by using the definition of ϕ from (9):

$$\rho = \rho(r,\theta) = \frac{1}{B^3}\left\{\frac{1}{M^2}\left[\frac{GM_p}{r} - \frac{\omega_0^2 r_0^2}{4}\exp\left(-\frac{2r^2\sin^2\theta}{r_0^2}\right) + F_0\right]^2 - 1\right\}^{3/2}. \tag{16}$$

Equation (16) contains an arbitrary integration constant of the system (11) and (12), which is yet to be determined from the boundary conditions. It is important to note that the system (11) and (12) has a solution only if we take $f(\theta) = \sin\theta$ in $\Omega = \Omega(rf(\theta))$; no solution exists for any other function $f(\theta)$, as would be expected (Tassoul 1978). In this case, the form of dependence on the argument $r\sin\theta$ is unimportant. We chose it in the form (10).

Next, we consider the boundary conditions to determine the constant F_0. Let the external radius of the atmosphere at which the density takes on a constant value ρ_0 be equal to r_{ex}. Note that it would be more natural to specify the boundary condition at the equator of the atmosphere, i.e., at $\theta_0 = \pi/2$, though relation (16) formally requires such a boundary condition only at some unique angle θ_0. After simple transformations, we derive the final expression for the density distribution of an iron atmosphere by eliminating the integration constant F_0 from (16) using the above boundary condition:

$$\rho = \frac{1}{B^3}\left\{\left[\sqrt{1+B^2\rho_0^{2/3}} + \frac{GM_\mathrm{p}}{M}\left(\frac{1}{r}-\frac{1}{r_\mathrm{ex}}\right) + \frac{\omega_0^2 r_0^2}{4M}\left(\exp\left(-\frac{2r_\mathrm{ex}^2}{r_0^2}\right) - \exp\left(-\frac{2r^2\sin^2\theta}{r_0^2}\right)\right)\right]^2 - 1\right\}^{3/2}. \tag{17}$$

As can be verified, only the factor $\sin^2\theta_0$ appears in the first exponential term in (17) at other angles $\theta_0 \neq \pi/2$. However, choosing the boundary condition not at the equator for constant r_ex (particularly at small θ_0) generally causes the total atmospheric mass to increase considerably, which seems unnatural.

4. Let us write some integrated quantities that are of interest in physically interpreting the solution (17) with allowance for a mirror symmetry. The total atmospheric mass M_0 for the given density distribution $\rho(r, \theta)$ (17) is

$$M_0 = 2\times 2\pi\int_{r_\mathrm{in}}^{r_\mathrm{ex}} r^2 dr\int_0^{\pi/2}\rho(r,\theta)\sin\theta d\theta. \tag{18}$$

The total angular momentum J_0 of the atmosphere is

$$J_0 = 2\times 2\pi\int_{r_\mathrm{in}}^{r_\mathrm{ex}} r^4 dr\int_0^{\pi/2}\rho(r,\theta)\Omega(r\sin\theta)\sin^3\theta d\theta. \tag{19}$$

The gravitational (E_gr), internal (E_in) [using (7) for $E(\rho)$], and rotational (E_rot) energies are, respectively,

$$E_\mathrm{gr} = -2\times 2\pi\int_{r_\mathrm{in}}^{r_\mathrm{ex}}\left(\frac{GM_\mathrm{p}}{r}\right) r^2 dr\int_0^{\pi/2}\rho(r,\theta)\sin\theta d\theta, \tag{20}$$

$$E_\mathrm{in} = 2\times 2\pi\int_{r_\mathrm{in}}^{r_\mathrm{ex}} r^2 dr\int_0^{\pi/2}\rho(r,\theta)E(\rho)\sin\theta d\theta, \tag{21}$$

$$E_\mathrm{rot} = 2\times 2\pi\int_{r_\mathrm{in}}^{r_\mathrm{ex}} r^4 dr \times\int_0^{\pi/2}\rho(r,\theta)\left(\frac{1}{2}\Omega^2(r\sin\theta)\right)\sin^3\theta d\theta. \tag{22}$$

All integrals (18)–(22) are written in this case of symmetry about the $z = 0$ equatorial plane; they imply the presence of a matter-free spatial region for which the expression in curly braces in (17) becomes a negative quantity without any physical meaning. Note that the equilibrium equations (11) and (12) formally admit of an imaginary solution ρ, though the function ϕ [see relation (9)] in Eqs. (11) and (12) is, of course, always positive. Therefore, the domain of the solution of interest to us is bounded by the line of zero density $\rho = 0$ (17):

$$f(r_\mathrm{in}^*, \theta) = \sqrt{1+B^2\rho_0^{2/3}} + \frac{GM_\mathrm{p}}{M}\left(\frac{1}{r_\mathrm{in}^*}-\frac{1}{r_\mathrm{ex}}\right) + \frac{\omega_0^2 r_0^2}{4M}\left[\exp\left(-\frac{2r_\mathrm{ex}^2}{r_0^2}\right) - \exp\left(-\frac{2r_\mathrm{in}^{*2}\sin^2\theta}{r_0^2}\right)\right] - 1 = 0. \tag{23}$$

As our numerical solution of the transcendental equation (23) shows, the angle θ at small values of the product $r_0\omega_0$($\leq 1.08 \times 10^{11}$ cm s^{-1}) varies in the range from $\theta = \theta_\mathrm{max} = \pi/2$ to $\theta = \theta_\mathrm{ex} < \pi/2$ while passing through a minimum $\theta = \theta_\mathrm{min} < \theta_\mathrm{ex}$. At large values of $r_0\omega_0$, the angle θ monotonically decreases from $\pi/2$ to θ_ex. In all cases, the radius r_in^* monotonically increases from its minimum $r_\mathrm{inmin}^* \equiv r_\mathrm{min}^*$ to maximum $r_\mathrm{inmax}^* \equiv r_\mathrm{ex}$. This is how the inner surface of the toroidal volume of an iron atmosphere is obtained, whereas its outer surface coincides with the external sphere of radius $r = r_\mathrm{ex}$, and the angle clearly increases from $\theta = \theta_\mathrm{ex}$ to $\theta = \pi/2$. In this case, $\rho = \rho_0$ at the equator by our definition of the constant F_0 described above when passing from (16) to (17); $\rho = 0$ at $\theta = \theta_\mathrm{ex}$, and, using (23), we explicitly derive at $r_\mathrm{in}^* = r_\mathrm{ex}$

$$\exp\left(-\frac{2r_\mathrm{ex}^2\sin^2\theta_\mathrm{ex}}{r_0^2}\right) = \frac{4M}{\omega_0^2 r_0^2}\sqrt{1+B^2\rho^{2/3}} + \exp\left(-\frac{2r_\mathrm{ex}^2}{r_0^2}\right) - \frac{4M}{\omega_0^2 r_0^2}. \tag{24}$$

Here, we are primarily interested in low-mass atmospheres with $M_0 \simeq 0.1M_\odot$. As our calculations show, they are toroidal structures with $r_\mathrm{ex} > r_\mathrm{min}^* > r_0 \gg r_\mathrm{in}$ and $\theta_\mathrm{min} \approx \theta_\mathrm{ex} \sim \pi/4$. Therefore, r_in, which is such an uncertain quantity for a NS binary with a total mass $M_\mathrm{p} + M_\mathrm{ns} = M_\mathrm{Fe} - M_\mathrm{e}$, is of no practical importance.

5. Next, it is instructive to show how the solution changes when we pass from the general equation of state (6) to a polytropic one; i.e., when the dependence $P = P(\rho)$ takes the form

$$P = K\rho^\gamma, \tag{25}$$

where the coefficient K can be formally represented as $K = P_0/\rho_0^\gamma$. This passage affects only the form of the dependence $\phi = \phi(\rho)$. When the equation of state (6) is

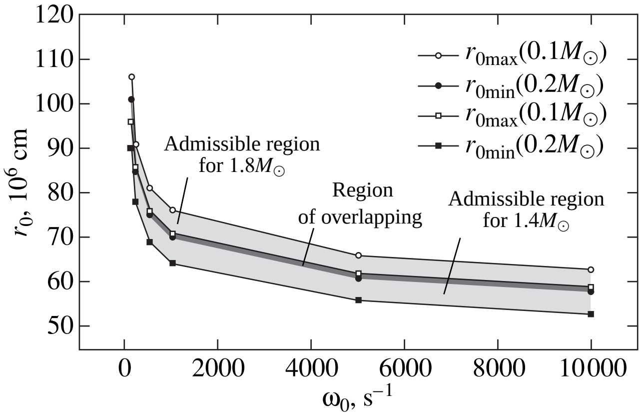

Fig. 1. Admissible (by the atmospheric mass) regions in the r_0–ω_0 plane for central masses $M_p = 1.8$ and $1.4M_\odot$.

replaced by expression (25), the function ϕ, according to (9), takes the form

$$M\phi = \frac{K\gamma}{\gamma-1}\rho^{\gamma-1}. \quad (26)$$

Thus, since the entire line of reasoning when deriving $\phi = \phi(r, \theta)$ from the solution of Eqs. (11) and (12) does not depend on the form of the equation of state and is valid as before, we can immediately write the expression for the density distribution of an iron atmosphere in the polytropic approximation:

$$\rho = \rho(r,\theta) = \left[\rho_0^{\gamma-1} + \frac{GM_p}{A(\gamma)}\left(\frac{1}{r} - \frac{1}{r_{ex}}\right) + \frac{\omega_0^2 r_0^2}{4A(\gamma)}\left(\exp\left(-\frac{2r_{ex}^2}{r_0^2}\right) - \exp\left(-\frac{2r^2\sin^2\theta}{r_0^2}\right)\right)\right]^{\frac{1}{\gamma-1}}, \quad (27)$$

where $A(\gamma) = K\gamma/\gamma - 1$. Below, we also give explicit expressions for the density functions $\rho(r, \theta)$ from (27) in two limiting cases for the equation of state (6):

$$\xi_F \ll 1:\ \gamma = \frac{5}{3},$$

$$K_{5/3} = \frac{8}{15}CB^5 = 2.758\times10^{12}\ \mathrm{cm}^4\ \mathrm{s}^{-2}\ \mathrm{g}^{-2/3},$$

$$\rho = \left[\rho_0^{2/3} + \frac{2GM_p}{5K_{5/3}}\left(\frac{1}{r} - \frac{1}{r_{ex}}\right) + \frac{\omega_0^2 r_0^2}{10K_{5/3}}\left(\exp\left(-\frac{2r_{ex}^2}{r_0^2}\right) - \exp\left(-\frac{2r^2\sin^2\theta}{r_0^2}\right)\right)\right]^{\frac{3}{2}}, \quad (28)$$

$$\xi_F \gg 1:\ \gamma = \frac{4}{3},$$

$$K_{4/3} = \frac{2}{3}CB^4 = 4.424\times10^{14}\ \mathrm{cm}^3\ \mathrm{s}^{-2}\ \mathrm{g}^{-1/3},$$

$$\rho = \left[\rho_0^{1/3} + \frac{GM_p}{4K_{4/3}}\left(\frac{1}{r} - \frac{1}{r_{ex}}\right) + \frac{\omega_0^2 r_0^2}{16K_{4/3}}\left(\exp\left(-\frac{2r_{ex}^2}{r_0^2}\right) - \exp\left(-\frac{2r^2\sin^2\theta}{r_0^2}\right)\right)\right]^3, \quad (29)$$

where B and C are the known constants. Note that, for a given rotation law, replacing the general equation of state by a polytropic one, as our calculations show, causes no appreciable change in the shape of the atmospheric surface, but causes a substantial density redistribution inside the atmosphere and a considerable reduction in mass (particularly for $\gamma = 5/3$).

6. We now turn to the results of our numerical calculations of density distributions $\rho(r, \theta)$ [relation (17)] and of the corresponding integrated quantities (18)–(22). In order for the validity conditions of the Roche approximation and the conditions of gravitational collapse with a residual iron gas mass M_e (see above) of interest to us to be satisfied, we restrict the total mass of an equilibrium atmosphere M_0 (18) to the range (0.1–0.2)$M_\odot$. We take the external radius to be $r_{ex} = 2.38 \times 10^8$ cm and the limiting equatorial density to be $\rho_0 = 5.66 \times 10^5$ g cm^{-3} (Imshennik and Zabrodina 1999). Consider two masses of the central NS: $M_p = 1.8M_\odot$ and $1.4M_\odot$ (see above). Our numerical calculations indicate that a fairly narrow admissible (by the total mass M_0 of an iron atmosphere) region in the $r_0 - \omega_0$ plane is obtained for a fixed mass of the central NS. Figure 1 shows two such regions for the two M_p, which slightly overlap with one another. We see from Fig. 1 that, as the central mass decreases, the admissible region displaces to the coordinate origin in the $r_0 - \omega_0$ plane, i.e., toward atmospheres with slower rotation (with a smaller product $r_0\omega_0$), as should be the case. The table gives the rotation parameters of these regions; quite naturally, $r_{0\max}$ and $r_{0\min}$ for a given ω_0 correspond to the minimum and maximum admissible atmospheric masses $M_0 = 0.1$ and $0.2M_\odot$, respectively (see also Fig. 1). Clearly, for any given M_p, more massive atmospheres with $M_0 > 0.2M_\odot$ and less massive atmospheres with $M_0 < 0.1M_\odot$ lie, respectively, below and above the highlighted regions in Fig. 1. The table also lists values for all forms of energy (20)–(22), as well as the total energy $E_{tot} = E_{gr} + E_{in} + E_{rot}$ and total angular momentum J_0 (19). All these quantities refer to both boundaries of the regions inside which they continuously change from one limiting value to the other. We see from the table that all $E_{tot} < 0$, with $|E_{tot}| \sim 10^{50}$ erg, for all ω_0 except the slowest rotation $\omega_0 = 100$ s^{-1}. In this case, $|E_{tot}|$ sharply

Table

$M = 1.8M_0$, $r_{ex} = 2.38 \times 10^8$ cm							
ω_0, s^{-1}		100	200	500	1000	5000	10000
$r_{0\,max}$, 10^6 cm		106	91	81	76	66	63
$r_{0\,min}$, 10^6 cm		101	85	75	70	61	58
$J_{\text{tot max}r_0}$	, 10^{49} cm^2 s^{-1} g	2.07	3.18	3.09	2.8	2.67	2.54
$J_{\text{tot min}r_0}$		3.41	5.27	5.17	4.79	4.3	4.15
$E_{\text{gr max}r_0}$	, 10^{50} erg	–28.9	–2.73	–2.79	–2.54	–2.62	–2.55
$E_{\text{gr min}r_0}$		–69.7	–5.38	–5.64	–5.35	–5.17	–5.14
$E_{\text{rot max}r_0}$	, 10^{50} erg	0.78	1.11	1.12	1.02	1.05	1.02
$E_{\text{rot min}r_0}$		1.49	2.08	2.16	2.04	1.96	1.95
$E_{\text{in max}r_0}$	, 10^{50} erg	5.10	0.84	0.87	0.80	0.84	0.82
$E_{\text{in min}r_0}$		15.0	1.79	1.89	1.80	1.77	1.77
$E_{\text{tot max}r_0}$	, 10^{50} erg	–23.1	–0.79	–0.80	–0.72	–0.74	–0.72
$E_{\text{tot min}r_0}$		–53.2	–1.54	–1.59	–1.50	–1.44	–1.43
$M = 1.4M_0$, $r_{ex} = 2.38 \times 10^8$ cm							
ω_0, s^{-1}		100	200	500	100	5000	10000
$r_{0\,max}$, 10^6 cm		96	86	76	71	62	59
$r_{0\,min}$, 10^6 cm		90	78	69	64	56	53
$J_{\text{tot max}r_0}$	, 10^{49} cm^2 s^{-1} g	2.47	2.44	2.45	2.29	2.08	2.01
$J_{\text{tot min}r_0}$		3.76	4.18	3.94	3.75	3.27	3.19
$E_{\text{gr max}r_0}$	, 10^{50} erg	–7.65	–2.08	–2.25	–2.16	–2.12	–2.11
$E_{\text{gr min}r_0}$		–25.0	–4.55	–4.60	–4.57	–4.29	–4.39
$E_{\text{rot max}r_0}$	, 10^{50} erg	0.68	0.81	0.86	0.83	0.81	0.81
$E_{\text{rot min}r_0}$		1.49	1.66	1.66	1.64	1.54	1.56
$E_{\text{in max}r_0}$	, 10^{50} erg	1.56	0.77	0.85	0.83	0.82	0.82
$E_{\text{in min}r_0}$		5.76	1.79	1.85	1.85	1.76	1.81
$E_{\text{tot max}r_0}$	, 10^{50} erg	–5.30	–0.50	–0.53	–0.51	–0.49	–0.49
$E_{\text{tot min}r_0}$		–17.8	–1.09	–1.09	–1.08	–1.0	–1.02

increases (by several tens of times). Clearly, this is of no interest from the viewpoint of the model for asymmetric explosions of collapsing supernovae (Aksenov *et al.* 1997), because the atmospheres closely approach the central star, up to the contact ($r^*_{min} = r_{in}$), and become gravitationally bound in explosion ($|E_{gr}| \sim 10^{52}$ erg). At the same time, for all other values of $\omega_0 \geq 200$ s^{-1}, the energy parameters of the atmospheres are acceptable in the above ratio: the contributions of E_{in} and E_{rot} turn out to be similar, ~10^{50} erg, while $|E_{gr}| \sim 3 \times 10^{50}$ erg. Note also that the table gives the corresponding values of total angular momentum J_0, $(2–4) \times 10^{49}$ erg s; they vary in a relatively narrow range consistent with the calculations of Imshennik and Nadyozhin (1992). Figures 2–4 show isochores in the θ–r plane of spatial variables, which demonstrate the configuration of a toroidal atmosphere for its density distribution $\rho(r, \theta)$ for the general equation of state at three different points of the admissible region for the central mass $M_p = 1.8M_\odot$. The

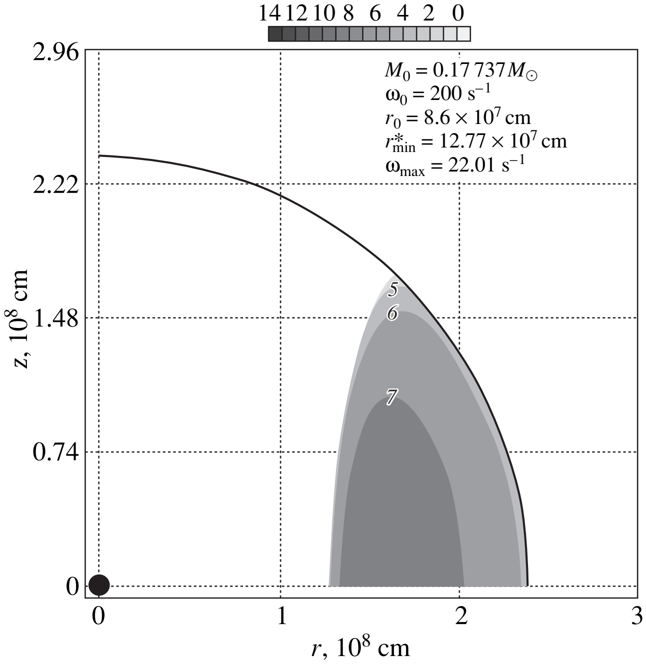

Fig. 2. Isochores in the θ–r plane of spatial variables showing the atmospheric density distribution $\rho(r, \theta)$ for the general equation of state with a central mass $M_p = 1.8M_\odot$ and for rotation parameters $r_0 = 86 \times 10^6$ cm and $\omega_0 = 200$ s^{-1}.

figures also show minimum radii r^*_{min} for the inner boundary of the toroidal volume of an iron atmosphere and maximum rotation frequencies ω_{max} of the atmospheric matter. This is clearly reached just near the inner boundary with radius r^*_{min} [see (10)]. These data lead us to conclude that, at all points within the admissible (by the atmospheric mass) region shown in Fig. 1, we obtain toroidal solutions with a characteristic highly elongated (along the z axis) profile differing only slightly from each other. The characteristic features shared by all solutions are a maximum matter density in the atmosphere (10^7–10^8 g cm^{-3}) and an abrupt drop in density at the inner boundary. When the mass of the central NS is $M_p = 1.4M_\odot$, we obtain almost the same results as would be expected. For comparison, Figs. 5 and 6 show the profiles of atmospheres with the same rotation law as in Fig. 3, but for a polytropic equation of state. Figures 5 and 6 correspond to atmospheres with nonrelativistic (polytropic index $\gamma = 5/3$) and relativistic ($\gamma = 4/3$) equations of state, respectively. Both cases are characterized by an appreciable reduction in total atmospheric mass compared to the general equation of state through a slight change in the internal structure of the atmosphere, with the shape of the outer boundary being virtually unchanged. This effect turns out to be particularly strong for atmospheres with the polytropic index $\gamma = 5/3$.

7. Let us discuss our results for toroidal iron atmospheres with rotation in the vicinity of a central star located near the coordinate origin with the mass of the more massive NS from the putative NS binary. Of fundamental importance is the very existence of steady-state solutions for such atmospheres with acceptable sets of parameters for an asymmetric explosion with a typical supernova energy to take place. The above statement of the problem, which assumes a zero matter tem-

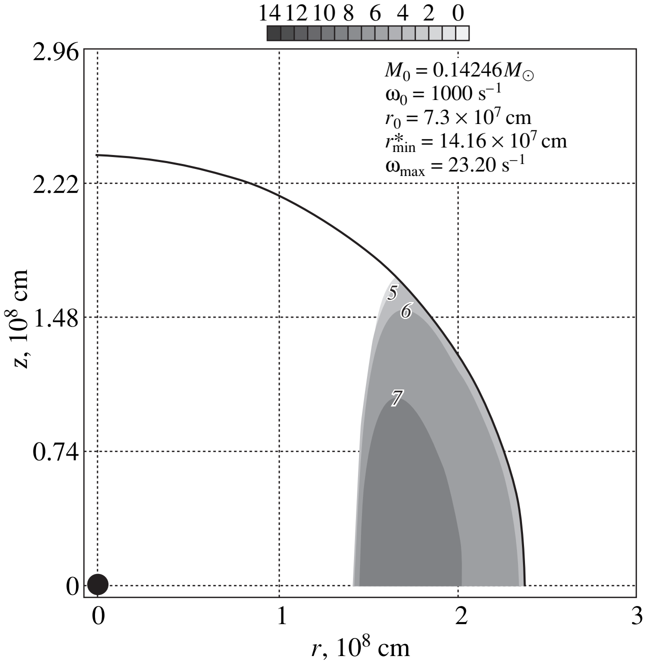

Fig. 3. Same as Fig. 2 for $r_0 = 73 \times 10^6$ cm and $\omega_0 = 1000$ s^{-1}.

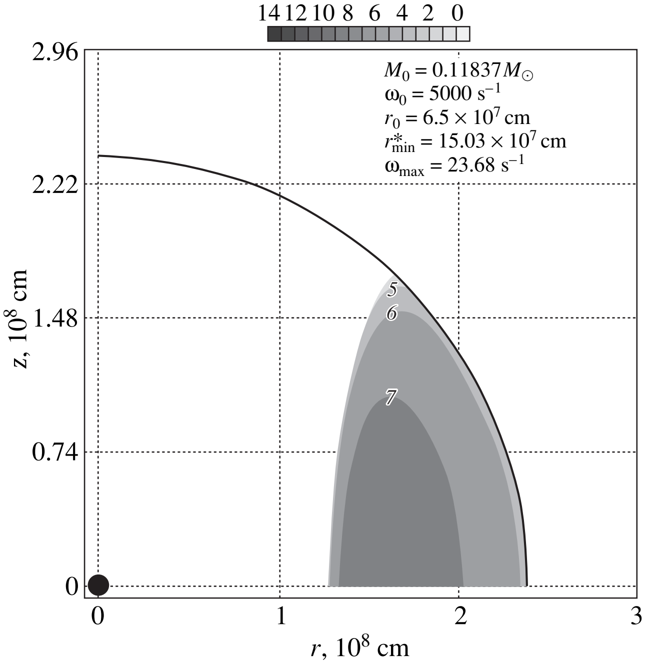

Fig. 4. Same as Fig. 2 for $r_0 = 65 \times 10^6$ cm and $\omega_0 = 5000$ s^{-1}.

perature, lifts any upper bounds on the lifetimes of these atmospheres. At the same time, it is clear that the assumption of a zero temperature requires higher rotation parameters ω_0 and r_0 than those in the general case of nonzero temperatures. It is instructive to roughly estimate the time scale of cooling through neutrino energy losses for the matter of an iron atmosphere with density $\rho \simeq 10^6$ g cm^{-3}. Assuming a kinetic equilibrium for beta processes with volume emission of pairs of electron neutrinos (ν_e and $\tilde{\nu}_e$), we may take (Imshennik *et al.* 1967) $q_{\nu,\tilde{\nu}}^{(n,p)} \simeq 10^{18}$ erg cm^{-3} s^{-1} for the power of energy losses in matter composed of free nucleons at temperature $T = 2\times10^9$ K (see Fig. 1 in the above paper). In our case of matter composed of completely ionized iron, this estimate, roughly speaking, must be reduced by a factor of $A_{\rm Fe}(ft)_{\rm Fe}/(ft)_{n,p}$, where $A_{\rm Fe} = 56$, $(ft)_{\rm Fe} \simeq 10^5$ and $(ft)_{n,p} \simeq 10^3$; i.e., $q_{\nu,\tilde{\nu}}^{(\rm Fe)} \simeq 2\times10^{15}$ erg cm^{-3} s^{-1}. If we write the cooling time scale as $\tau_q \simeq e_{\rm in}/q_{\nu,\tilde{\nu}}^{(\rm Fe)}$, where the internal energy density is

$$e_{\rm in} = \frac{3}{2}k_{\rm B}T\frac{(Z_{\rm Fe}+1)\rho}{A_{\rm Fe}m_0} \simeq 1.2\times10^{23}\,\frac{\rm erg}{\rm cm^3},$$

we then obtain the final estimate $\tau_q \simeq 6\times10^7$ s $\simeq 2$ years. This estimate essentially corresponds to the conditions of a nondegenerate iron gas and neglect of all energy thresholds for beta processes; i.e., at least $k_{\rm B}T \sim m_ec^2 \sim E_0 \sim 1$ MeV and $T \geq T_{\rm d} \simeq 2\times10^9$ K (E_0 is the characteristic threshold energy of electron beta capture in iron, and $T_{\rm d}$ is the degeneracy temperature). Our rough estimate of τ_q implies that, over the lifetimes of the NS binaries (~1 h) of interest to us, no significant matter cooling in their atmospheres takes place. Therefore, the atmospheric structures found in our analytic solution slightly overestimate the rotation parameters ω_0 and r_0 required for hydrostatic equilibrium. Finally, note that the above temperature $T \simeq 2\times10^9$ K just corresponds to the results of our collapse calculations (Imshennik and Nadyozhin 1992; see also Imshennik and Zabrodina 1999). The complex problem of the behavior of the outer layers in SN progenitors, in particular, in circumpolar vacuum holes, needs further study.

Having expanded in the transverse direction, the explosion remnants of a low-mass NS moving at a high velocity in an equatorial circular orbit eventually reach the inner surface of such toroidal atmospheres and produce shock waves inside them. Note, for completeness, that the rotation axes of the binaries and the atmospheres coincide, being the rotation axes of the original stellar iron cores. Thus, shock fronts propagate from the centers of the atmospheres to their periphery, which seem to gradually acquire the characteristic features established in our previous two-dimensional hydrodynamic calculations of asymmetric explosions (Aksenov *et al.* 1997; Imshennik and Zabrodina 1999; Zabrodina and Imshennik 2000). Nevertheless, the new problems of shock generation and propagation in toroidal atmospheres differ significantly because of the nonuniform density distributions inside the atmospheres. However, since the mean densities of these atmospheres are approximately equal to the constant density $\rho_0 = 5.66\times10^5$ g cm^{-3}

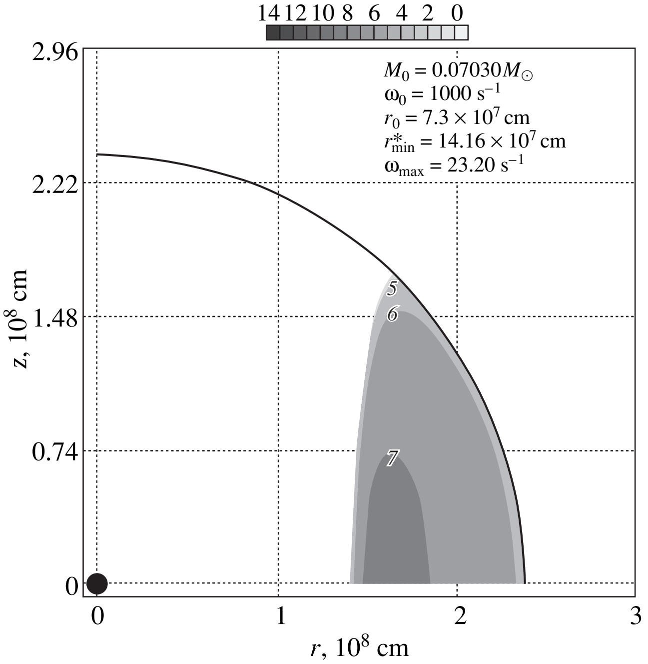

Fig. 5. Isochores in the θ–r plane of spatial variables showing the atmospheric density distribution $\rho(r, \theta)$ for a polytropic equation of state with $\gamma = 5/3$, a central mass $M_{\rm p} = 1.8M_\odot$, and rotation parameters $r_0 = 73\times10^6$ cm and $\omega_0 = 1000$ s^{-1}.

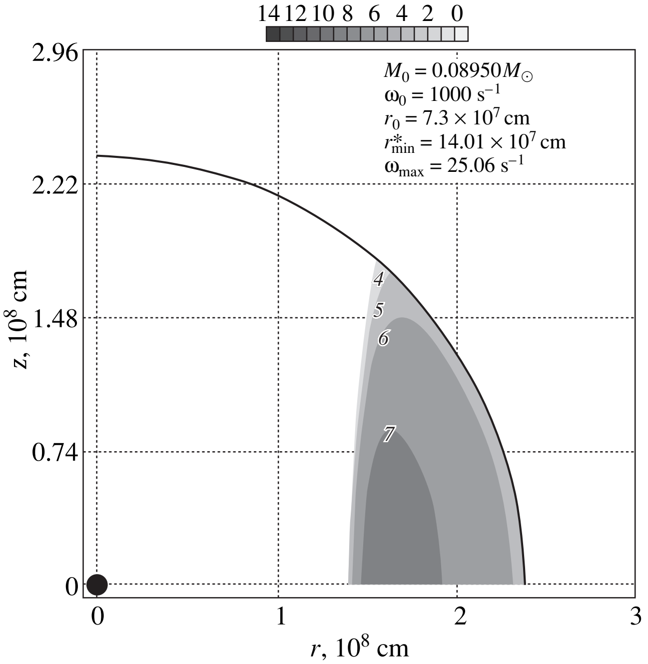

Fig. 6. Same as Fig. 5 for $\gamma = 4/3$.

assumed in our previous calculations, such differences will vanish in the course of time. In addition, the dependence of the hydrodynamic pattern on the preshock matter density is generally weak. In particular, the previously found high degree of asymmetry for late times must be the same in the new statement of the problem. Next, in all probability, the iron dissociation in toroidal atmospheres is considerably reduced because of the relatively high matter density near the inner surface of these atmospheres. After shock generation, the circumpolar vacuum cavities must be partly filled with the matter that passed through the shock front. We conclude that new calculations of asymmetric explosions with allowance for the steady-state toroidal atmospheres obtained here are undoubtedly of considerable interest. However, it would apparently be unreasonable to expect radical changes in the hydrodynamic pattern of explosion compared to our previous calculations in the approximation of homogeneous atmospheres.

ACKNOWLEDGMENTS

We wish to thank M.S. Popov for taking an active part in the discussion of this study. One of us (V.S. Imshennik) is also grateful to Prof. Hillebrandt, who emphasized the importance of the existence of steady-state atmospheres in binaries of neutron stars for the explosion scenario of collapsing supernovae under consideration.

REFERENCES

1. A. G. Aksenov, Pis'ma Astron. Zh. **25**, 163 (1999) [Astron. Lett. **25**, 127 (1999)].
2. A. G. Aksenov, S. I. Blinnikov, and V. S. Imshennik, Astron. Zh. **72**, 717 (1995) [Astron. Rep. **39**, 638 (1995)].
3. A. G. Aksenov and V. S. Imshennik, Pis'ma Astron. Zh. **20**, 32 (1994) [Astron. Lett. **20**, 24 (1994)].
4. A. G. Aksenov, E. A. Zabrodina, V. S. Imshennik, and D. K. Nadyozhin, Pis'ma Astron. Zh. **23**, 779 (1997) [Astron. Lett. **23**, 677 (1997)].
5. J. L. Houser, J. M. Centrella, and S. C. Smith, Phys. Rev. Lett. **72**, 1314 (1994).
6. V. S. Imshennik, Pis'ma Astron. Zh. **18**, 489 (1992) [Sov. Astron. Lett. **18**, 194 (1992)].
7. V. S. Imshennik, Space Sci. Rev. **74**, 325 (1995).
8. V. S. Imshennik and D. K. Nadyozhin, Pis'ma Astron. Zh. **18**, 195 (1992) [Sov. Astron. Lett. **18**, 79 (1992)].
9. V. S. Imshennik and D. V. Popov, Pis'ma Astron. Zh. **20**, 620 (1994) [Astron. Lett. **20**, 529 (1994)].
10. V. S. Imshennik and D. V. Popov, Pis'ma Astron. Zh. **24**, 251 (1998) [Astron. Lett. **24**, 206 (1998)].
11. V. S. Imshennik and E. A. Zabrodina, Pis'ma Astron. Zh. **25**, 25 (1999) [Astron. Lett. **25**, 93 (1999)].
12. V. S. Imshennik, D. K. Nadyozhin, and V. S. Pinaev, Astron. Zh. **44**, 768 (1967) [Sov. Astron. **11**, 617 (1967)].
13. L. D. Landau and E. M. Lifshitz, *Statistical Physics* (Nauka, Moscow, 1976; Pergamon, Oxford, 1980).
14. K. V. Manukovskiĭ, Bachelor's Qualification Works (Moscow Institute of Physics and Technology, Moscow, 1999).
15. L. Mestel, in *Stellar Structure*, Ed. by L. Aller and D. McLaughlin (Univ. of Chicago Press, Chicago, 1965; Mir, Moscow, 1970), p. 249.
16. J.-L. Tassoul, *Theory of Rotating Stars* (Princeton Univ. Press, 1978).
17. E. A. Zabrodina and V. S. Imshennik, Pis'ma Astron. Zh. **26**, 665 (2000) [Astron. Lett. **26**, 572 (2000)].

Translated by V. Astakhov

Astronomy Letters, Vol. 26, No. 12, 2000, pp. 797–801. Translated from Pis'ma v Astronomicheskiĭ Zhurnal, Vol. 26, No. 12, 2000, pp. 927–932.
Original Russian Text Copyright © 2000 by Chugaĭ.

Monte Carlo Simulations of Supernova Light Curves and the Hypernova SN 1998bw

N. N. Chugaĭ*
Institute of Astronomy, Russian Academy of Sciences, ul. Pyatnitskaya 48, Moscow, 109017 Russia

Received June 19, 2000

Abstract—We propose a method for computing the bolometric light curves of type Ia and Ib/c supernovae based on Monte Carlo simulations of unsteady-state radiative transfer. The method is used to analyze the bolometric light curve of the unusual type Ib/c supernova SN 1998bw associated with GRB 980 425. We show that the previously noted inconsistency in the behavior of simulated light curves at early and late stages, which is attributable to asymmetry effects, can be overcome in a spherically symmetric model. Agreement with observations requires complete ^{56}Ni mixing and a higher matter density in the central part of the envelope in the velocity range $v < 5000$ km s^{-1} compared to standard models. © *2000 MAIK “Nauka/Interperiodica”.*

Key words: *supernovae and supernova remnants*

INTRODUCTION

In general, computing a supernova light curve requires the simultaneous solution of hydrodynamic and unsteady-state radiative-transfer equations (Imshennik and Nadyozhin 1964; Falk and Arnett 1977; Höflich *et al.* 1993). At the same time, the optical luminosity for SN Ia and SN Ib/c, which resulted from explosions of compact stars, is virtually independent of the internal energy stored in the envelope after shock passage; it is determined by the radioactive decay of ^{56}Ni. On the other hand, the energy of radioactive decay for such supernovae has no appreciable effect on the subsequent expansion kinematics. Both these circumstances allow the problem of computing a light curve to be simplified. Actually, it remains only to solve the unsteady-state transfer equation and the energy equation in an envelope model specified by the mass and ^{56}Ni velocity distributions. Moreover, adiabatic internal-energy losses can be disregarded; as a result, computing a bolometric light curve reduces to solving the unsteady-state transfer equation for given opacity.

Below, we propose a method for computing SN Ia and SN Ib/c light curves based on Monte Carlo simulations of unsteady-state radiative transfer. The Monte Carlo method for computing light curves is appealing in that a sufficiently accurate result is obtained in a simple physical model with a compact computational algorithm. Furthermore, this method can be naturally generalized to the three-dimensional case. Here, however, we restrict our analysis to a spherically symmetric model. We first describe the method itself and then use it to analyze the bolometric light curve of the unusual supernova (hypernova) SN 1998bw, which was identified with GRB 980 425 (Galama *et al.* 1998; Iwamoto *et al.* 1998).

The problem is that the hydrodynamic model (Iwamoto *et al.* 1998), while reproducing the SN 1998bw light curve near its maximum, is inconsistent with the late stage (Nomoto *et al.* 2000). This forced Nomoto *et al.* (2000) to assume the necessity of departures from spherical symmetry. On the other hand, it is well known that, as yet, there is no self-consistent hydrodynamic model for SN 1998bw and the question of what the actual envelope structure is remains open. Below, we show that the mass and ^{56}Ni distributions can be determined in a spherically symmetric model, which satisfactorily reproduces the observed light curve of SN 1998bw.

MODEL

Consider a freely expanding supernova envelope (kinematics $v = r/t$) with given distributions of density $\rho(v)$ and radioactive ^{56}Ni. The internal energy stored in the envelope after shock passage is assumed to be negligible compared to the internal energy contributed to the envelope by the decay of radioactive nuclei. This assumption is quite justified for supernovae produced by explosions of compact stars (SN Ia and SN Ib/c), because, in this case, virtually the entire initial internal energy is expended on the work of radiation pressure forces at an early expansion stage (of the order of a day) and does not contribute appreciably to the light curve at the subsequent stage. The problem involves computing the supernova bolometric light curve for given density and ^{56}Ni distributions by assuming a gray (i.e., frequency-independent) absorption coefficient.

---

* E-mail address for contacts: nchugai@inasan.rssi.ru

Computation of the bolometric light curve can be arbitrarily divided into two stages: (1) computing the energy deposition $\epsilon(v, t)$ (erg cm^{-3} s^{-1}) of radioactive ^{56}Ni–^{56}Co–^{56}Fe decay as a function of velocity and time and (2) computing the unsteady-state transfer of optical radiation. We computed the gamma-ray energy deposition by the Monte Carlo method, which is commonly used to model gamma-ray scattering in supernovae (Bartunov *et al.* 1987; Grebenev and Sunyaev 1987). The following justified assumptions were made for positrons: local deceleration and instantaneous deposition compared to the expansion time.

The second part of the problem—computing unsteady-state radiative transfer—is central in the proposed method. Generally, the unsteady-state energy equation along with the unsteady-state radiative-transfer equation must be considered in this case. Fortunately, for SN Ia and SN Ib/c, there is no need to solve the energy equation for matter in the gray approximation. Let us show that this is the case. To this end, we estimate the ratio of the radiation energy density to the internal energy density of thermal particle motion in the envelope at maximum light by assuming that the optical and gamma-ray radiation is virtually locked. In this case, the energy equation for specific energy density e (erg g^{-1}) is

$$\frac{de}{dt} + p\frac{d}{dt}\left(\frac{1}{\rho}\right) = q\lambda\exp(-\lambda t), \qquad (1)$$

where p is the pressure, ρ is the matter density, $q = 2.95 \times 10^{15} Z_{56}$ erg g^{-1} is the specific energy of radioactive ^{56}Ni–^{56}Co decay (Z_{56} is the mass fraction of ^{56}Ni), and λ is the inverse mean lifetime of ^{56}Ni ($1/\lambda = 8.8$ days). If we take into account the radiation alone (below, it will become clear that this is admissible), the solution to the energy equation is

$$e = \frac{q}{\lambda t}[1 - (1 + \lambda t)\exp(-\lambda t)]. \qquad (2)$$

Having determined the temperature from $aT^4 = e\rho$, we obtained the ratio of the radiation and thermal energy densities for typical parameters of the SN 1998bw model by assuming a uniformly mixed oxygen envelope of constant density with a mass of $7M_\odot$, a kinetic energy of 2×10^{52} erg, and a ^{56}Ni mass of $0.6M_\odot$ (the model of SN 1998bw) of the order of 10^2 and 10^3, respectively, one and ten days after the explosion. It thus follows that, for characteristic adiabatic cooling times of t and $t/2$ for radiation and matter, respectively, the adiabatic internal-energy losses of matter account for a negligible fraction (of the order of 10^{-2}) of the adiabatic energy losses of radiation. The radiation-to-matter energy ratio for SN Ia is an order of magnitude higher, whereas this ratio for normal SN Ib/c with $M_{\rm Ni} = 0.07M_\odot$ is slightly lower (<0.05). Thus, the light curves of SN Ia and SN Ib/c can be computed by taking into account the radiation energy alone.

We represent the solution to the unsteady-state problem of radiative transfer in terms of the distribution function of photon escape time (Sobolev 1952). A static case with variable sources was considered in the above paper. In a modification for an expanding medium, Sobolev (1979) also took into account the time dependence of its density. However, for an expanding medium, in particular, for supernovae, apart from a delay of radiation in the medium, the radiation energy losses through the work of pressure forces (adiabatic energy losses) must be taken into account, which is tantamount to allowing for the Doppler effect in a microscopic description. Note that the remaining effects of the order of v/c, aberration and advection, are absent: the former because there are no transverse motions for kinematics $v = r/t$ in a comoving frame of reference, and the latter because of the very essence of a Monte Carlo microscopic description of photon transfer.

Let us introduce the distribution function $f(v, t_1, t)$ of escape time t for optical photons emitted at time t_1 by an element of matter moving at velocity v. The bolometric luminosity can then be expressed in terms of the energy release $\epsilon(v, t)$ and $f(v, t_1, t)$ as follows:

$$L(t) = 4\pi \int_0^{v_{\max}} v^2 dv \int_0^t t_1^3 \epsilon(v, t_1) A(t_1, t) f(v, t_1, t) dt_1, \qquad (3)$$

where $A(t_1, t)$ is the factor that allows for adiabatic energy losses; it is equal to the fraction of the initial energy of a photon leaving the envelope.

The photon residence time in the medium is the sum of the time $t_{\rm r}$ spent by the photons between scatterings and the time $t_{\rm m}$ between their absorption and emission. At an optically dense expansion phase, the energy exchange between radiation and matter takes place rapidly compared to the expansion time. Therefore, the ratio of the above times is equal to the ratio of the corresponding energy densities of radiation and matter: $t_{\rm m}/t_{\rm r} \approx U_{\rm r}/U_{\rm m}$. In contrast to estimating the adiabatic energy losses, one should take into account the total energy, which is the sum of the energy of translational particle motion, the excitation energy, and the ionization energy. The latter appreciably exceeds the energy of translational motion and the excitation energy. In the envelope model considered above, we obtain $t_{\rm m}/t_{\rm r} \approx 0.1$ and 0.03 one and ten days after the explosion, respectively. Thus, disregarding the time spent by the photons in the absorbed state, in the form of internal energy of the matter, at $t > 1$ day, we underestimate the photon residence time in the envelope by less than 10%; the error decreases with time. With the same accuracy, the energy of radioactive decay contributed to the matter can be assumed to be instantaneously transformed into optical photons.

It should be emphasized that disregarding the delay of photons in the absorbed state generally requires justification. In this connection, it is pertinent to recall the following paradox: the Kelvin time for the Sun exceeds the diffusion time by an order of magnitude. The paradox stems from the fact that, when the diffusion time is estimated in a standard way, the time spent by a photon in the absorbed state in the form of internal energy of the matter is disregarded.

As was noted above, the adiabatic radiation-energy losses during medium expansion in a microscopic treatment are described in terms of the Doppler effect experienced by individual photons as they walk in the medium. In a comoving frame of reference in a homologically expanding medium, the redshift of photons in flight is given by

$$d\ln\nu/d\ln t = -1. \tag{4}$$

This equation follows from a more general equation for photons in a comoving frame of reference in a medium with Hubble kinematics $d\ln\nu = -d\ln a$ (see Zel'dovich and Novikov 1975), where a is a scaling factor. Equation (4) also describes the photon redshift in the case of multiple conservative photon scattering in a medium if the resultant photon frequency and residence time in the medium are calculated by adding up the results on individual segments of a polygonal trajectory. It follows from Eq. (4) that, if a photon with frequency ν_1 is generated at time t_1 and leaves the envelope at time t after multiple scattering, its final frequency is $\nu = \nu_1(t_1/t)$. Clearly, the adiabatic photon cooling factor is $A(t_1, t) = \nu/\nu_1 = t_1/t$. Note that the requirement of conservative scattering for individual photons is actually redundant. Photons can break up during cascade transitions or through true absorption and subsequent reemission. When the bolometric luminosity is computed, only the energy conservation of a photon packet during the interaction of matter and radiation in general is of importance, as is the case on time scales of the order of $t_m \ll t$.

All the above considerations allow a simple Monte Carlo algorithm for computing light curves to be realized. At each time step t_1, simulated photons are randomly generated in a spherical layer of the envelope with a distribution function proportional to $\epsilon(v, t_1)v^2\Delta v$. We then compute the distribution function of escape time $f(v, t_1, t)$ and the adiabatic cooling factor $A(t_1, t)$ by the Monte Carlo method, which are used to compute the light curve in accordance with relation (3). When the photon propagation in the envelope is computed, one should take into account the fact that the matter density falls off with time as $\rho \propto t^{-3}$.

THE MASS AND ^{56}Ni DISTRIBUTIONS IN SN 1998bw

The type Ib/c supernova SN 1998bw before its explosion appears to have been a Wolf–Rayet star (Iwamoto *et al.* 1998; Woosley *et al.* 1999); i.e., it was compact enough to disregard the internal energy stored after shock propagation and to guarantee the applicability of the method for computing light curves described above. As a standard model, we consider the model of Iwamoto *et al.* (1998): an envelope with a total mass of $11M_\odot$, a kinetic energy of 3×10^{52} erg, and a ^{56}Ni mass of $0.7M_\odot$. We describe the density distribution in the envelope by an exponential law $\rho \propto \exp(-v/u)$, which satisfactorily reproduces the density distribution in the hydrodynamic model of a supernova associated with the instantaneous explosion of a compact progenitor. An example of this kind is the density distribution in the CO60 model (Nomoto *et al.* 2000), which matches an exponential law with an accuracy better than 25% in the velocity range 2000–20 000 km s^{-1} and in the density range of five orders of magnitude. At the same time, the structure of the inner layers may depend on the explosion mechanism (Imshennik and Nadyozhin 1988), which is not known for SN 1998bw. For this reason, we describe the density as a superposition of two exponential laws (the core and halo model) with core and halo masses M_1 and M_2 and with characteristic exponential velocity scales u_1 and u_2. Thus, in general, the model is characterized by core and halo parameters, namely, by their masses M_1 and M_2, velocities u_1 and u_2, kinetic energies E_1 and E_2, and ^{56}Ni mass (see the table).

The optical opacity is computed as a sum of the Thomson and Rosseland opacities for free–free and bound–free transitions. We computed the degree of ionization by using the Saha formula in the average-ion approximation (Zel'dovich and Raizer 1963). The radiation temperature inside the envelope was determined from (2) for the specific energy density with allowance for the relation $aT^4 = e\rho$ in the case of uniform ^{56}Ni mixing in the envelope. The opacity was found to vary only slightly along the radius; for this reason and to speed up the computation, it was assumed to be constant along the radius. However, the time dependence is fairly strong and, for a typical model of the SN 1998bw envelope composed of oxygen matter, the time dependence of opacity can be fitted at $t > 1$ day, with an acceptable accuracy, by the relation $k = 0.13/[1 + (t/10)^2]$ cm^2 g^{-1}. The nonthermal ionization is negligible at $t < 20$ days. We disregard the contribution of lines to the opacity.

Our computations show that, to ensure a rapid rise in luminosity, the radioactive nickel must be present virtually in the entire envelope. In model bw3 (table), which is equivalent to the CO138 model (Iwamoto *et al.* 1998), ^{56}Ni is assumed to be uniformly mixed throughout the entire envelope up to its boundary (≈40000 km s^{-1}). This is in qualitative agreement with the assertion of Iwamoto *et al.* (1998) that ^{56}Ni must be present near the surface. The light curve of model bw3 (Fig. 1) reproduces the luminosity before the maximum light and at $t > 100$ days; however, the luminosity is enhanced during the intermediate period compared to the observations

The CO138H model, which also describes well the maximum phase (Nomoto *et al.* 2000), have slightly different parameters: $M = 10M_\odot$, $E = 6 \times 10^{52}$ erg, and $M_{\rm Ni} = 0.5M_\odot$. Model bw4 (see table) is similar to the

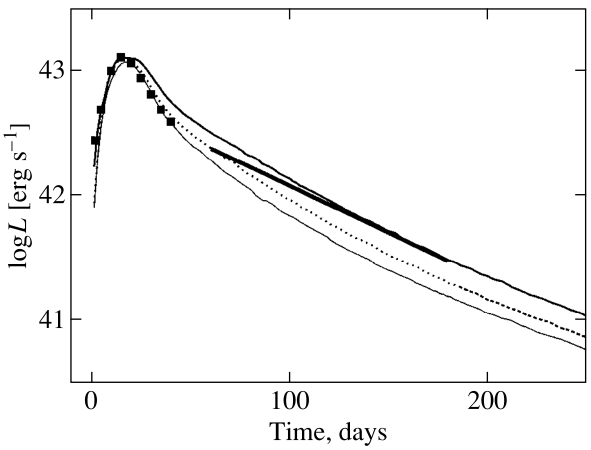

Fig. 1. The bolometric light curve of SN 1998bw. The squares represent the observed bolometric luminosity estimated by Woosley *et al.* (1999); the heavy segment represents the observed bolometric luminosity from Nomoto *et al.* (2000). The solid curves correspond to models bw3 (heavy line) and bw4 (thin line); the dotted line corresponds to models bw1.

CO138H model but differs by a lightly larger amount of ^{56}Ni, which is uniformly mixed up to 30 000 km s^{-1}. This model is actually in better agreement with observations at maximum light (Fig. 1) than model bw3; however, it shows a significant deficit in luminosity at $t > 50$ days, which is also present in the computations of Nomoto *et al.* (2000).

The decrease in optical depth, which was obtained in model bw4 by increasing the energy at fixed mass, can also be achieved by decreasing the mass. Like bw4, model bw1 with $M = 7M_\odot$, $E = 2 \times 10^{52}$ erg, and $M_{\rm Ni} = 0.6M_\odot$ satisfactorily reproduces the maximum (Fig. 1) and is characterized by a low luminosity at the late stage. Note that, in this model, ^{56}Ni is uniformly mixed in the velocity range $v < 20\,000$ km s^{-1}. At $v > 20\,000$ km s^{-1}, the nickel abundance is a factor of 2 lower.

To reconcile the light curves at the early and late stages, we added a dense core with an exponential density distribution to the model with a purely exponential density distribution. Having computed a grid of models, we found satisfactory agreement with the observed light curve (Fig. 2) for model bw2 (see the table), which consists of a $2M_\odot$ core and a $5M_\odot$ halo. The kinetic energy of the halo (1.3×10^{52} erg) is lower than that for model bw1, in accordance with the requirement of density invariance in the outer layers, which is determined by modeling the spectrum at the photospheric stage (Iwamoto *et al.* 1998). Figure 3 compares the matter and ^{56}Ni density distributions for models bw2 and bw1. The central density in model bw2 is a factor of 7, 5, and 14 higher than that in models bw1, bw3, and bw4, respectively. Recall that models bw3 and bw4 are equivalent to the CO138 (Iwamoto *et al.* 1998) and CO138H (Nomoto *et al.* 2000) models, respectively.

With all the uncertainty in the details of the ^{56}Ni and total-density distributions, model bw2 gives a general idea of the pattern of distribution of the above quantities in a spherically symmetric model, which is consistent with the observed bolometric light curve. The salient features of the empirical model for SN 1998bw are as follows: (1) the envelope must be appreciably denser in the central zone ($v < 5000$ km s^{-1}) than it is in the CO138 (Iwamoto *et al.* 1998) and CO138H (Nomoto *et al.* 2000) models and (2) ^{56}Ni must be mixed virtually uniformly throughout the entire envelope. It should be emphasized that, when searching for an optimum model (model bw2), we sought to reproduce the density in the outer layers (10 000–40 000 km s^{-1}), which is typical of model bw3 and is virtually equivalent to the density in the CO138 model (Iwamoto *et al.* 1998) and, in turn, is in qualitative agreement with the presence of high-velocity gas absorption lines. For this reason, the uncertainty in the kinetic energy and mass is

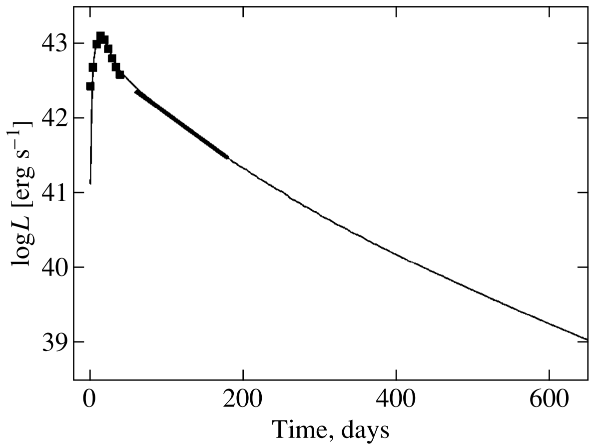

Fig. 2. The bolometric light curve of SN 1998bw: observations (see Fig. 1) and model bw2 (thin solid line).

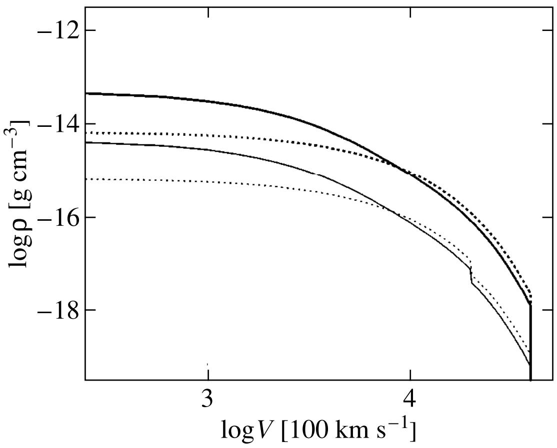

Fig. 3. The matter and ^{56}Ni density distributions on day 100 in models bw2 (solid lines) and bw1 (dotted lines). The ^{56}Ni density corresponds to the lower curve for each of the two models.

Model parameters

Model	M_1	M_2	v_1	v_2	E_1	E_2	$M_{\rm Ni}$
	$M_\odot$		km s^{-1}		10^{51} erg		$M_\odot$
bw3	0	11	0	4770	0	30	0.7
bw4	0	10	0	7070	0	60	0.6
bw1	0	7	0	4880	0	20	0.6
bw2	2	5	1710	4730	0.7	13	0.56

essentially determined by uncertainty in the outer-layer densities estimated from the photospheric spectra of SN 1998bw (Iwamoto *et al.* 1998).

CONCLUSION

We have proposed a method for Monte Carlo simulations of supernova light curves, which proves to be efficient enough in computing the bolometric light curves of supernovae produced by explosions of compact stars, i.e., SN Ia and SN Ib/c. Using this method to study the interesting anomalous type Ib/c supernova SN 1998bw has shown that the bolometric light curve at the early and late stages can be explained in terms of a spherically symmetric model. Our empirical model of the density distribution for SN 1998bw is peculiar in that it has a denser core than does the model of Iwamoto *et al.* (1998) and virtually uniform ^{56}Ni mixing. Interestingly, the conclusion about a higher central density of the envelope than that in the model of Iwamoto *et al.* (1998) is actually contained in Nomoto *et al.* (2000); however, this is interpreted as evidence for the asymmetry of the SN 1998bw envelope. In fact, as we verified, the light curve by itself requires no departures from sphericity.

The discrepancy between the empirical model and hydrodynamic models of SN 1998bw is further emphasized by the fact that complete ^{56}Ni mixing in the envelope is also inconsistent with the hydrodynamic model of instantaneous explosion of a CO star (Nomoto *et al.* 2000). The two facts provide circumstantial evidence that the envelope ejection was slow compared to the hydrodynamic time of the bulk of the SN progenitor envelope ($\sim 10^2$ s), because, in this case, the conditions for efficient envelope mixing are more favorable and the density distribution definitely differs from that in the instantaneous explosion model. Note in this connection that slow energy release on a time scale of 10^2–10^3 s is a characteristic property of the models for massive-star collapse followed by disk accretion of matter onto a black hole (MacFadyen *et al.* 1999). A possible scenario for the SN 1998bw explosion could appear as the envelope ejection and mixing in the regime of expansion of a central hot bubble, in which energy was injected with a time scale $\geq 10^3$ s in the form of hot jets generated during disk accretion onto a black hole (MacFadyen *et al.* 1999).

ACKNOWLEDGMENTS

I proposed the method for simulating supernova light curves described here during my visit to the Osservatorio Astronomico di Trieste at the invitation of P. Mazzali. This work was supported by the Russian Foundation for Basic Research (project no. 98-02-16404).

REFERENCES

1. O. S. Bartunov, S. I. Blinnikov, L. V. Levakhina, and D. K. Nadyozhin, Pis'ma Astron. Zh. **13**, 744 (1987) [Sov. Astron. Lett. **13**, 313 (1987)].
2. S. W. Falk and D. W. Arnett, Astrophys. J., Suppl. Ser. **33**, 515 (1977).
3. T. J. Galama, P. M. Vreeswejk, J. van Paradijs, *et al.*, Nature **395**, 670 (1998).
4. S. A. Grebenev and R. A. Sunyaev, Pis'ma Astron. Zh. **13**, 945 (1987) [Sov. Astron. Lett. **13**, 397 (1987)].
5. P. Höflich, E. Müller, and A. Khokhlov, Astron. Astrophys. **268**, 570 (1993).
6. V. S. Imshennik and D. K. Nadyozhin, Astron. Zh. **41**, 829 (1964) [Sov. Astron. **8**, 664 (1964)].
7. V. S. Imshennik and D. K. Nadyozhin, Usp. Fiz. Nauk **156**, 561 (1988).
8. K. Iwamoto, P. A. Mazzali, K. Nomoto, *et al.*, Nature **395**, 672 (1998).
9. A. I. MacFadyen, S. E. Woosley, and A. Heger, astro-ph/9910034.
10. K. Nomoto, P. A. Mazzali, T. Nakamura, *et al.*, in *Supernovae and Gamma Ray Bursts*, Ed. by M. Livio (Cambridge Univ. Press, Cambridge, 2000) (in press).
11. V. V. Sobolev, Astron. Zh. **29**, 406 (1952).
12. V. V. Sobolev, Astrofizika **15**, 401 (1979).
13. S. E. Woosley, R. G. Eastman, and B. P. Schmidt, Astrophys. J. **516**, 788 (1999).
14. Ya. B. Zel'dovich and I. D. Novikov, *Structure and Evolution of Universe* (Nauka, Moscow, 1975).
15. Ya. B. Zel'dovich and Yu. P. Raizer, *Physics of Shock Waves and High-Temperature Hydrodynamic Phenomena* (Nauka, Moscow, 1963; Academic, New York, 1966).

Translated by A. Dambis

Astronomy Letters, Vol. 26, No. 12, 2000, pp. 802–805. Translated from Pis'ma v Astronomicheskiĭ Zhurnal, Vol. 26, No. 12, 2000, pp. 933–937.
Original Russian Text Copyright © 2000 by Zinchenko.

Correlations between Parameters of Massive Cores in Interstellar Molecular Clouds

I. I. Zinchenko*

Institute of Applied Physics, Russian Academy of Sciences, ul. Ul'yanova 46, Nizhniĭ Novgorod, 603600 Russia

Received December 3, 1999; in final form, April 13, 2000

Abstract—Based on a CS and $C^{34}S$ survey of dense molecular-cloud cores in regions of high-mass-star formation, we analyze the correlations between line width and size (ΔV–L), as well as between mean density and size (n–L). There is virtually no correlation between ΔV and L ($\Delta V \propto L^{0.2 \pm 0.1}$). The velocity dispersion is several times higher in absolute value than that in CO and dark clouds of the same size. The mean density decreases with increasing size considerably faster than L^{-1}, so the column density also decreases. Possible effects of selection and of the technique for determining object parameters on these results are discussed. Possible physical causes of the above correlations are considered. *© 2000 MAIK "Nauka/Interperiodica".*

Key words: *interstellar medium, gaseous nebulae*

INTRODUCTION

Studies of molecular clouds in lines of various CO isotopes, as well as CO, NH_3, and CS observations of dark clouds, have revealed statistically significant correlations between cloud size and velocity dispersion, between cloud size and mean density, etc. (see, e.g., Larson 1981; Myers 1985). These correlations may result, to some extent, from selection effects (Kegel 1989). Nevertheless, they can also reflect actual physical processes in clouds, for example, turbulence.

The first such studies in CO and ^{13}CO lines covered mostly tenuous clouds, because the corresponding transitions are excited at gas densities $n \sim 10^3$ cm^{-3}. Subsequent observations of molecules excited at higher densities allowed the above correlations to be analyzed for dense clumps inside molecular clouds or cores in which star formation takes place (see, e.g. Fuller and Myers 1992; Caselli and Myers 1995; Goodman *et al.* 1998). These studies showed, in particular, a difference between the low-mass cores in dark nebulae and the cores in regions of high-mass-star formation. For the latter, the slope α of the power-law dependence ΔV–L ($\Delta V \propto L^{\alpha}$) proved to be considerably smaller than that for the former (~0.2 and ~0.5, respectively). A number of theoretical papers have aimed at interpreting these correlations [see Pirogov and Zinchenko (1998) and references therein].

Recently, we have extensively studied dense clumps in molecular clouds by their emission in lines of CS, HCN, and HCO^+ and their isotopes (Zinchenko *et al.* 1989, 1994, 1995, 1998; Pirogov *et al.* 1995). We investigated mostly dense cores in regions of high-mass-star formation. The results of an analysis of the correlation between velocity dispersion and size based on HCN and HCO^+ observations were published by Pirogov and Zinchenko (1998). However, the size of the sample analyzed in the above paper was limited (about ten objects). Since the maps were incomplete, the cloud sizes were estimated from observations of several points around the emission peak.

The most homogeneous and representative data set was obtained by surveying molecular clouds toward H_2O masers in CS and $C^{34}S$ lines. During this survey, we thoroughly mapped most sources in the line of the main isotope and used observations of optically thin $C^{34}S$ lines to determine basic parameters of the objects: their sizes, masses, mean densities, and velocity dispersions. It is these data that we discuss here.

DESCRIPTION OF THE DATA SET

Our analysis is based on our CS and $C^{34}S$ survey of dense molecular clumps toward H_2O masers carried out in 1993–1996 with the 15-m SEST radio telescope in Chile and with the 20-m OSO radio telescope in Onsala (Sweden). These observations were described in detail by Zinchenko *et al.* (1995, 1998). We also observed several clouds with the 14-m Metsahovi telescope in Finland by using a similar technique (Zinchenko *et al.* 1994).

These observations yielded isophotal maps for most of the cores discovered in the CS J = 2–1 line. CS emission peaks were observed in the $C^{34}S$ J = 2–1 and CO J = 1–0 lines. Based on these data, we determined the source sizes, their masses, the mean gas densities, and other parameters. We will not go into detail on these estimates, which are presented in the above papers, and note only the most important points.

---

* E-mail address for contacts: zin@appl.sci-nnov.ru

To estimate the core sizes and masses and the mean gas density, we used spectrophotometric distances to stars in nearby HII regions or, if such data were unavailable, the kinematic distances computed from measured radial velocities. The error in kinematic distances depends strongly on Galactic longitude and is particularly large toward the Galactic center and anticenter and in the tangential direction. It is ~0.5–1 kpc for most of the sources.

The next step in our data analysis was to estimate the core sizes, masses, and densities. To this end, we first determined the solid angles (Ω) of the sources by integrating line intensities within our maps. The angular sizes were calculated from $\theta = \sqrt{(4/\pi)\Omega}$. Using the source distances d, we then determined their linear sizes L. The mean gas densities were calculated from $\bar{n} = N_L(H_2)/L$. We inferred the hydrogen column densities by assuming that the CS abundance relative to H_2 was $X(CS) = 4 \times 10^{-9}$ (Irvine *et al.* 1987). The core masses were estimated using the formula

$$M = \mu m N_L(H_2)\Omega d^2, \qquad (1)$$

where m is the mass of the hydrogen molecule and μ is the ratio of the total gas mass to the hydrogen mass ($M = 1.36$). We used the source-averaged CS line widths to compute the virial core masses

$$M_{\text{vir}} = \frac{5}{3}\frac{\sigma^2 R}{G} = \frac{5}{16\ln 2}\frac{L\overline{\Delta V}^2}{G}, \qquad (2)$$

where σ is the three-dimensional velocity dispersion and G is the gravitational constant.

We were unable to determine the masses and densities for some (about 20%) of the cores by the method described above because of the lack of insufficiently high quality $C^{34}S$ data. In these cases, we took their virial masses as mass estimates and used them to compute the densities. This approach is justified by the fact that they are very similar for the cores whose masses were inferred by both methods (i.e., the objects under study are in virial equilibrium).

RESULTS

The correlations between size and line width (L–ΔV), as well as between size and density (L–n), are traditionally discussed in the literature. It should be noted that lines in these objects are generally broadened by small-scale differential motions of cloud parts and the line widths considerably exceed the thermal widths. The figure shows our data on these correlations for the data set described above.

There is no statistically significant correlation between L and ΔV (the correlation coefficient is $\rho \approx 0.3$ and the significance of rejecting the hypothesis of a zero correlation is ~60%). The correlation coefficient between L and n is $|\rho| \approx 0.7$, and the correlation is highly significant. The best fits to the above relations obtained by ordinary least squares (i.e., by minimizing the sum of the squares of deviations along the y axis) are

$$\Delta V = (3.3 \pm 0.2) L_{\text{pc}}^{0.16 \pm 0.08} \text{ km s}^{-1}, \qquad (3)$$

$$n = (2.2 \pm 0.3) \times 10^4 L_{\text{pc}}^{-1.6 \pm 0.2} \text{ cm}^{-3}. \qquad (4)$$

However, if there is uncertainty in the data along both coordinates, it would be more appropriate to derive regression relations by other methods, for example, by minimizing the sum of the squares of deviations from the regression line orthogonal to it. For this approach, we derived the following relations by using the SLOPES code (Feigelson and Babu 1992):

$$\Delta V = (3.1 \pm 0.2) L_{\text{pc}}^{0.24 \pm 0.10} \text{ km s}^{-1}, \qquad (5)$$

$$n = (4.2 \pm 1.0) \times 10^4 L_{\text{pc}}^{-2.9 \pm 0.4} \text{cm}^{-3}. \qquad (6)$$

Note that the high degree of correlation between mean density and size can, at least in part, stem from the fact that these parameters are not independent: the mean density is computed from measured column densities and sizes. Therefore, it seems reasonable to analyze the correlation between these parameters (column density and size), which are inferred independently of one another. The corresponding plot is shown in Fig. 1c. Here, the correlation coefficient is considerably lower ($|\rho| \approx 0.35$), but the correlation remains statistically significant: the hypothesis of a zero correlation is rejected at a significance level of ~1%. The exponent of the $N_L(L)$ relation is -0.6 ± 0.2 and -3.4 ± 1.2 for the "ordinary" and "orthogonal" least-squares methods, respectively. The difference between these estimates is large, but of importance is the very fact of decrease in column density with increasing size, which seems to have been firmly established.

RESULTS AND DISCUSSION

The slope for the L–ΔV relation agrees with the results of Casseili and Myers (1995), who found $\Delta V \propto L^{0.21 \pm 0.03}$ for the massive cores in the molecular clouds Orion *A* and *B*. This slope is smaller than that for the lower mass cores in cold dark clouds (~0.5).

As for the L–n relation, to the best of our knowledge, it differs markedly from all the previous ones, which were close to $n \propto L^{-1}$. Analyzing objects of the same class, Plume *et al.* (1997) found no correlation between size and density at all. However, they used the densities estimated from an analysis of CS excitation conditions based on multifrequency data, i.e., the densities in line formation regions. The mean densities discussed here can differ from them by several orders of magnitude (which suggests a low factor of volume filling by emitting clumps).

Of importance in studying these kinds of correlations is to properly allow for the possible effects of selection by particular parameters. In particular, it has repeatedly been pointed out in the literature that the

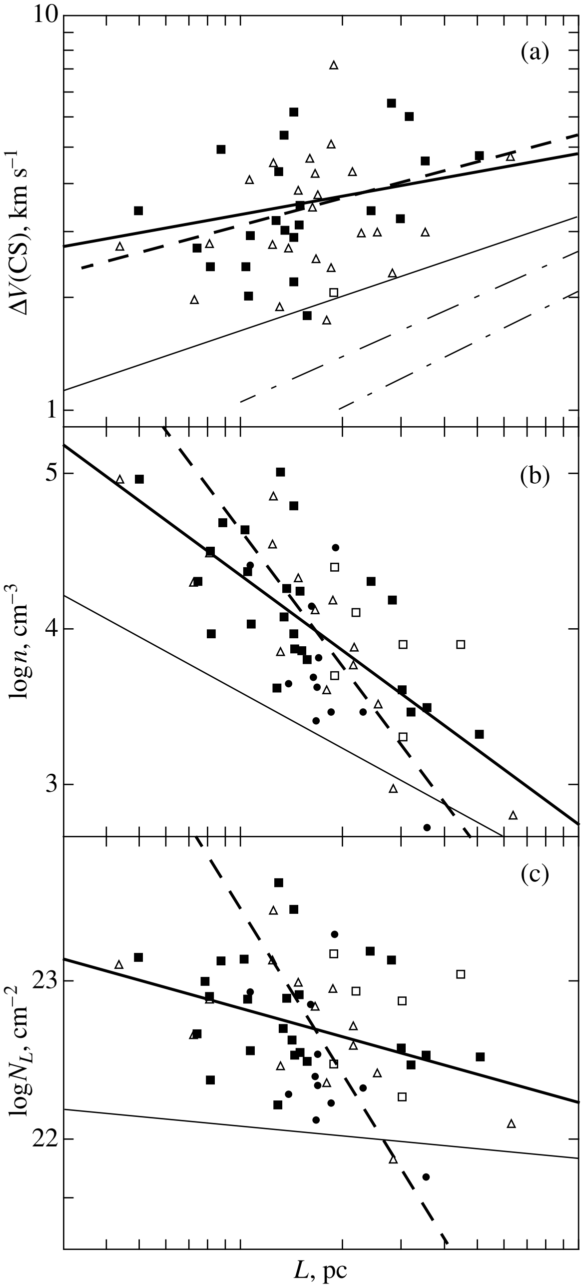

Fig. 1. (a) CS line widths, (b) mean densities, and (c) hydrogen column densities versus size for the sources observed with SEST (filled squares), OSO (triangles and dots for the data obtained from $C^{34}S$ column densities and virial masses, respectively), and Metsahovi (open squares) radio telescopes. The heavy solid and dashed lines correspond to the ordinary and orthogonal least-squares methods, respectively. The thin solid lines correspond to the $J = 1$–0 ^{13}CO observations. The dash–dotted lines correspond to the ^{13}CO (Larcon 1981), CS, and NH_3 [upper for cores with embedded stars, and lower for cores without stars (Fuller and Myers 1992)] observations of dark-cloud cores.

commonly obtained relation $n \propto L^{-1}$ may well be the result of selection by column density.

Our data are not free from selection effects either. In particular, if we construct the mass–distance relation, we see that only massive cores are observed at large distances ($d \gtrsim 4$ kpc). By contrast, cores of relatively low mass dominate nearby ($d \lesssim 1$ kpc). There is also a similar selection by size. How can these effects affect the detected correlations? The selection by mass and size mentioned above apparently cannot distort them seriously. As a result of this, we will have many (or few) disproportionate data points in one part of the plot, but the pattern of relations will not change significantly.

The slope of our L–n relation cannot be explained by possible selection by column density either, which, as was pointed out above, results in a relation of the form $n \propto L^{-1}$. In general, the fact that CS emission was detected virtually in all directions rules out any substantial selection of this kind.

The next important question is as follows: How can the adopted technique for determining cloud parameters affect the results? In particular, we estimated the sizes from the solid angles of sources. This is one of the standard approaches. Another commonly used approach is to determine the size at half intensity $L_{0.5}$. It should be noted that the ratio of these sizes depends on the brightness distribution over the source, which, in turn, is determined by the density and temperature distributions. For a Gaussian brightness distribution, L is the size at e^{-1} of the maximum. It is related to the half-intensity size by $L = L_{0.5}/\sqrt{\ln 2}$. In other cases, the ratio of these sizes can differ, but only slightly.

To find out how our results depend on size determination, we also computed half-intensity sizes virtually for all objects of our sample. The correlations between $L_{0.5}$, line width, and mean density essentially match those given above. Thus, our correlations are clearly not the result of selection effects or of the measurement technique, but reflect the physical realities.

The L–ΔV and L–n relations for clouds in virial equilibrium [this condition is satisfied for the objects under consideration, as we showed previously (Zinchenko 1995; Zinchenko *et al.* 1998) are linked via the virial equation (2). The question arises as to which of them is "primary".

A number of authors (e.g., Caselli and Myers 1995; McLaughlin and Pudritz 1996) derived relations between ΔV and L similar to those obtained here either by assuming a peculiar equation of state of the gas ("logotropic" model) or by using a model combining in a certain way thermal and nonthermal motions (TNT model). However, in these models, the velocity dispersion in a specific cloud increases with distance from the center. Our data (Zinchenko 1995; Zinchenko *et al.* 1997) most likely imply an inverse radial dependence of the velocity dispersion.

The L–n relation can be assumed to be primary. In this case, the following must be borne in mind: (i) the gas column density decreases with increasing size, and (ii) the gas density in line formation regions is more or less constant and exceeds considerably the mean density. It thus follows that the variations in mean density and cloud size are mostly determined by variations in the factor of volume filling by emitting clumps and by the rate of decrease in density toward the cloud edge. More extended clouds must have smaller filling factors and smoother radial density-decrease laws. What we see may be a manifestation of the evolution of the objects under study: from extended tenuous clouds to compact clumps.

According to CS observations, the velocity dispersions in massive cores are larger in absolute value than those in CO clouds and dense cores in dark nebulae. This is consistent with our previous results in HCN and HCO^+ lines (Zinchenko 1992; Pirogov and Zinchenko 1998). Similar results were also obtained during a CS $J = 1$–0 survey of the dense cores in Orion *A* (Tatematsu *et al.* 1993) and by Plume *et al.* (1997). Some models link the velocity dispersion with an external pressure on the cloud (e.g., Elmegreen l989). In these models, the above discrepancies can be explained by a higher external pressure on the cores under study, which can be produced, for example, by tenuous shells.

CONCLUSION

We have analyzed the correlations between line width and size (ΔV–L), as well as between mean density and size (n–L), by using a CS and $C^{34}S$ survey of dense molecular-cloud cores in regions of high-mass-star formation. There is virtually no correlation between ΔV and L ($\Delta V \propto L^{0.2 \pm 0.1}$). The velocity dispersions are several times higher in absolute value than those in CO clouds and dark nebulae of the same size. The mean density decreases with increasing size faster than L^{-1}, so the column density also decreases with increasing core size. These results could not have been affected significantly by possible selection effects. So far it seems impossible to unambiguously answer the question of why these correlations appear. They may reflect the evolution of dense clouds.

ACKNOWLEDGMENTS

I am grateful to L.E. Pirogov for his assistance and to the referee for helpful comments. This study was supported by the Russian Foundation for Basic Research (project nos. 96-02-16 472 and 99-02-16 556) and the INTAS Foundation (grant no. 93-2168-ext).

REFERENCES

1. P. Caselli and P. C. Myers, Astrophys. J. **446**, 665 (1995).
2. B. G. Elmegreen, Astrophys. J. **338**, 178 (1989).
3. E. D. Feigelson and G. J. Babu, Astrophys. J. **397**, 55 (1992).
4. G. A. Fuller and P. C. Myers, Astrophys. J. **384**, 523 (1992).
5. A. A. Goodman, J. A. Barranco, D. J. Wilner, and M. H. Heyer, Astrophys. J. **504**, 223 (1998).
6. W. M. Irvine, P. F. Goldsmith, and A. Hjalmarson, in *Interstellar Processes*, Ed. by D. L. Hollenbach and H. A. Thronson, Jr. (Reidel, Dordrecht, 1987), p. 561.
7. W. H. Kegel, Astron. Astrophys. **225**, 517 (1989).
8. R. B. Larcon, Mon. Not. R. Astron. Soc. **194**, 809 (1981).
9. D. E. McLaughlin and R. E. Pudritz, Astrophys. J. **469**, 194 (1996).
10. P. C. Myers, in *Protostars and Planets II*, Ed. by D. C. Black and M. S. Matthewes (Univ. Arizona Press, Tucson, 1985), p. 81.
11. L. E. Pirogov and I. I. Zinchenko, Astron. Zh. **75**, 14 (1998) [Astron. Rep. **42**, 11 (1998)].
12. L. E. Pirogov, I. I. Zinchenko, A. V. Lapinov, *et al.*, Astron. Astrophys., Suppl. Ser. **109**, 333 (1995).
13. R. Plume, D. T. Jaffe, N. J. Evans II, *et al.*, Astrophys. J. **476**, 730 (1997).
14. K. Tatematsu, T. Umemoto, O. Kameya, *et al.*, Astrophys. J. **404**, 643 (1993).
15. I. I. Zinchenko, Astron. Astrophys. Trans. **1**, 253 (1992).
16. I. Zinchenko, Astron. Astrophys. **303**, 554 (1995).
17. I. I. Zinchenko, A. V. Lapinov, and L. E. Pirogov, Astron. Zh. **66**, 1142 (1989) [Sov. Astron. **33**, 590 (1989)].
18. I. Zinchenko, V. Forsstroem, A. Lapinov, and K. Mattila, Astron. Astrophys. **288**, 601 (1994).
19. I. Zinchenko, K. Mattila, and M. Toriseva, Astron. Astrophys., Suppl. Ser. **111**, 95 (1995).
20. I. Zinchenko, Th. Henning, and K. Schreyer, Astron. Astrophys., Suppl. Ser. **124**, 385 (1997).
21. I. Zinchenko, L. Pirogov, and M. Toriseva, Astron. Astrophys., Suppl. Ser. **133**, 337 (1998).

Translated by V. Astakhov

Astronomy Letters, Vol. 26, No. 12, 2000, pp. 806–808. Translated from Pis'ma v Astronomicheskiĭ Zhurnal, Vol. 26, No. 12, 2000, pp. 938–941.
Original Russian Text Copyright © 2000 by Bekaryan, Melkonyan.

Investigation of Dynamical Chaotization in Stellar Systems with Double Massive Centers Using the Ricci Curvature Criterion

K. M. Bekaryan[1] and A. A. Melkonyan[2]

[1] *Yerevan State University, ul. A. Manukyana 1, Yerevan, 375049 Armenia*
[2] *Yerevan Physical Institute, Yerevan, Armenia*

Received May 27, 1999; in final form, April 20, 2000

Abstract—The Ricci curvature criterion is used to investigate the relative instability of various configurations of *N*-body gravitational systems. Systems with double massive centers are shown to be less stable than homogeneous systems or systems with single massive centers. In general, this is a confirmation that the Ricci curvature criterion is efficient in studying *N*-body systems by means of relatively simple computations. *© 2000 MAIK "Nauka/Interperiodica".*

Key words: *dynamical instability of gravitating systems*

1. INTRODUCTION

The interest in the dynamics of systems with double massive centers stems from the discovery of double nuclei at the centers of some galaxies with projected component separations from 2 pc (M 31) to 800 pc (Markarian 273); a massive double object was also discovered at the center of Arp 220 (Baan and Haschil 1995). Massive double objects in the central parts of galaxies may be responsible for a number of dynamical effects.

We used the Ricci curvature criterion, which was introduced by Gurzadyan and Kocharyan (1987) to analyze the relative instability (chaos) of *N*-body systems, to investigate the effect of a massive central double object on the dynamical instability of gravitational systems. In particular, using this method, Gurzadyan and Kocharyan (1988) established that a regular central field makes the *N*-body systems more unstable. Remarkably, this result was established by numerically analyzing a system with a moderate number of bodies and was subsequently confirmed by extended simulations with more powerful computers (El Zant and Gurzadyan 1998). The effect of a central regular field is crucial in understanding the relaxation, mixing, and evolution of galactic nuclei. Here, we explore the question of how a double center, i.e., a massive double object at the center of an *N*-body system, affects the system's instability. The situation is complex in that there are both types of effects, causing both an increase and decrease in the degree of chaos in the system.

Note that there is a wide range of methods for investigating the instability of *N*-body systems: from computing the Lyapunov characteristic indices and the Kolmogorov–Sinay entropy and successive iterations to methods based on exact solutions (Gerald and Wheatley 1994; Aarseth 1985, 1994; Lichtenberg and Lieberman 1983). The efficiency of each of these methods generally depends on the objectives of a particular task, so, in many respects, selecting numerical methods is of crucial importance. Thus, for example, when the Lyapunov indices are computed, the errors increase exponentially with time.

Geometric methods based on theorems of the theory of dynamical systems provide rich possibilities for studying *N*-body systems by reducing the problem to investigating the geometric properties of the system's phase and configuration spaces (Arnold 1979). Krylov (1950) and Gurzadyan and Savvidi (1984, 1986) were the first to apply this method to physical problems and *N*-body gravitational systems, respectively. The latter authors showed that spherical systems are *K*-systems, i.e., those with mixing and exponential instability.

Statistical properties play a key role in understanding the relaxation and evolutionary effects in many astrophysical systems, ranging from the Solar system to clusters of galaxies.

2. NUMERICAL SIMULATIONS

As was pointed out above, we used the Ricci curvature criterion (Gurzadyan and Kocharyan 1987) to study the relative instability of dynamical systems. In essence, this criterion involves determining the sign and magnitude of the Ricci curvature. A system is con-

---

* E-mail address for contacts: bekar@uniphi.yerphi.am

sidered to be more unstable relative to another system if its Ricci curvature is negative and larger in magnitude.

In our numerical simulations, we determined the Ricci curvature of various N-dimensional configurations; i.e., we traced the time dependence of the Ricci curvature. The Ricci curvature for an N-body system was computed by using the following formulas (Gurzadyan and Kocharyan 1987, 1994; Gurzadyan and Pfenniger 1994):

$$r_u(s) = -\frac{(3N-2)}{2}\frac{W_{ik}u^i u^k}{W} + \frac{3}{4}(3N-2)\frac{(W_i u^i)^2}{W^2} - \frac{(3N-4)}{4}\frac{|\nabla W|^2}{W^3},$$

where

$$W = E - V; \quad V = -G\sum_{i<k}\frac{m_i m_k}{r_{ik}};$$

$$W_i = \frac{\delta W}{\partial q_i}; \quad W_{ik} = \frac{\partial^2 W}{\delta q_i \delta q_k};$$

$$\Delta W = \sum_i W_{ii}; \quad |\nabla W|^2 = \sum_i \left(\frac{\delta W}{\delta q_i}\right)^2.$$

We studied different configurations of systems with $N = 22$ using the scheme described by Gurzadyan and Kocharyan (1987); i.e., we considered systems with bodies uniformly located at the vertices and edges of two concentric cubes. The body velocities were chosen in such a way that the system's angular momentum was zero.

We determined the change in Ricci curvature with time t (in units of dynamical time τ) for the following configurations (Figs. 1–4):

(1) Homogeneous systems, i.e., all bodies have the same mass m;

(2) Systems with a central massive body m_1, while the remaining N–1 bodies have the same masses $m \ll m_1$;

(3) Systems with two central massive bodies m_1 and m_2, with the remaining N–2 remaining bodies having the same masses $m \ll m_1, m_2$.

Numerous computations (see Fig. 3) indicate that systems with a single central mass are more unstable than homogeneous systems, confirming the previous results (Gurzadyan and Kocharyan 1987, 1988; El Zant 1997; El Zant and Gurzadyan 1998). Note that systems become more unstable as the central mass increases.

Figure 1 illustrates the relative instability of the three types of systems for $m_1 = 10$. Systems with double massive centers are most unstable. Note that, although the Ricci curvature tends to zero for all three systems, this rate is at a maximum for systems with double massive centers. It is physically clear that systems of the third type must break up faster for a small number of bodies. It is this tendency that was revealed by our numerical simulations: the Ricci curvature tends to zero more slowly with increasing number of bodies. In other words, double massive centers make the systems initially more unstable, but such systems reach the final regular state faster.

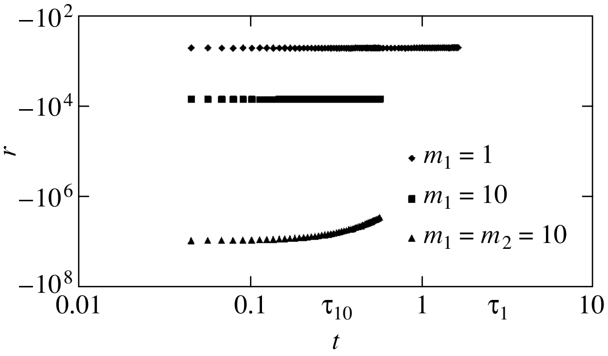

Fig. 1. Relative instability of three types of systems : homogeneous ($m_i = 1$); a central body with $m_1 = 10$ and the remaining N–1 bodies of unit mass; two central bodies with masses $m_1 = 10$ and $m_2 = 10$ and the remaining N–2 bodies of unit mass.

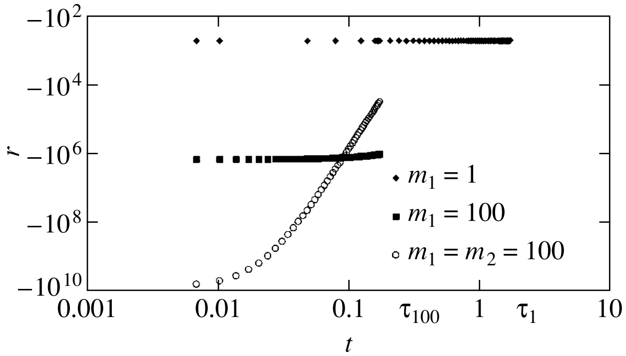

Fig. 2. Relative instability of systems: homogeneous; with $m_1 = 100$; and with $m_1 = 100$ and $m_2 = 100$.

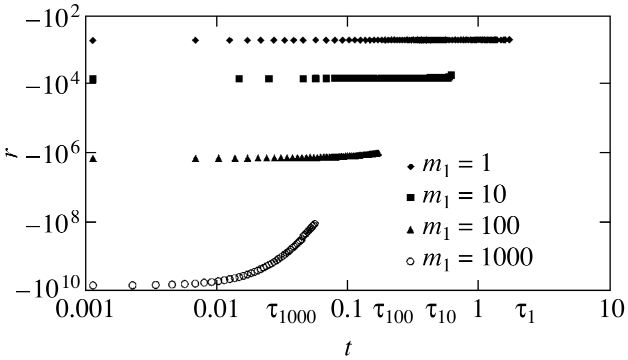

Fig. 3. Relative instability of the systems with a single massive center.

Figure 2 shows the results of our computations for $m_1 = 100$. Figure 4 shows how the Ricci curvature

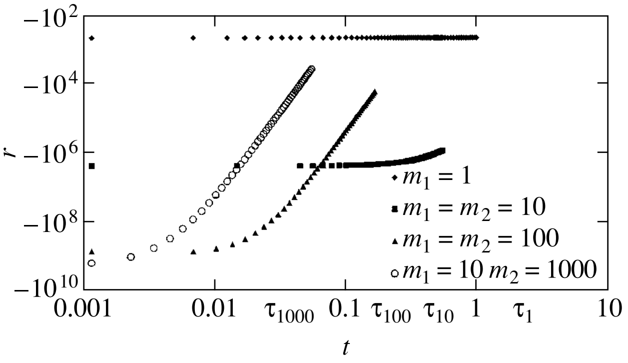

Fig. 4. Degree of instability versus mass of the central double object.

depends on the mass of a central double object. The tendencies shown in the figures were observed during our numerical simulations with a variety of initial conditions.

3. CONCLUSION

We have used the Ricci curvature criterion to study the relative instability of three types of *N*-body systems: homogeneous systems, systems with a single massive center, and systems with a double massive center. Our numerical simulations have led us to the following conclusions.

(1) The presence of a second central mass makes the systems more unstable relative to the two systems mentioned above.

(2) Systems with binary massive centers approach the regular state faster.

(3) The larger the mass ratio of the central objects and the remaining bodies, the greater the difference in the initial instability and in the rate of evolution.

Our main conclusion is that the Ricci curvature criterion is efficient in studying complex multidimensional systems, such as *N*-body systems, using rather simple numerical simulations.

ACKNOWLEDGMENTS

We are grateful to Prof. V.G. Gurzadyan for his useful discussions and valuable remarks and to S. Aarseth for a discussion of *N*-body algorithms. This work was supported in part by the INTAS (grant no. 93-2032).

REFERENCES

1. S. J. Aarseth, in *Multiple Time Scales*, Ed. by J. U. Brackbill and B. Cohen (Academic, New York, 1985).
2. S. J. Aarseth, in *Galactic Dynamics and N-Body Simulations*, Ed. by G. Contopoulos, N. K. Spyrou, and L. Vlahos (Springer-Verlag, New York, 1994).
3. V. I. Arnold, *Mathematical Methods of Classical Mechanics* (Nauka, Moscow, 1979; Springer-Verlag, New York, 1989).
4. W. A. Baan and A. D. Haschick, Astrophys. J. **454**, 745 (1995).
5. A. A. El-Zant, Astron. Astrophys. **326**, 113 (1997).
6. A. A. El-Zant and V. G. Gurzadyan, Physica D **122**, 241 (1998).
7. C. F. Gerald and P. O. Wheatley, *Applied Numerical Analysis* (Addison-Wesley, New York, 1994).
8. V. G. Gurzadyan and G. K. Savvidy, Dokl. Akad. Nauk SSSR **277**, 69 (1984) [Sov. Phys. Dokl. **29**, 520 (1984)].
9. V. G. Gurzadyan and G. K. Savvidy, Astron. Astrophys. **160**, 203 (1986).
10. V. G. Gurzadyan and A. A. Kocharyan, Astrophys. Space Sci. **135**, 307 (1987).
11. V. G. Gurzadyan and A. A. Kocharyan, Dokl. Akad. Nauk SSSR **301**, 323 (1988) [Sov. Phys. Dokl. **33**, 494 (1988)].
12. V. G. Gurzadyan and A. A. Kocharyan, *Paradigms of the Large-Scale Universe* (Gordon and Breach, New York, 1994).
13. V. G. Gurzadyan and D. Pfenniger, *Ergodic Concepts in Stellar Dynamics* (Springer-Verlag, New York, 1994).
14. N. S. Krylov, *Basing Works of Statistical Physics* (Akad. Nauk SSSR, Moscow, 1950).
15. A. J. Lichtenberg and M. A. Lieberman, *Regular and Stochastic Motion* (Springer-Verlag, New York, 1983).

Translated by A. Dambis

Astronomy Letters, Vol. 26, No. 12, 2000, pp. 809–820. Translated from Pis'ma v Astronomicheskiĭ Zhurnal, Vol. 26, No. 12, 2000, pp. 942–953.

Effects of Data Incompleteness on the Results of Fourier Analysis of Line-of-Sight Velocity Fields in Spiral-Galaxy Disks

A. N. Burlak[1, 2], A. V. Zasov[1], A. M. Fridman[2, 1], and O. V. Khoruzhiĭ[3, 2]*

[1] *Sternberg Astronomical Institute, Universitetskiĭ pr. 13, Moscow, 119899 Russia*
[2] *Institute of Astronomy, Russian Academy of Sciences, ul. Pyatnitskaya 48, Moscow, 109017 Russia*
[3] *Troitsk Institute for Innovation and Thermonuclear Research, Troitsk, Moscow oblast, 142092 Russia*

Received July 21, 2000

Abstract—Our main goal is to investigate the effects of data incompleteness on the results of Fourier analysis of line-of-sight velocity fields in the disks of spiral galaxies. We have carried out a number of numerical experiments, first with an artificially created simple velocity field and then with the velocity fields of two real galaxies, which qualitatively differ in data filling: NGC 157 and NGC 3631 with good and bad data filling, respectively. The field of purely circular velocities is chosen as the simplest artificial velocity field, because the circular velocities of spiral galaxies are much high than the residual (noncircular) velocities. Superimposing a "mask" simulating blank spots (holes) in the map of observational data on this artificial field has no effect on the results of Fourier analysis of this simplest field. A similar result is obtained for real galaxies with good data filling of the observed velocity fields. Superimposing arbitrarily shaped masks on the observed velocity field of NGC 157 in such a way that the field was filled by a mere 50% (at each radius) could not change appreciably the radial variations of large-scale Fourier harmonics. The situation qualitatively changes in attempting to fill the holes in the observed velocity field of NGC 3631 in some way. When missing velocities are artificially introduced by using the simplest model of purely circular gas rotation, the amplitudes and phases of the principal Fourier harmonics are distorted. In particular, a substantial distortion of the third harmonic also causes an increase in the error when determining the corotation radius from data of the filled field. When the filling of the velocity field is increased by degrading the spatial resolution, the amplitudes of most harmonics decrease throughout the entire disk region; as a result, their radial variations are smoothed out and the behavior of harmonic phases in the range of moderately high initial amplitudes can be distorted. An abnormal enhancement of the highest Fourier harmonics in the regions of low filling of the initial field is also possible. At the same time, despite the above distortions, the corotation radius determined from the smoothed fields matches that for the initial velocity fields. © *2000 MAIK "Nauka/Interperiodica".*

Key words: *spiral galaxies, Fourier analysis of line-of-sight velocities*

1. INTRODUCTION

The recently appeared possibilities for measuring gas line-of-sight velocities in the optical and radio spectral ranges for thousands of points in galactic disks opened up new prospects for investigating large-scale gas motions. An analysis of the velocity field based on the extraction of Fourier harmonics in the azimuthal distribution of gas line-of-sight velocities at various galactocentric distances allow us not only to refine the disk orientation and inclination and the shape of the galaxy rotation curve, but also to reveal systematic deviations from circular gas motion attributable to the large-scale density waves associated with the spiral pattern, as well as to estimate parameters of these waves and to construct a model for the three-dimensional vector residual velocity field (Lyakhovich *et al.* 1997; Fridman *et al.* 1997, 1998, 2000). To perform a Fourier analysis, the disk is broken down into circular (corrected for disk inclination) concentric rings. A certain galactocentric distance r is assigned to each ring, and a dependence of the measured velocity on azimuthal angle φ is sought for each ring in the form of a Fourier series:

$$V_{\rm rad}(r,\varphi) = \sum_{0}^{m}[a_k(r)\cos(k\varphi) + b_k(r)\sin(k\varphi)] + \xi, \qquad (1)$$

where $m \simeq 10$ and ξ is a random deviation. In accordance with our Grand-Design model (Lyakhovich *et al.* 1997; Fridman *et al.* 1997, 1998, and 2000), a correspondence can be established between the large-scale behavior of individual gas velocity components in galaxies and the lowest Fourier harmonics. In this case, it is important that the agreement between specific observational data and the model can be verified by several independent methods (Lyakhovich *et al.* 1997; Fridman *et al.* 1997, 1998, 2000).

---

* E-mail address for contacts: okhor@inasan.rssi.ru

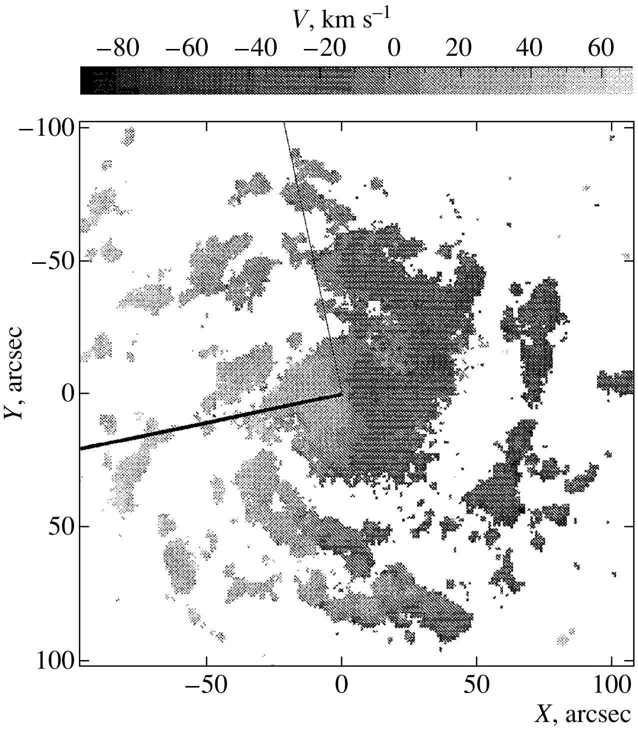

Fig. 1. The original line-of-sight velocity field of NGC 3631 obtained with the 6-m Special Astrophysical Observatory telescope (Fridman *et al.* 1998). Since holes in observations are grouped in the interarm spaces, the field looks like a two-armed spiral.

If velocity measurements cover the entire disk, no difficulties arise when computing Fourier harmonics. However, the velocity field is often filled incompletely: there are holes in which line-of-sight velocity data are lacking. The situation is compounded by the fact that it is not uncommon for holes to form something of a spiral pattern concentrating toward the interarm spaces rather than being arranged chaotically. This implies that the data incompleteness can be not only random in nature, but can also exhibit some azimuthal periodicity associated with the spiral pattern.

We face a similar problem in optical observations when analyzing time series. In this case, daytime holes in observations are arranged periodically, in contrast to “random holes” caused, say, by bad weather. In his book devoted to an analysis of time series, Terebizh (1992) showed that, in general, data sampling could give rise to spurious maxima in the power spectrum of the signal under study; theoretical studies based on observational data are used to clean them out. Here, we compare several methods of computing Fourier spectra for line-of-sight velocity fields in galaxies with spatial data incompleteness attributable to weak emission lines in some galactic-disk regions. As at daytime, when there are no observations, we do not assume peculiarities in the stellar variability that are inconsistent with the theory of its evolution based on nighttime observations, nor do we assume any peculiarities inconsistent with the dynamical theory of gaseous disks based on extensive observational data in the holes of the velocity fields of gaseous disks. The absence of real holes in a literal sense in weak emission line regions is also corroborated by galaxy observations in other wavelength ranges: radio and infrared. As a rule, the holes seen in optical emission-line images are absent in radio and infrared galaxy images.

We can imagine holes in the observed velocity field as the result of observing the galaxy through a mask covering certain disk regions where the velocities remain unmeasured. The mask can be described as a map made up of points with indices 1 (line-of-sight velocity measurements available) and 0 (measurements unavailable). The Fourier spectrum of such a mask for a fully filled velocity field will contain only a zero harmonic with value 1. In general, the spectrum of an imaginary mask through which the velocity field is observed will have a complex shape dominated by certain harmonics. For example, if there is an m-armed spiral pattern in the galaxy, then the spectrum of the map will be dominated by the mth harmonic. Such a correlated incompleteness of the velocity field can be assumed to affect the results of Fourier analysis. However, the degree of influence of this factor is not clear in advance.

Here, our goal is to study the influence of holes in line-of-sight velocity fields on the results of Fourier analyses. One might expect the incompleteness effect to depend both on the total area of the holes and on the Fourier spectrum of their distribution. We therefore carried out the following numerical experiments:

—superimposing artificial masks of various geometries, including those describing holes in the observed velocity fields of spiral galaxies, on the velocity field corresponding to purely circular gas motion;

—superimposing artificial masks of various geometries and filling factors on the observed line-of-sight velocity field with initially good filling.

In addition, we analyzed two possible methods for suppressing the strong incompleteness effect in the velocity field:

—artificial filling of holes in the observed velocity field of a specific galaxy based on the simplest model of purely circular gas motion;

—blurring out holes by smoothing the observed velocity field or by degrading its spatial resolution.

As the input data for our experiments, we used published data on the line-of-sight velocity fields in the spiral galaxies NGC 157 and NGC 3631 (Fridman *et al.* 1997, 1998, 2000). These fields differ qualitatively in filling ratio. Whereas the velocity field of the former galaxy is essentially filled with measurements, much of the velocity field in the latter is covered with holes. These galaxies were observed in the Hα line with a scanning Fabry–Perot interferometer attached to the 6-m Special Astrophysical Observatory telescope. To compute the Fourier harmonics of the velocity field, we used the VORTEX code developed at the Institute of Astronomy

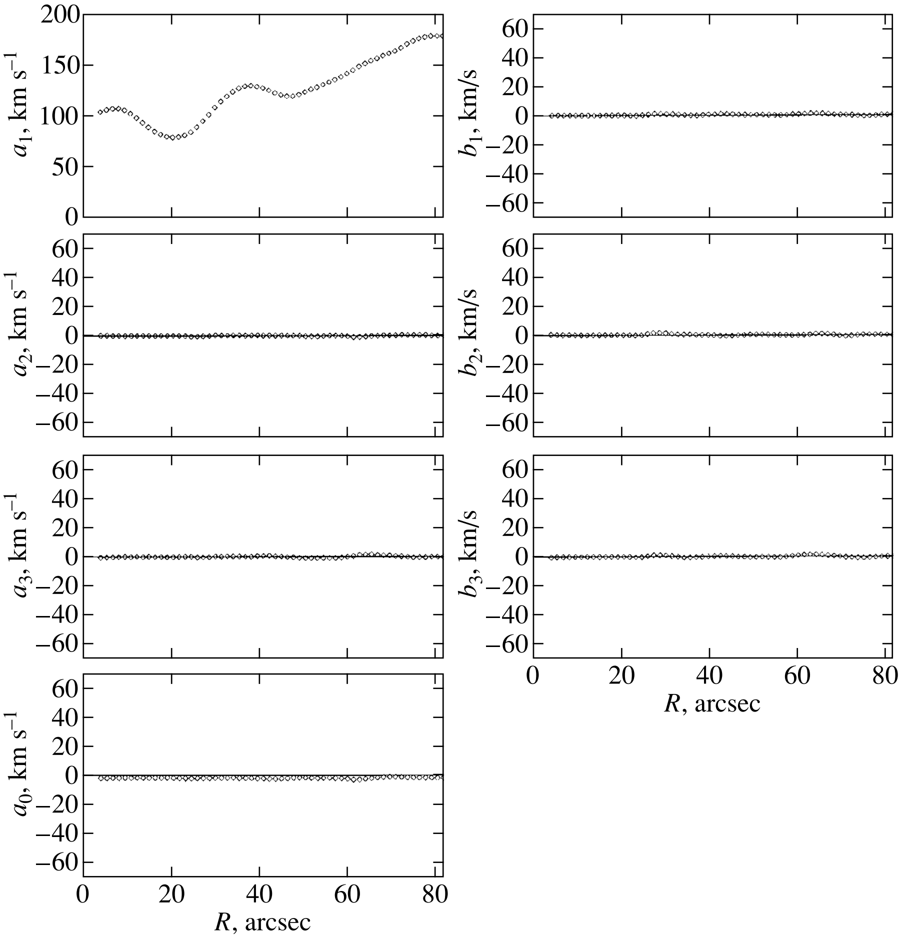

Fig. 2. Radial behavior of the principal Fourier harmonics for the line-of-sight velocity field of gas with purely circular motion. The disk orientation and the field filling reproduce the characteristics of the actual velocity field in NGC 3631.

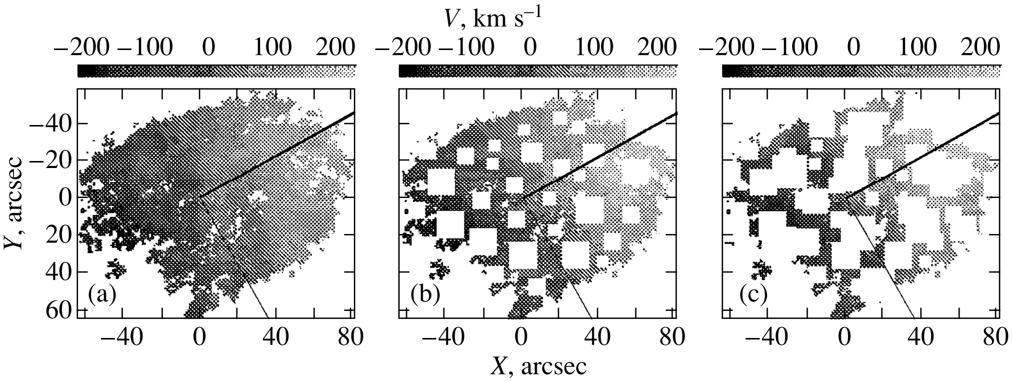

Fig. 3. (a) The original and (b), (c) masked velocity fields of NGC 157.

of the Russian Academy of Sciences (Lyakhovich *et al.* 1997). Observing conditions and data reduction were described by Fridman *et al.* (1997, 1998, 2000).

2. SUPERIMPOSING AN ARTIFICIAL MASK ON THE LINE-OF-SIGHT VELOCITY FIELD OF PURELY CIRCULAR GAS MOTION

To make sure that the mask by itself introduces no additional harmonics into the Fourier spectrum of the line-of-sight velocity field, we carried out several experiments on superimposing a mask on the velocity field of purely circular gas motion. The latter implies that, to each velocity-field pixel with galactocentric coordinates r and φ, we assigned the line-of-sight velocity $V_{\mathrm{mod}}(r)$ determined by the rotation velocity at a given radius $V_{\mathrm{rot}}(r)$ according to the following standard relation (see, e.g., Lyakhovich *et al.* 1997; Fridman *et al.* 1997):

$$V_{\mathrm{mod}}(r, \varphi) = V_{\mathrm{rot}}(r)\cos(\varphi)\sin i. \quad (2)$$

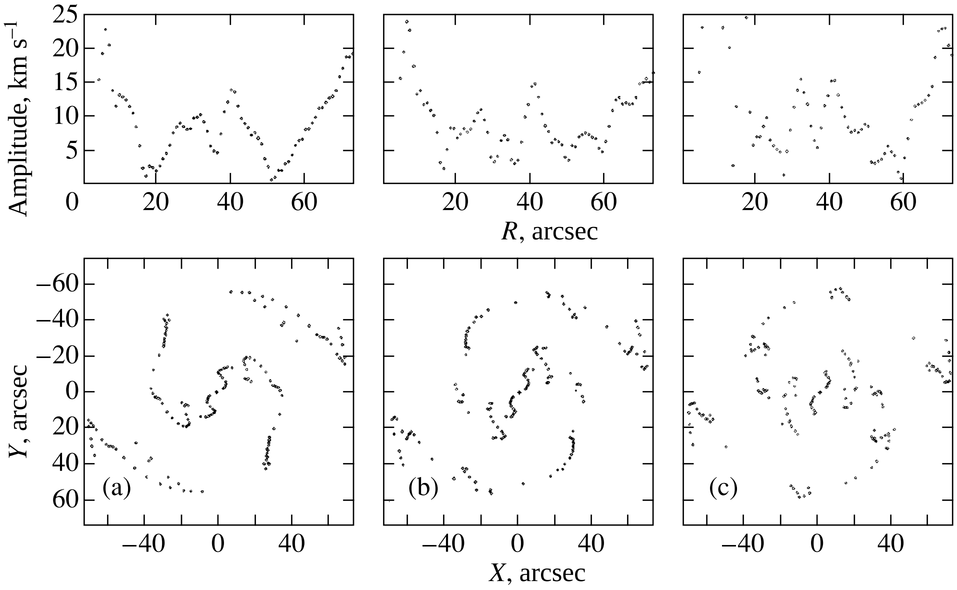

Fig. 4. Behavior of the amplitude (top) and the lines of maximum values of the second Fourier harmonic (bottom) calculated from (a) the original and (b), (c) masked velocity fields of NGC 157.

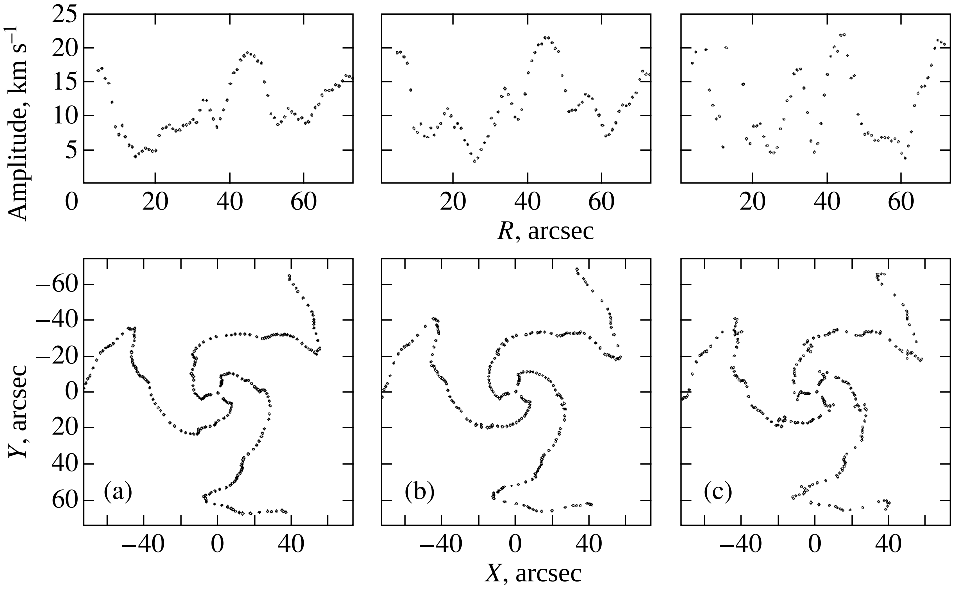

Fig. 5. Behavior of the amplitude (top) and the lines of maximum values of the third Fourier harmonic (bottom) calculated from (a) the original and (b), (c) masked velocity fields of NGC 157.

Here, i is the inclination of the galactic disk. In addition, we introduced small random deviations of the line-of-sight velocity from that calculated from (2) into each pixel. Below, our results are presented for the field generated by using the rotation curve of NGC 3631 (Fridman *et al.* 1998).

We first superimposed a mask whose shape corresponded to the observed line-of-sight velocity field of this galaxy (Fig. 1). By the definition of the mask in Section 1, this implies that we covered the areas for which no measurements were available in the real galaxy, i.e., we covered the holes. Figure 3 shows the results of our computations of Fourier harmonics for this case. We see from the figure that all amplitudes, starting from the amplitude of the sine of the first harmonic, are present only at a noise level; i.e., the mask introduces no artificial harmonics into the Fourier spectrum of the velocity field, although the observed velocity field in NGC 3631 has the shape of a two-armed clumpy spiral, implying that the superimposed mask contains a pronounced second harmonic.

We then superimposed "provocative" masks with pronounced first, second, and third harmonics on the constructed velocity field of purely circular motion. For the first and second harmonics of the mask, we varied the angle between the line of mask zero phase and the galaxy major axis. A total of several tens of experiments were carried out. Only in some exotic cases did the radial dependence of the harmonic amplitudes differ from that shown in Fig. 2. In particular, if no line-of-sight velocities are available in both quadrants along the galaxy minor axis (second harmonic) or in the disk half on one side of the major or minor axis (first harmonic), deviations from zero in the zero and second harmonics of the order of the velocity noise divided by the sine of the galaxy inclination to the line of sight appear in the Fourier spectrum.

Thus, our experiments show that the results of Fourier analysis are stable to changes in the mask shape, i.e., to the gap pattern in the observed velocity field.

3. SUPERIMPOSING AN ARTIFICIAL MASK ON A WELL-FILLED GALAXY VELOCITY FIELD

The above experiments used a galaxy model with purely circular gas motion. To check how data incompleteness affects the results in the presence of noncircular gas motions in galaxies, we superimposed artificial masks on the observed line-of-sight velocity field of NGC 157. The velocity field of this galaxy is well filled and exhibits pronounced Fourier harmonics in the azimuthal line-of-sight velocity distribution, which are produced, as can be shown, by the two-armed density wave observed in this galaxy (Fridman *et al.* 1997, 2000).

Our Fourier analysis with superimposed masks yielded results that qualitatively agreed with the original ones (i.e., without masks). The amplitude and the location of the zero-phase line of the first three harmonics remained unchanged, within the limits of the measurement errors, even when the masks covered much of the disk area. The corresponding examples are given in Figs. 3–6. Figure 3 shows the shape of the superimposed mask; Figs. 4 and 5 show the amplitude and the lines of maximum values of the second and third harmonics calculated from the masked field; and Fig. 6 shows the behavior of the $|b_3| - |b_1|$ curve, where b_1 and b_3 are the amplitudes of the sines of the first and third Fourier harmonics, respectively. In the method proposed by Lyakhovich *et al.* (1997), the latter curve is used to determine the position of the corotation radius: the corotation position corresponds to the change of sign of $|b_3| - |b_1|$ from minus to plus. As we see from the above examples, the results of our Fourier analysis were severely distorted only when the unmasked part of the disk decreased to 20–25%.

Our results show that the results of Fourier analysis of the line-of-sight velocity field are sensitive only slightly both to the filling factor and to the gap pattern. A filling factor of 50% (at each radius) is essentially enough for the radial variations of large-scale Fourier harmonics to be reliably determined.

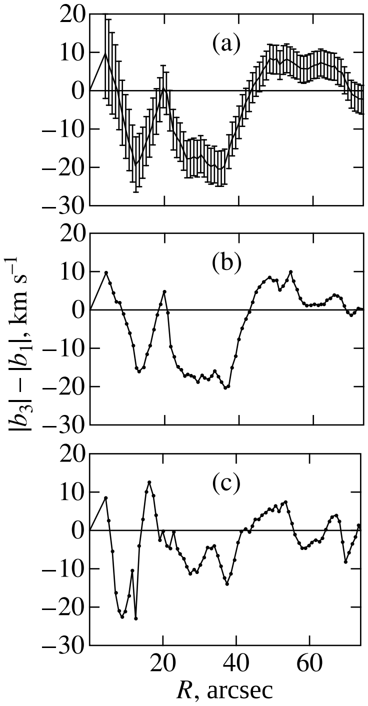

Fig. 6. Behavior of the function $|b_3| - |b_1|$, which is used to determine the position of the corotation radius (Lyakhovich *et al.* 1997; Fridman *et al.* 1997, 2000), calculated from (a) the original and (b), (c) masked velocity fields of NGC 157.

4. FILLING HOLES IN THE OBSERVED LINE-OF-SIGHT VELOCITY FIELD

Despite the stability of the results of Fourier analysis to incomplete filling of the galaxy disk with the observations shown above, it is of interest to discuss the potentialities of several most evident methods for suppressing holes in observations.

The simplest way out of the situation where there are holes in the velocity field seems to be their filling, i.e., an artificial introduction of missing velocities based on a particular model of gas motion. The simplest model requiring no additional data is the model of purely circular gas motion. In other words, we can try to fill the holes in the observed field with velocities that would be observed for purely circular gas motion at a given orientation of the galaxy disk. At first glance, this model makes sense, as the galactic disk is a disk precisely because its circular rotation velocity is much higher than the perturbed (or residual) velocities characterizing noncircular gas motions in the density wave.

We filled the holes in the velocity field of NGC 3631 by using the rotation curve computed from this field. In Figs. 7 and 8, the amplitudes of lower harmonics calculated, respectively, from the original and filled line-of-sight velocity fields of NGC 3631 are plotted against galactocentric radius. It is immediately apparent from a comparison of these figures that the harmonic amplitudes decreased after the holes were filled. This can be easily understood given that, in the case of circular rotation, the

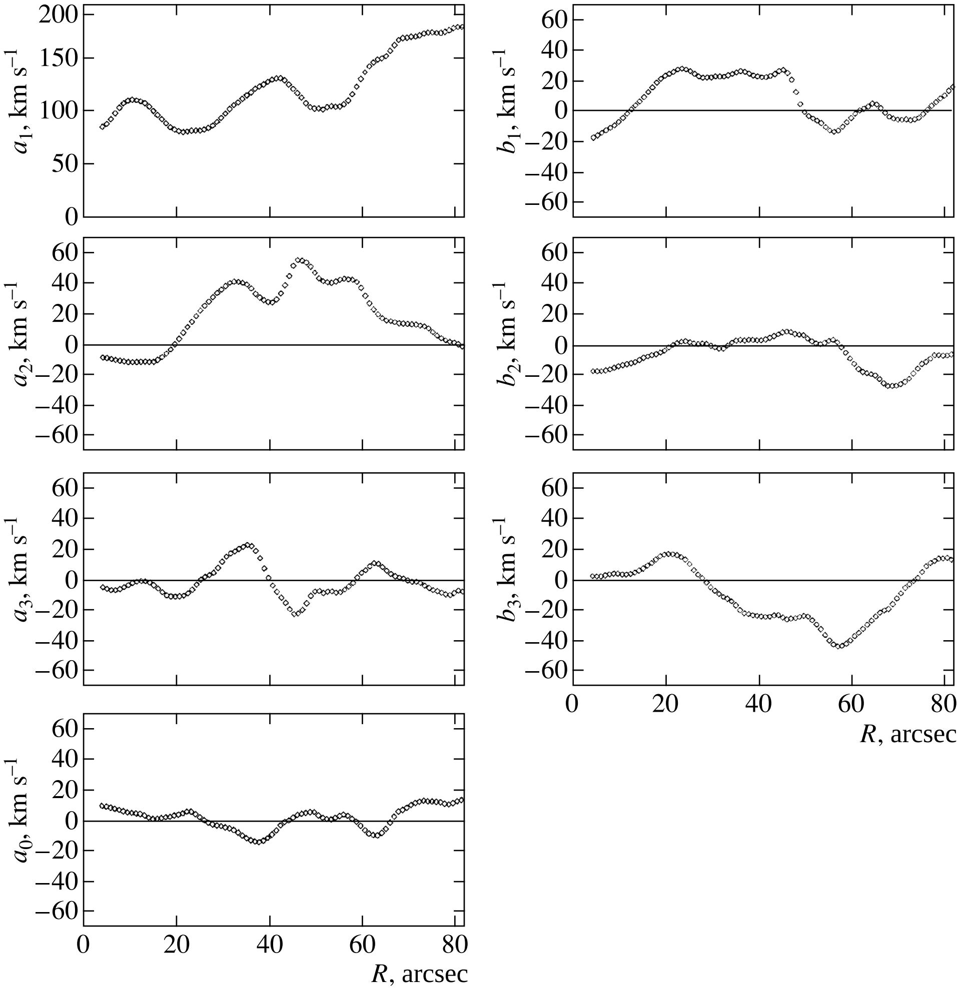

Fig. 7. Radial behavior of the principal Fourier harmonics in the original gas velocity field of NGC 3631.

amplitudes of all harmonics, except the amplitude of the cosine of the first harmonic, are zero. Therefore, filling holes is tantamount to assuming that there are no noncircular gas motions in these regions, which just corresponds to the lower amplitudes of the Fourier harmonics in general.

A more careful comparison of Figs. 7 and 8 clearly shows that filling the holes with purely circular motions causes not only a reduction in the radial dependence of harmonic amplitudes, but also in its distortion; the third Fourier harmonic is distorted most severely in this case. In support of this conclusion, Figs. 9 and 10 show the behavior of the amplitudes and the lines of maximum values of the second and third Fourier harmonics calculated from the (a) original and (b) filled velocity fields. We see that the distortions of the third harmonic are considerably more pronounced than those of the second harmonic: not only its amplitude decreases, but also the phase behavior in the outer region, where the fraction of holes is relatively large, changes qualitatively. This factor also causes the error in the position of the corotation radius inferred from the filled field to increase: we see from Fig. 11 that the zeros and extrema of the function $|b_3| - |b_1|$ are displaced.

The severe distortion of the third harmonic can be explained by taking into account the dominance of the second harmonic in the mask reflecting the velocity-field filling. The interference between the first harmonic describing circular rotation and the second harmonic in the form of artificially introduced additional points produces distortions primarily in the third harmonic of the velocity field “corrected” in this way. Interestingly, the same effect causes virtually no reduction in the amplitudes of higher Fourier harmonics of the filled field compared to the original field and artificial abnormally large amplitudes appear in some cases. For example, Fig. 12 shows the behavior of the amplitude and the lines of maximum values of the fifth Fourier harmonics for the (a) original and (b) filled velocity fields. We see that, after the holes were filled, an amplitude peak appeared at galactocentric distances of about 60″; it was so pronounced that the fifth harmonic artificially dominated in this region.

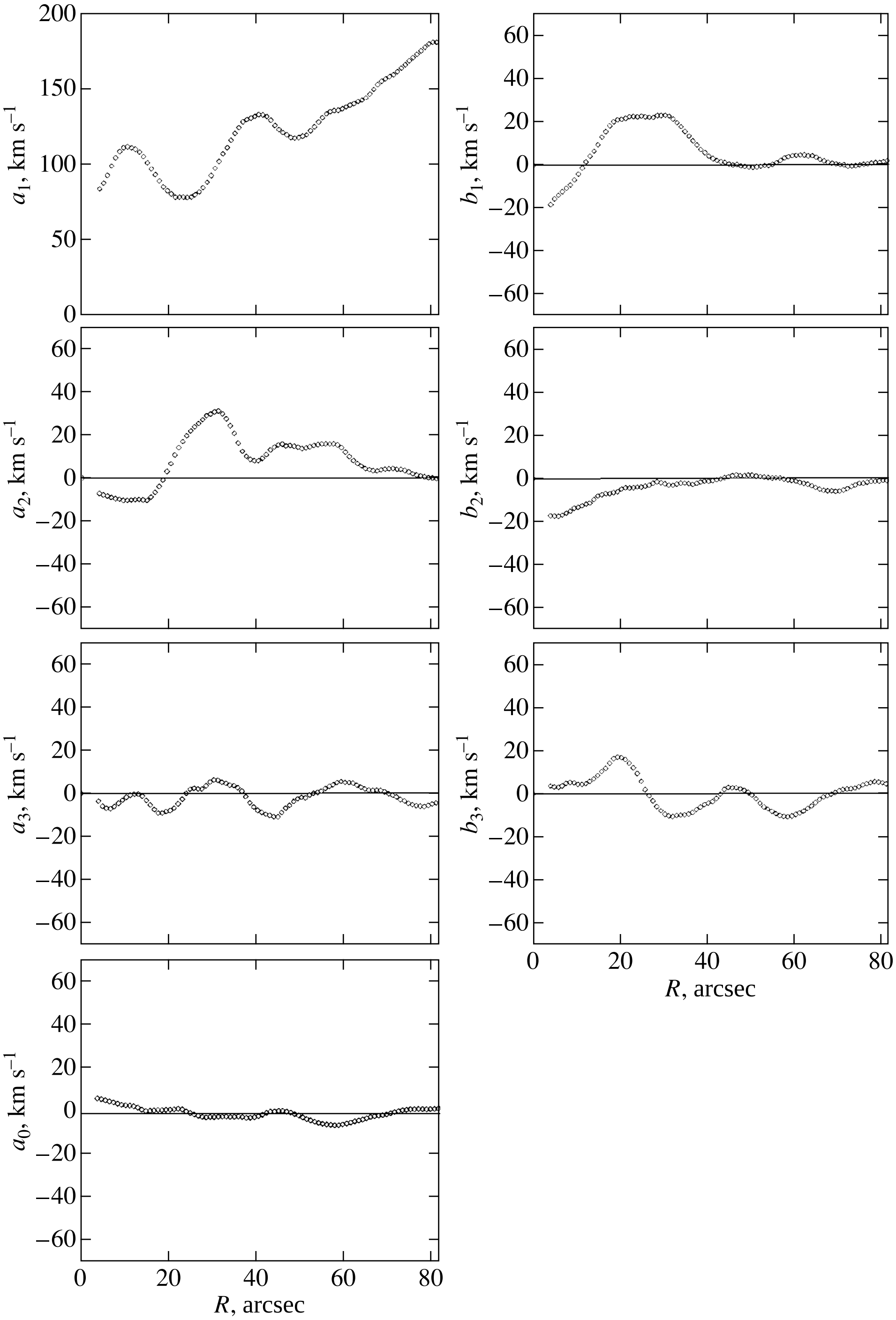

Fig. 8. Radial behavior of the principal Fourier harmonics in the gas line-of-sight velocity field constructed from the original field of NGC 3631 by filling holes in observations based on the model of purely circular gas motion.

Thus, filling holes in the observed line-of-sight velocity field based on the simplest model of purely circular gas motion cannot improve the quality of Fourier analysis. Rather, it distorts the radial behavior of the amplitudes and phases of the principal Fourier harmonics and, when there are holes of well-defined structure in the mask spectrum, can result in abnormally large amplitudes of higher Fourier harmonics. This makes the method of "correcting" poorly filled observed velocity fields totally unacceptable.

5. INCREASING THE FILLING FACTOR OF A VELOCITY FIELD BY DEGRADING THE SPATIAL RESOLUTION

Of special interest is the effect of angular resolution on Fourier harmonics. As the angular resolution is

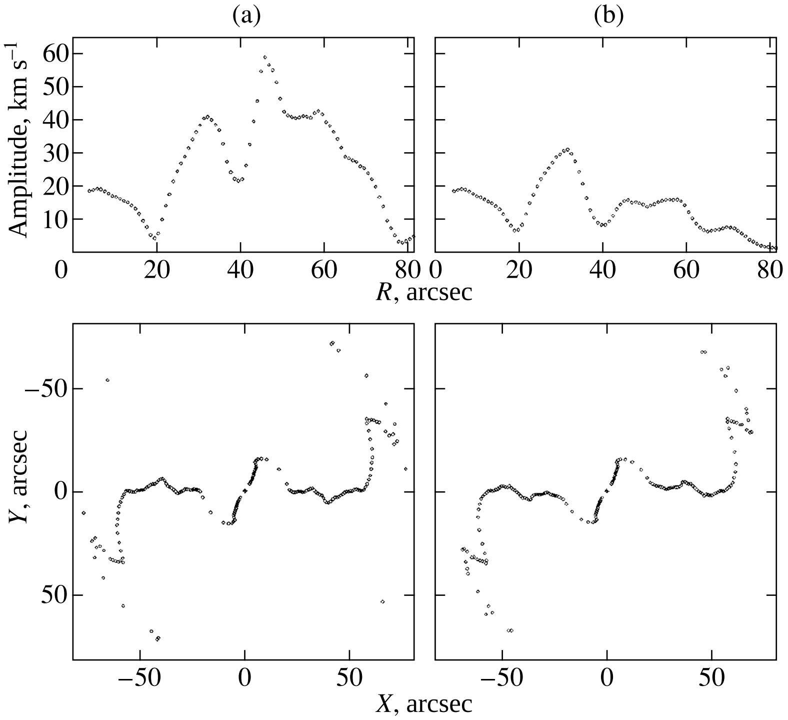

Fig. 9. Behavior of the amplitude (top) and the lines of maximum values of the second Fourier harmonic (bottom) calculated from (a) the original and (b) filled velocity fields of NGC 3631.

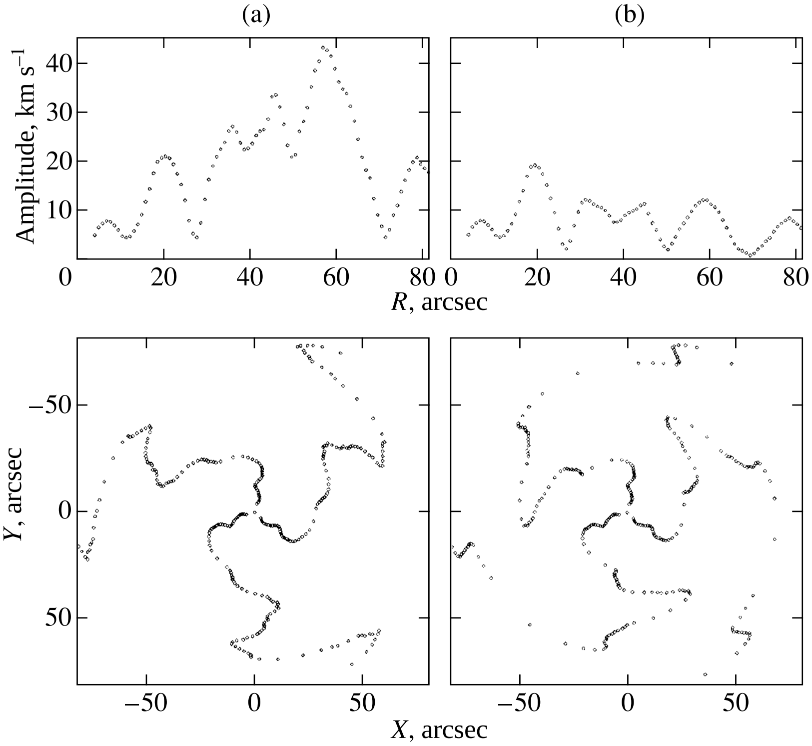

Fig. 10. Behavior of the amplitude (top) and the lines of maximum values of the third Fourier harmonic (bottom) calculated from (a) the original and (b) filled line-of-sight velocity fields of NGC 3631.

reduced, the holes in the velocity field are blurred and the filling factor increases for the same number of measurements in the galaxy disk. We studied the effect of resolution degradation on Fourier analysis by using the galaxies NGC 157 and NGC 3631 as examples. The velocity fields were obtained from the input observational data with a resolution several times lower than that of the original field (1 pixel = $0''.91$). The blurring

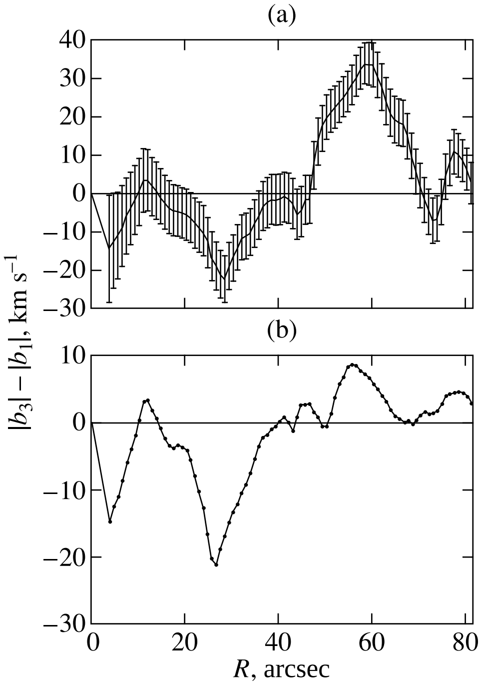

Fig. 11. Behavior of the function $|b_3| - |b_1|$ calculated from (a) the original and (b) filled velocity fields of NGC 3631.

was made by folding with a Gaussian of appropriate profile width.

Our computations of Fourier spectra for the constructed smoothed fields shows that, although degrading the spatial resolution leads to a better filling of the disk, it produces the following distortions in the radial dependence of the harmonic amplitudes and phases.

First, the amplitudes of most harmonics decrease throughout the entire disk region. This effect can be explained by taking into account the fact that the contributions of individual harmonics to the line-of-sight velocity change sign both in azimuth and in radius. As a result, when the resolution is degraded, the contributions of regions with opposite signs partially cancel each other out. Naturally, this suppression must be particularly strong near the center at galactocentric distances comparable to the resolution. Indeed, as we see from the figures given below, the amplitudes of all harmonics are nearly zero in the central region.

Second, the radial dependence of harmonic amplitudes is smoothed out. As a result, distortions are possible in the behavior of harmonic phases in the regions of (originally) low amplitudes. In support of this point, Figs. 13 and 14 show the behavior of the second and third harmonics calculated from the smoothed velocity fields of NGC 157 (cf. Figs. 4a and 5a) and NGC 3631 (cf. Figs. 9a and 10a), respectively.

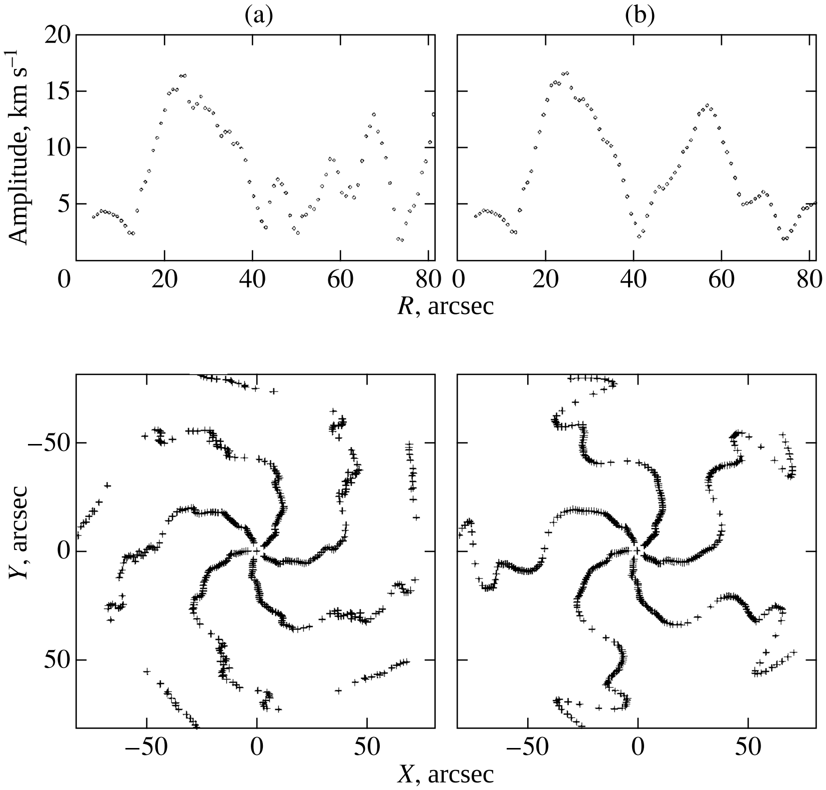

Fig. 12. Behavior of the amplitude (top) and the lines of maximum values of the fifth Fourier harmonic (bottom) calculated from (a) the original and (b) filled velocity fields of NGC 3631.

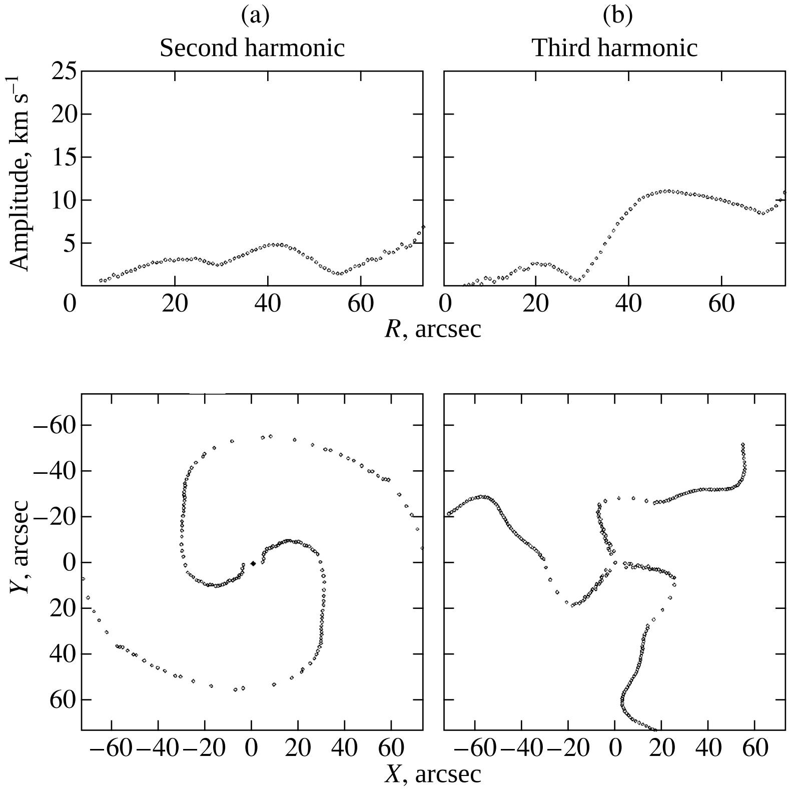

Fig. 13. Behavior of the amplitude (top) and the lines of maximum values (bottom) of (a) the second and (b) third Fourier harmonics calculated from the line-of-sight velocity field of NGC 157 smoothed by a Gaussian with a 9″.1 FWHM (cf. Figs. 4a and 5a, respectively).

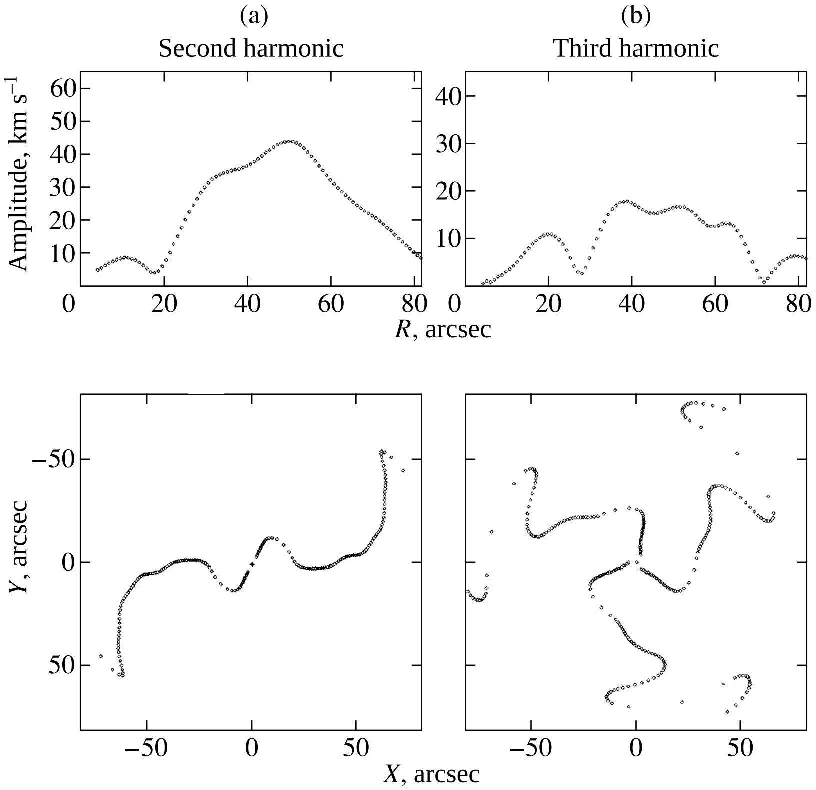

Fig. 14. Behavior of the amplitude (top) and the lines of maximum values (bottom) of (a) the second and (b) third Fourier harmonics calculated from the line-of-sight velocity field of NGC 3631 smoothed by a Gaussian with a 14″ FWHM (cf. Figs. 9a and 10a, respectively).

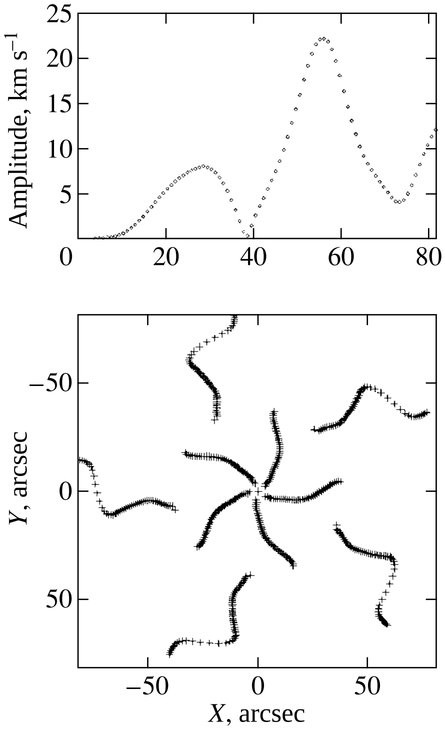

Fig. 15. Behavior of the amplitude (top) and the lines of maximum values (bottom) of the fifth Fourier harmonic calculated from the line-of-sight velocity field of NGC 3631 smoothed by a Gaussian with a 14″ FWHM (cf. Fig. 12a).

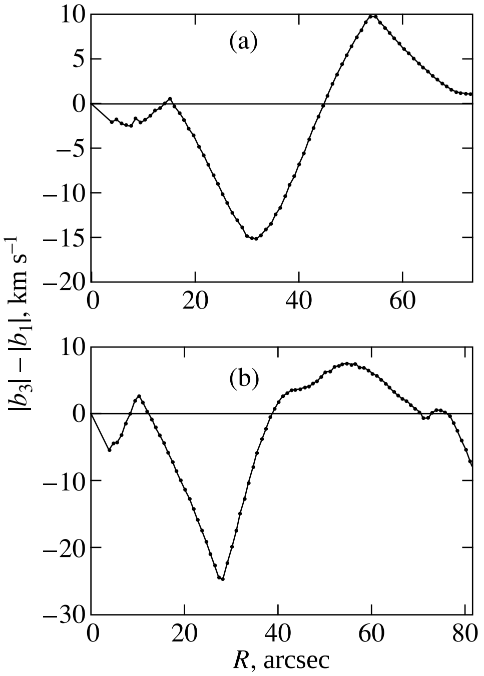

Fig. 16. Behavior of the function $|b_3| - |b_1|$ calculated from the smoothed fields of (a) NGC 157 and (b) NGC 3631 (cf. Figs. 6a and 11a, respectively).

Third, as in the case of gap filling based on the model of purely circular gas motion, the higher Fourier harmonics can be enhanced in poorly filled regions of the original field. For example, Fig. 15 shows the behavior of the parameters of the fifth Fourier harmonic in the smoothed velocity field of NGC 3631, demonstrating an abnormally high amplitude at 45″–60″ attributable solely to the smoothing (cf. Fig. 12a).

At the same time, despite the above distortions, the predicted position of the corotation radius inferred from the smoothed fields based on the function $|b_3| - |b_1|$ is stable for both galaxies (Fig. 16, cf. Figs. 6a and 11a).

6. CONCLUSION

(1) Introducing a velocity-field mask (i.e., the presence of holes in the disk filling with velocity measurements), even with pronounced higher harmonics in the spectrum, does not significantly affect the results of Fourier analysis of the resulting field. Fields with extremely low (below 20–25%) filling factors, in which the effect of random noise increases when calculating harmonics, constitute an exception.

(2) A practical corollary of the previous conclusion is that line-of-sight velocity measurements from optical emission lines can be used to analyze harmonic velocity components and to reconstruct a vector velocity field even if there are regions that are not filled with measurements.

(3) Although degrading the spatial resolution of the velocity field by up to a factor of 10 causes the amplitudes of the first three Fourier harmonics to decrease, it weakly affects the radial behavior of their phases and, in particular, the coordinate of zero of the function that determines the position of the corotation radius of a density wave.

(4) A practical corollary of the previous conclusion is that the results of Fourier analyses for optical and radio data, which differ greatly in angular resolution, can be compared. This conclusion has already been used previously when analyzing optical and radio line-of-sight velocity measurements of the gas in the galaxy NGC 3631 (Fridman *et al.* 1998). At the same time, the suppression of harmonic amplitudes with degrading spatial resolution makes low-resolution fields unsuitable for reconstructing the vector velocity field in galaxies.

ACKNOWLEDGMENTS

We are grateful to A. A. Boyarchuk for his useful discussions, which helped in more clearly formulating the problem and in identifying several useful analogies. This work was supported in part by the Russian Foundation for Basic Research (project no. 99-02-18 482), the Program “Leading Scientific Schools” (project no. 00-15-96 528), and the Federal Program "Astronomy" (project nos. 1.2.3.1 and 1.7.4.3).

REFERENCES

1. A. M. Fridman, O. V. Khoruzhiĭ, V. V. Lyakhovich, *et al.*, Astrophys. Space Sci. **252**, 115 (1997).
2. A. M. Fridman, O. V. Khoruzhiĭ, A. V. Zasov, *et al.*, Pis'ma Astron. Zh. **24**, 883 (1998) [Astron. Lett. **24**, 764 (1998)].
3. A. M. Fridman, O. V. Khoruzhiĭ, V. V. Lyakhovich, *et al.*, Astron. Astrophys. (2000) (in press).
4. V. V. Lyakhovich, A. M. Fridman, O. V. Khoruzhiĭ, and A. I. Pavlov, Astron. Zh. **74**, 509 (1997) [Astron. Rep. **41**, 447 (1997)].
5. V. Yu. Terebizh, *Analysis of Astrophysical Time Series* (Nauka, Moscow, 1992).

Translated by A. Dambis

Astronomy Letters, Vol. 26, No. 12, 2000, p. 821. Translated from Pis’ma v Astronomicheskiĭ Zhurnal, Vol. 26, No. 12, 2000, p. 954.
Original Russian Text Copyright © 2000.

Kopylov Ivan Mikheevich (October 14, 1928–July 29, 2000)

On July 29, 2000, Professor I.M. Kopylov, an eminent Russian astrophysicist, a brilliant pedagogue, the founder and first director of the Special Astrophysical Observatory (Academy of Sciences of the USSR), died at the age of 72.

I.M. Kopylov’s career as a scientist began at the Crimean Astrophysical Observatory (Academy of Sciences of the USSR) after he graduated from the Astronomical Department of the Leningrad State University in 1950. At that time, G.A. Shain gathered a brilliant galaxy of scientists here: A.B. Severnyi, S.B. Pikel’ner, I.S. Shklovskii, E.R. Mustel’, K.K. Chuvaev, and others. In this creative environment, I.M. Kopylov formed as an energetic, demanding, stellar astronomer. He mainly did research on stellar atmospheres, stellar spectroscopy, and stellar evolution. Together with A.A. Boyarchuk, he discovered a nonuniform dependence of the rotational velocity of stars on their luminosity. He developed a spectroscopic criterion for stellar classification. Under his leadership and with his direct participation, techniques for investigating stars were improved and new equipment was created for the 2.6-m telescope.

His authority as a scientist and experience in research and organizational work were so significant that I.M. Kopylov was offered to take charge of the Special Astrophysical Observatory (Russian Academy of Sciences), under construction at that time in the Caucasus. He bore the whole burden of setting up and developing this largest Observatory in the USSR and the world. He paid great attention to forming a creative staff at the Observatory and to developing lines of research. The largest astronomical instruments—the 6-m Large Telescope Azimuthal (LTA) and the RATAN-600 radio telescope with a 600-m ring-shaped antenna—were designed and put into operation at the Observatory. It became the world astronomical center. Studies in the field of stellar spectroscopy, polarimetry, photometry, stellar physics, and Galactic and extragalactic astronomy were successfully developed and are being carried out at the Observatory to this day.

I.M. Kopylov received a government award for his services in creating and developing the Observatory—an Order of the Red Banner of Labor—and was honored with the title of a Council of Ministers Price laureate. In recent years, I.M. Kopylov had fruitfully worked with astronomers of the Pulkovo Astronomical Observatory on fundamentally new astronomical problems in the field of space astrometry (STRUVE project) and took part in creating the International Solar Stereoscopic Observatory (STEREOSCOPE-A project).

The research activities of I.M. Kopylov are directly associated with the development of problems in stellar astronomy, stellar atmospheres and their chemical composition, stellar physics and their evolution, two-dimensional stellar spectroscopy, and binary nonstable stars with relativistic and degenerate components. The results of his studies were presented in more than 160 publications. I.M. Kopylov made a substantial contribution in compiling onboard input and specialized catalogs of spectroscopic, photometric, and astronomical data for astrometry and applied problems.

True interest in science, thoroughness and conscientiousness in studies, encyclopedic knowledge, experience and intuition, goodwill, and willingness to help characterized this brilliant man, a man of word and business. I.M. Kopylov founded a scientific school and his numerous pupils work at many observatories in Russia and the Ukraine.

I.M. Kopylov was a member of the International Astronomical Union and a member of the Editorial Board of Pis’ma v Astronomicheskii Zhurnal (Astronomy Letters). He was the vice-chairman of the Committee on large telescopes of the Russian Federation and a member of many academic councils.

The death of I.M. Kopylov is a heavy loss for our astronomical science.

Friends and colleagues

1063-7737/00/2612-0821$20.00